INVESTIGATION ON WAVE PROPAGATION CHARACTERISTICS IN PLATES AND PIPES FOR IDENTIFICATION OF STRUCTURAL DEFECT LOCATIONS

A Dissertation

by

JE HEON HAN

Submitted to the Office of Graduate Studies of
Texas A&M University
in partial fulfillment of the requirements for the degree of

DOCTOR OF PHILOSOPHY

Chair of Committee,	Yong-Joe Kim
Committee Members,	Alan Palazzolo
	Kuang-An Chang
	Won-Jong Kim
Head of Department,	Andreas A. Polycarpou

August 2013

Major Subject: Mechanical Engineering

ABSTRACT

For successful identification of structural defects in plates and pipes, it is essential to understand structural wave propagation characteristics such as dispersion relations. Analytical approaches to identify the dispersion relations of homogeneous, simple plates and circular pipes have been investigated by many researchers. However, for plates or pipes with irregular cross-sectional configurations or multi-layered composite structures, it is almost impossible to obtain the analytical dispersion relations and associated mode shapes. In addition, full numerical modeling approaches such as finite element (FE) methods are not economically feasible for high (e.g., ultrasonic) frequency analyses where an extremely large number of discretized meshes are required, resulting in significantly expensive computation.

In order to address these limitations, Hybrid Analytical/Finite Element Methods (HAFEMs) are developed to model composite plates and pipes in a computationally-efficient manner. When a pipe system is used to transport a fluid, the dispersion curves obtained from a "hollow" pipe model can mislead non-destructive evaluation (NDE) results of the pipe system. In this study, the HAFEM procedure with solid elements is extended by developing fluid elements and solid-fluid boundary conditions, resulting in the dispersion curves of fluid-filled pipes. In addition, a HAFEM-based acoustic transfer function approach is suggested to consider a long pipe system assembled with multiple pipe sections with different cross-sections. For the validation of the proposed

methods, experimental and full FE modeling results are compared to the results obtained from the HAFEM models.

In order to detect structural defect locations in shell structures from defect-induced, subtle wave reflection signals and eliminate direct-excitation-induced and boundary-reflected, relatively-strong wave signals, a time-frequency MUSIC algorithm is applied to ultrasonic wave data measured by using an array of piezoelectric transducers. A normalized, structurally-damped, cylindrical 2-D steering vector is proposed to increase the spatial resolution of time-frequency MUSIC power results. A cross-shaped array is selected over a circular or linear array to further improve the spatial resolution and to avoid the mirrored virtual image effects of a linear array. Here, it is experimentally demonstrated that the proposed time-frequency MUSIC beamforming procedure can be used to identify structural defect locations on an aluminum plate by distinguishing the defect-induced waves from both the excitation-generated and boundary-reflected waves.

ACKNOWLEDGEMENTS

I would like to thank my committee chair, Prof. Yong-Joe Kim for serving as my advisor on my study. This work could not have been done without his great advice and suggestions. In addition, I also would like to thank my committee members, Prof. Alan Palazzolo, Prof. Kuang-An Chang, and Prof. Won-Jong Kim (in the alphabetic order) for their seasoned guidance on this research.

Thanks also go to my friends and colleagues for making my time at Texas A&M University a great experience. Finally, my special thanks go to my wife and son for their prayers, dedication, encouragement, and patience.

TABLE OF CONTENTS

Page

LIST OF FIGURES

Page

LIST OF TABLES

Page

1. INTRODUCTION[*]

A guided ultrasonic Lamb wave in a shell structure can propagate a long distance with a small spatial dissipation rate so that it can be used to scan a large area of the structure for its structural defects with a relatively small number of sensors. Thus, it can be applied for the non-destructive evaluations (NDEs) of a large number of structures such as composite panels, pipelines, and drill strings [1-3]. When there is a structural defect in a system, an excited wave is propagating and then reflected from this defect. By measuring the reflective wave, the structural defect location and shape can be identified. In order to use the guided waves for the NDE applications, it is important to properly excite a plate or pipe system to generate a specific guided wave of which wave propagation characteristics are predetermined.

1.1 Identification of Wave Propagation Characteristics Using HAFEM

The dispersion curves of a shell structure contain information on frequency-dependent wave propagation characteristics such as phase speed, wavelength, and wavenumber. Therefore, various numerical and analytical methods have been developed to obtain the dispersion curves [3-7]. However, for plates or pipes with complicated cross-sectional configurations, such as multi-layered composite structures with irregular

[*] Parts of this section are reprinted from "Identification of Acoustic Characteristics of Honeycomb Sandwich Composite Panels Using Hybrid Analytical/Finite Element Method" by Y.-J. Kim and J.H. Han, 2013, *Journal of Vibration and Acoustics Transactions of American Society of Mechanical Engineers*, **135**, 011006 (11 pages), Copyright [2013] with permission by Journal of Vibration and Acoustics Transactions of American Society of Mechanical Engineers.

cross-sections, it is almost impossible to obtain analytical dispersion relations and associated mode shapes. In order to investigate wave propagation characteristics of these complex structures, numerical methods such as finite element methods (FEMs) have been also developed. However, these approaches are not always applicable to relatively high frequency analyses that require a large number of FEM meshes, resulting in high computational costs.

In order to address the aforementioned limitations with analytical and numerical approaches, a Hybrid Analytical/Finite Element Method (HAFEM) is proposed that uses a finite element approximation in the thickness direction (or cross-sectional directions) while an analytical solution is used in the plane directions (or axial direction). Thus, it makes possible to use a small number of finite elements even for high frequency (e.g., ultrasonic) analyses in a computationally-efficient manner. Here, when the thickness direction is discretized based on the finite element approximation for the case of plates, it is referred to as the Hybrid Analytical/1-D Finite Element Method (1-D HAFEM). Similarly, the 2-D finite element approximation combined with the 1-D analytical solution for the case of pipes is referred to as the Hybrid Analytical/2-D Finite Element Method (2-D HAFEM).

Previous research using hybrid 1-D approaches has some limitations, for example, including only in-plane, 2-D nodal displacements [8-9] or using an assumption of no reflective waves in the plane directions [10]. In this research, a 1-D HAFEM formulation is described that uses no assumption for analytical solutions in the plane

directions, which results in a partial differential system equation that can be used to consider the boundary conditions at the edges of "finite-size" panels [11].

Regarding 2-D HAFEM formulations, a hybrid finite strip element formulation was presented by Cheung in 1976 [12]. Taweel et al. [13] investigated wave propagation characteristics of rectangular bars and a circular cylinder by applying a hybrid approach. Kim and Bolton [14-15] investigated the vibration responses of a tire by modeling it using an analytical wave solution in the circumferential direction and 2-D shell finite elements in the cross-sectional directions. Kim and Han [11,16-17] studied the acoustic characteristics of honeycomb sandwich panels by applying the 1-D HAFEM. Hayashi et al. [18] obtained the dispersion curves of a railroad by using a hybrid method referred to as the Semi Analytical Finite Element Method (SAFEM) formulated with linear interpolation functions. In this research, the dispersion curves of hollow cylindrical pipes are obtained by using the 2-D HAFEM that employs an analytical solution in the axial direction and a Finite Element (FE) approximation in the cross-sectional directions [19]. While the FE approximations in the previous hybrid approaches are based on the linear interpolation functions, the current FE approximation uses quadratic interpolation functions to improve computational efficiency and accuracy. Additionally, a forced solution procedure for pipe systems with simply-supported boundary conditions is presented, while the forced dynamic responses of the finite-size pipe cannot be analyzed by using the previous hybrid approaches. The proposed, forced solution approach is validated by comparing the HAFEM-predicted responses to the analytical solutions of a simply-supported, hollow, cylindrical pipe. The proposed 2-D HAFEM procedure is

also validated by comparing the HAFEM-predicted and analytical dispersion curves of the cylindrical pipe.

1.2 Wave Propagation Modeling of Fluid-filled Pipe System Assembled with Multiple, Different Cross-sections Using HAFEM

When a pipe system is used to transport a fluid, the dispersion curves obtained from a "hollow" pipe model can mislead NDE results of the pipe system. Therefore, dispersion curves including fluid loading effects are essential for obtaining accurate NDE results. The aforementioned hybrid approaches cannot be used to analyze the fluid loading effects to the best knowledge of the authors. In this study, the existing 2-D HAFEM procedure with the solid elements is extended by developing fluid elements and solid-fluid boundary conditions, resulting in dispersion curves of fluid-filled pipes. Similar to the hybrid solid elements in Ref. 19, the hybrid fluid element uses a 2-D finite element approximation in the cross-sectional area, while an analytical wave solution is assumed in the axial direction. The proposed method is validated by comparing the HAFEM-predict dispersion curves to "experimental" ones of an empty pipe and "analytical" ones of a fluid-filled pipe. The analytical results of the fluid-filled pipe in Ref. 7 are reused for this comparison.

Although the HAFEM is useful to understand wave propagation characteristics of fluid-filled, multi-layered composite pipes with arbitrary cross-sections, the cross-sectional shapes should not be changed in the axial direction. In order to consider a pipe system assembled with multiple pipe sections with different cross-sections, an acoustic

transfer function is derived from the HAFEM formation. Although an "analytical" acoustic transfer function was derived from shell vibration equations [20] to model drill string systems, this analytical approach cannot be used to consider fluid loading effects and multi-layered composite pipes. For the validation of the proposed, HAFEM-based, acoustic transfer function method, the frequency response functions (FRFs) obtained from the proposed method are compared to experimental results for both hollow and fluid-filled pipes.

1.3 Time-frequency Beamforming for NDEs Using Ultrasonic Wave

In order to detect structural defect locations in a plate based on the wave propagation characteristic identified by using the HAFEM, the plate is excited with a specific ultrasonic Lamb wave and wave signals are recorded by using an array of Piezoelectric Wafer Active Sensors (PWASs) [21,22]. When there is a structural defect in the system, the excited wave is then reflected from the defect. By measuring the reflective wave and processing the measured wave signal, the structural defect location can be identified. The latter procedure can be implemented to scan a large structural area with a relatively small number of transducers due to the long propagation distance of the guided wave.

The guided Lamb wave generation characteristics of piezoelectric actuators were studied by Crawley et al. [23-24] and Giurgiutiu [21]. Giurgiutiu et al. [21-22] suggested a mode tuning technique to dominantly excite a single mode Lamb wave by selecting an appropriate excitation frequency for the given dimensions and material properties of a piezoelectric actuator and a shell structure.

NDE algorithms for processing measured guided wave signals are listed in Refs. [2,25]. A pulse-echo method using a PWAS array referred to as the embedded ultrasonic structural radar was used for detecting cracks on a panel [26]. Wang et al. improved the conventional pulse-echo and pitch-catch method by applying a time reversal process to suppress boundary effects and thus increase the signal to noise ratio (SNR) although this method required undamaged baseline data [27-28]. In Ref. [29], Ikegami et al. introduced an aircraft health monitoring system by using embedded-piezoelectric transducers and continuously comparing measured data with undamaged data. Sohn et al. suggested a damage diagnostic procedure that does not require undamaged data by combining a consecutive outlier analysis and a time reversal procedure [30]. Giurgiutiu et al. [31] and Yan et al. [32] found structural defect locations in aluminum and composite plates from two-dimensional (2-D) beamforming power images constructed by using a Delay-And-Sum (DAS) beamforming algorithm. In addition, Li et al. applied a Multiple Signal Classification (MUSIC) beamforming algorithm to identify air-filled cylindrical target locations in a water-filled tank at a high spatial resolution [33]. Belanger et al. investigated the performance of a MUSIC algorithm by considering numerically-simulated, second-order scattering between defects with a high spatial resolution of 0.1λ where λ is the wavelength [34].

The aforementioned MUSIC beamforming algorithms can be applied to identify structural defects in “ideal” and “simple” shell structures such as infinite-size and uniform-thickness shells. However, in a “real” shell structure, high-level waves are reflected from many discontinuous features such as boundaries and stiffeners. In

general, the waves reflected from the structural defects have much weaker signal strength than direct excitation waves and reflective waves from the structural boundaries or stiffeners. Then, it is almost impossible to identify the structural defects using the aforementioned, steady-state beamforming algorithms due to the strong direct excitation and reflective wave signals. In order to overcome this problem, a time-gating approach removing reflection time data from boundaries is generally applied [35]. For an embedded structure health monitoring system installed in the middle of a structure, the latter method can be useful since the measured time signals of boundary-reflected waves are appeared at the end of the time data and can be thus easily distinguished from the defect-induced waves that are measured before the arrival of the boundary-reflected waves. However, this approach is difficult to be applied when defect-induced reflective waves appears later than or at the same time with boundary-reflected waves.

In this article, experimental results obtained with a 1.22 m × 0.92 m × 0.002 m aluminum plate placed on small foam blocks around its edges are presented. For the purpose of simulating structural defects in this experiment, coins or washers are glued on the aluminum plate, which is similar to the cases in Refs. [27-28] where mass blocks are glued on an aluminum plate. A cross-shaped array of 7 mm × 7 mm piezoelectric transducers is also installed on the plate. One of the transducers is excited with a Lamb burst signal and the transducer array is then used to measure direct and reflective wave signals. In order to avoid multi-mode wave generation and spatial aliasing, the excitation frequency is set to 20 kHz. Then, a single anti-symmetric A0 Lamb wave

mode whose wavelength is long enough to avoid the spatial aliasing is excited selectively at this excitation frequency.

By applying conventional, steady-state MUSIC beamforming algorithms to the measured array signals, it is shown that these algorithms are unable to identify the locations of the simulated structural defects in the aluminum plate due to the multiple wave reflections. Thus, it is proposed to improve the beamforming algorithms by exploiting the temporal information of the reflective wave signals from the defects and boundaries as well as the spatial information that the defect locations are not coincident with the boundaries. In order to realize this idea, a "time-frequency" MUSIC algorithm is proposed in this article.

Belouchrani et al. and Johnson et al. introduced the concept of a time-frequency beamforming procedure [36-37]. However, its applications are limited to estimate the "direction of arrival (DOA)" of active sources. In this article, the proposed time-frequency MUSIC algorithm is applied to identify the "locations" (i.e., directions and distances) of "structural defects" by measuring reflected waves from the defects on a plate, which does not require any specific time filtering or gating to distinguish defect- and boundary-induced reflective wave events. The proposed algorithm is expected to be useful, in particular, when boundary-reflected waves are measured earlier than or at the same time with defect-reflected waves. In the latter case, it is difficult to filter out the boundary-reflected signals unless the locations of the boundaries and defects are visualized on temporal beamforming power maps obtained by using the proposed time-frequency algorithm. For example, when the defect- and boundary-induced reflective

waves are measured at the same time, the proposed algorithms can separate these waves based on their reflection locations identified on the resulting MUSIC beamforming power map.

Additionally, a normalized, structurally-damped, 2-D cylindrical steering vector is proposed to increase the spatial resolution of time-frequency MUSIC power results, accurately pinpointing structural defect locations. A cross-shaped array is here selected over a circular or linear array to further improve the spatial resolution and to avoid the mirrored virtual image effects of the linear array.

Through the experimental results obtained by applying the proposed time-frequency MUSIC beamforming algorithm to the measured array data, it is shown that the proposed algorithms can be used to successfully locate the simulated defects.

2. INVESTIGATION ON WAVE PROPAGATION CHARACTERISTICS USING HYBRID ANALYTICAL/NUMERICAL APPROACHES*

In order to investigate wave propagation characteristics in structures such as panels and pipes for their NDEs, the HAFEM procedures are developed. For the validation of these methods, analytical solutions or experimental results are compared to HAFEM results. In order to obtain dispersion curves of fluid-filled pipes, the HAFEM procedure with solid elements is extended by developing fluid elements and solid-fluid boundary conditions. In addition, for the purpose of considering a pipe system assembled with multiple pipe sections with different cross-sections, an acoustic transfer function is derived from the HAFEM formation.

2.1 Hybrid Analytical/One-Dimensional Finite Element Method

For the Hybrid Analytical/One-Dimensional Finite Element Method (1-D HAFEM) formulation for analyzing structural wave propagation characteristics in composite panels, it is assumed that each composite layer is homogeneous: i.e., each layer is assumed to be represented well by a single set of material properties. It is also assumed that each layer has a constant thickness. For example, Fig. 1 illustrates the HAFEM model of a double-layered composite panel. In this model, two elements are used to

* Parts of this section are reprinted with permission from "Identification of Acoustic Characteristics of Honeycomb Sandwich Composite Panels Using Hybrid Analytical/Finite Element Method" by Y.-J. Kim and J.H. Han, 2013, *Journal of Vibration and Acoustics Transactions of American Society of Mechanical Engineers*, **135**, 011006 (11 pages), Copyright [2013] by Journal of Vibration and Acoustics Transactions of American Society of Mechanical Engineers.

represent layer 1 and one element for layer 2. Since the displacements are approximated by the combination of nodal displacements and "linear" interpolation functions in the *z*-direction, there are two nodes per one element. In the following section, the HAFEM formulation is first derived for a single hybrid element. The global equation of motion (EOM) for a multi-element system can then be obtained by assembling the local EOMs of all elements.

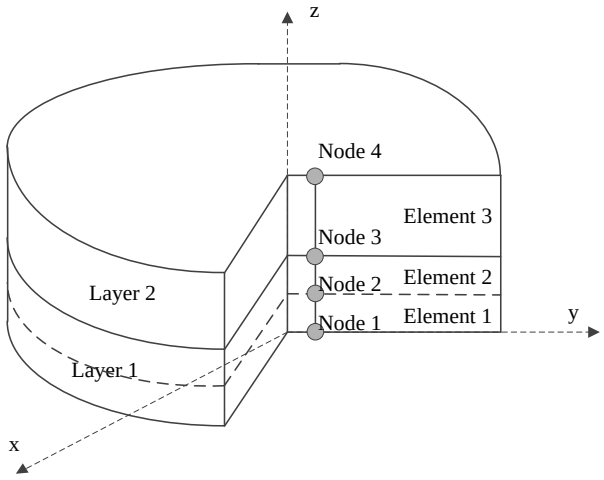

Figure 1: Illustration of HAFEM model of double-layered panel.

2.1.1 One-Dimensional HAFEM Equation

The displacements of a single hybrid element can be approximated in terms of its nodal displacements, that are the functions of *x*, *y*, and *t*, combined with the linear interpolation functions, N_1 and N_2 in the *z*-direction: i.e.,

$$\begin{bmatrix} u(x,y,z,t) \\ v(x,y,z,t) \\ w(x,y,z,t) \end{bmatrix} = \begin{bmatrix} N_1(z) & 0 & 0 & N_2(z) & 0 & 0 \\ 0 & N_1(z) & 0 & 0 & N_2(z) & 0 \\ 0 & 0 & N_1(z) & 0 & 0 & N_2(z) \end{bmatrix} \begin{bmatrix} u_1 & v_1 & w_1 & u_2 & v_2 & w_2 \end{bmatrix}^{\mathrm{T}}, \quad (2.1)$$

where the superscript, T represents the transpose of a vector or matrix and N_1 and N_2 are the interpolation functions defined as

$$N_1(z) = 1 - \frac{z}{d} \text{ and } N_2(z) = \frac{z}{d}. \quad (2.2)$$

When the deformation of the element is small enough, the strains can be linearly related to the displacements: i.e.,

$$\mathbf{e}(x,y,z,t) = \begin{bmatrix} \frac{\partial u}{\partial x} & \frac{\partial v}{\partial y} & \frac{\partial w}{\partial z} & \frac{\partial v}{\partial x} + \frac{\partial u}{\partial y} & \frac{\partial w}{\partial y} + \frac{\partial v}{\partial z} & \frac{\partial w}{\partial x} + \frac{\partial u}{\partial z} \end{bmatrix}^{\mathrm{T}}, \quad (2.3)$$

where **e** represents the strain vector. By using the stress-strain relation (i.e., constitutive relation) represented by a matrix, **C**, the stress vector can be related to the strain vector as

$$\mathbf{s} = \mathbf{C}\mathbf{e}, \quad (2.4)$$

where the matrix **C**, for example, for an orthotropic material can be expressed as

$$\mathbf{C} = \begin{bmatrix} C_{11} & C_{12} & C_{13} & 0 & 0 & 0 \\ C_{12} & C_{22} & C_{23} & 0 & 0 & 0 \\ C_{13} & C_{23} & C_{33} & 0 & 0 & 0 \\ 0 & 0 & 0 & C_{44} & 0 & 0 \\ 0 & 0 & 0 & 0 & C_{55} & 0 \\ 0 & 0 & 0 & 0 & 0 & C_{66} \end{bmatrix}. \quad (2.5)$$

The virtual work principle is expressed as

$$\delta(U - T - W) = 0, \tag{2.6}$$

where the potential energy U, the kinetic energy T, and the work W are represented, respectively, as

$$U = \frac{1}{2}\int_t\int_x\int_y\int_z \left(\mathbf{e}^{\mathrm{H}}\mathbf{C}\mathbf{e}\right) dx\,dy\,dz\,dt\,, \tag{2.7}$$

$$T = \frac{1}{2}\int_t\int_x\int_y\int_z \rho\dot{\mathbf{u}}^{\mathrm{T}}\dot{\mathbf{u}}\,dx\,dy\,dz\,dt, \tag{2.8}$$

and

$$W = \frac{1}{2}\int_t\int_x\int_y \mathbf{u}^{\mathrm{T}}\mathbf{f}\,dx\,dy\,dt\,. \tag{2.9}$$

Then, the EOM of the single element can be derived by substituting Eqs. (2.7) – (2.9) into Eq. (2.6): i.e.,

$$\mathbf{K}_{xx}\frac{\partial^2\mathbf{u}}{\partial x^2} + \mathbf{K}_{xy}\frac{\partial^2\mathbf{u}}{\partial x\partial y} + \mathbf{K}_{yy}\frac{\partial^2\mathbf{u}}{\partial y^2} + \mathbf{K}_{xz}\frac{\partial\mathbf{u}}{\partial x} + \mathbf{K}_{yz}\frac{\partial\mathbf{u}}{\partial y} + \mathbf{K}_{zz}\mathbf{u} + \mathbf{M}\frac{\partial^2\mathbf{u}}{\partial t^2} = \mathbf{f}^{\mathrm{i}} + \mathbf{f}^{\mathrm{e}}, \tag{2.10}$$

where $\mathbf{u}$ is the nodal displacement vector (i.e., $\mathbf{u} = [u_1\ v_1\ w_1\ u_2\ v_2\ w_2]^{\mathrm{T}}$), $\mathbf{K}$ is the element stiffness matrix, and $\mathbf{M}$ represents the element mass matrix. In Eq. (2.10), $\mathbf{f}^{\mathrm{i}}$ and $\mathbf{f}^{\mathrm{e}}$ are the internal and external force vectors, respectively. A set of orthotropic material properties can be considered in Eq. (2.10) when the stiffness matrices are calculated by using the constitutive equation of an orthotropic material in Eq. (2.4). For a multi-element system, all local element matrices can be assembled into a global matrix. For a compact notation, the same symbols are used for both local and global quantities from

now on. Furthermore, the left-hand-side terms associated with the stiffness matrices in Eq. (2.10) can be represented as the linear operator defined by

$$\mathbf{L} = \mathbf{K}_{xx}\frac{\partial^2}{\partial x^2} + \mathbf{K}_{xy}\frac{\partial^2}{\partial x \partial y} + \mathbf{K}_{yy}\frac{\partial^2}{\partial y^2} + \mathbf{K}_{xz}\frac{\partial}{\partial x} + \mathbf{K}_{yz}\frac{\partial}{\partial y} + \mathbf{K}_{zz}. \tag{2.11}$$

When the system is excited at a single angular frequency of ω, the global EOM can be then expressed as

$$\mathbf{L}\{\mathbf{u}(\mathbf{x})\} - \omega^2 \mathbf{M}\mathbf{u}(\mathbf{x}) = \mathbf{f}(\mathbf{x}), \tag{2.12}$$

where **u** is the nodal displacement vector and **x** represents the position vector in the *x*-*y* plane: i.e., **x** = (*x*, *y*). The internal force vector in Eq. (2.10) is not shown in Eq. (2.12) since a pair of internal forces facing each other at a node is cancelled during the global matrix assembly process.

2.1.2 Dispersion Relations of Lamb Wave

For the analysis of the Lamb wave propagation in a composite panel, a plane strain case with no external external forces (i.e., **f** = **0** in Eq. (2.12)) is considered by neglecting the *y*-direction nodal displacements: i.e., $v_n = 0$ where $n = 1, 2, \ldots, N$. The spatial derivative with respect to *y* can also be neglected in Eq. (2.11). Then, the displacement vector can be assumed as

$$\mathbf{u}(x, y, t) = \mathbf{U}\exp(ikx - i\omega t), \tag{2.13}$$

where the complex amplitude vector is defined as

$$\mathbf{U} = \begin{bmatrix} U_1 & W_1 & U_2 & W_2 & \cdots & U_N & W_N \end{bmatrix}^{\mathrm{T}}. \tag{2.14}$$

The resulting eigenvalue problem can be then written as

$$\left(-\mathbf{K}_{xx}k^2 + i\mathbf{K}_{xz}k + \mathbf{K}_{zz} - \omega^2\mathbf{M}\right)\mathbf{U} = \mathbf{0}. \tag{2.15}$$

For a nontrivial displacement vector, the determinant of the coefficient matrix should be equal to zero: i.e.,

$$\det\left(-\mathbf{K}_{xx}k^2 + i\mathbf{K}_{xz}k + \mathbf{K}_{zz} - \omega^2\mathbf{M}\right) = 0. \tag{2.16}$$

From Eq. (2.16), the dispersion relations (i.e., k-ω relations) of the Lamb waves propagating in a composite panel can be calculated. Then, the phase speed of the Lamb wave can be obtained from [38]

$$c_p = \frac{\omega}{k}. \tag{2.17}$$

In order to validate the proposed 1-D HAFEM, the wave speeds in an aluminum plate with the thickness of 2 mm is calculated as a function of frequency by using both the analytical method (see Eqs. (C.24) and (C.25) in Appendix C.1) and the 1-D HAFEM with equally-spaced 51 nodes in the thickness direction. Table 1 shows the material properties of the aluminum panel. As shown in Fig. 2, the dispersion curves predicted by using the HAFEM are well matched with the analytical dispersion relations.

Aluminum Panel	Thickness ($2h$)	0.002 m
	Young's Modulus (E)	7.1×10^{10} Pa
	Poisson's Ratio (ν)	0.2396
	Density (ρ)	2700 kg/m^3

Table 1: Material properties of aluminum panel.

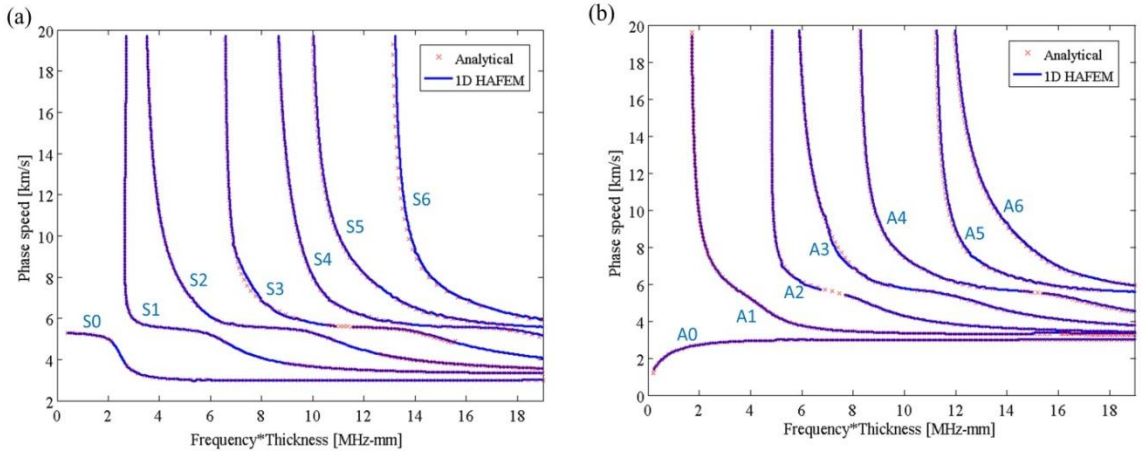

Figure 2: Dispersion relations of waves propagating in 2 mm aluminum plate: (a) Symmetric modes and (b) Anti-symmetric modes.

Figure 3 shows the wave shapes in the thickness direction for several Lamb modes (see the mode numbers, S0, S1, …, S6 and A0, A1, …, A6 associated with the dispersion curves in Fig. 2). The analytical mode shapes in the thickness direction obtained from Eqs. (C.20) and (C.21) are well in line with the HAFEM results. Although the validation of the proposed HAFEM procedure is limited to the simple aluminum panel in this Section, the other validation cases with composite honeycomb sandwich panels can be found in the following Section. Therefore, it can be concluded that the dispersion curves of multi-layered panels can be also obtained by using the proposed HAFEM procedure.

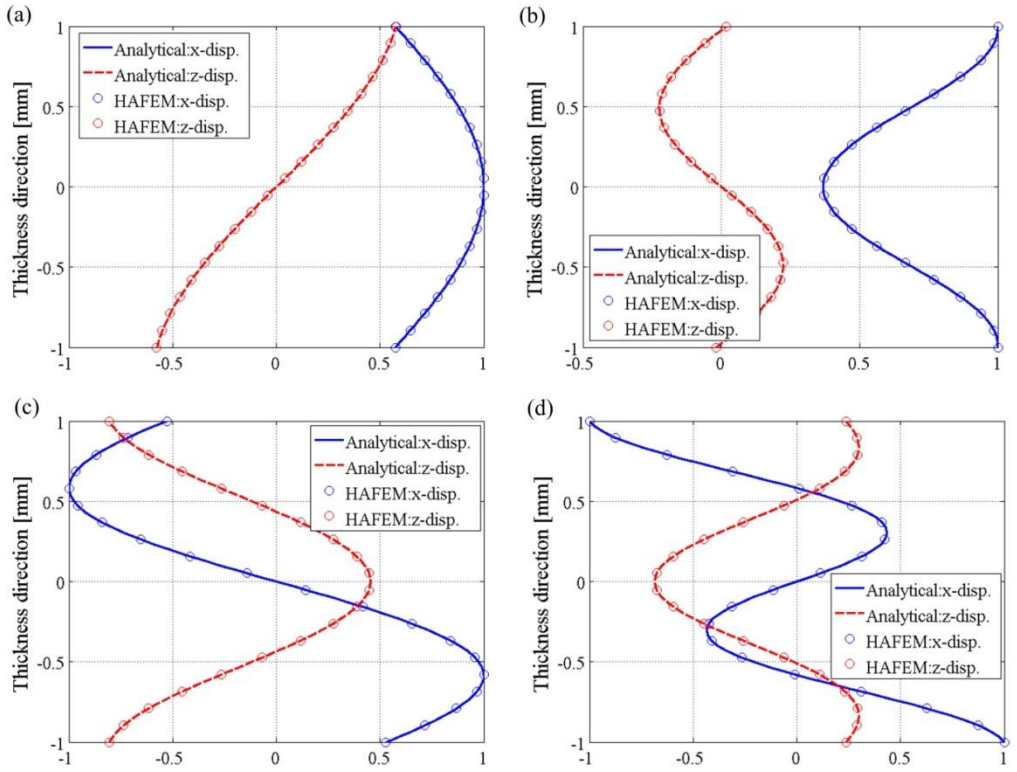

Figure 3: Cross-sectional wave shapes of 2 mm aluminum plate: **(a)** S0 mode at $f{\cdot}2h$ = 1.91 MHz·mm, **(b)** S1 mode at $f{\cdot}2h$ = 4.09 MHz·mm, **(c)** A1 mode at $f{\cdot}2h$ = 3.91 MHz·mm, and **(d)** A2 mode at $f{\cdot}2h$ = 5.07 MHz·mm.

2.1.3 Wave Propagation Characteristics in Honeycomb Sandwich Panel

In this Section, structural wave propagation characteristics of a honeycomb sandwich panel are investigated. When a plane wave is incident on the bottom surface of the panel at a single frequency, the external force vector in Eq. (2.12) is represented as the combination of incident, reflected, and transmitted sound pressure waves: i.e.,

$$\mathbf{L}\{\mathbf{v}(\mathbf{x})\} - \omega^2 \mathbf{M}\mathbf{v}(\mathbf{x}) = -j\omega\{\mathbf{s}_1(p_i(\mathbf{x}) + p_r(\mathbf{x})) - \mathbf{s}_N p_t(\mathbf{x})\}, \tag{2.18}$$

where $\mathbf{v}$ is the nodal velocity vector ($\mathbf{v} = \partial\mathbf{u}/\partial t$), p_i, p_r, and p_t are the incident, reflected, and transmitted sound pressures, respectively, and $\mathbf{s}_1$ and $\mathbf{s}_N$ represent the unit vectors normal to the bottom and top surfaces of the panel, respectively. In order to identify the "structural" wave propagation characteristics of the panel, it is assumed that there is no fluid loading on the panel surfaces: e.g., the panel is placed in vacuum where there is no sound radiation. When the panel is excited with a distributed, harmonic force with specific wave numbers, (k_x, k_y) and a frequency, f on the bottom surface of the panel, its normal vibration response can be found from Eq. (2.18) with the only p_i term on the right hand side: i.e.,

$$\mathbf{L}\{\mathbf{v}(\mathbf{x})\} - \omega^2 \mathbf{M}\,\mathbf{v}(\mathbf{x}) = -j\,\omega \mathbf{s}_1\, p_i(\mathbf{x})\,. \tag{2.19}$$

After solving Eq. (2.19), the vibration response on the top surface is represented as

$$v(x,y,t) = \mathbf{s}_N^{\mathrm{T}}\mathbf{v}(x,y,t) = \mathrm{Re}[V(k_x,k_y,f)\exp(ik_x x + ik_y y - i2\pi ft)]\,, \tag{2.20}$$

where V is the complex velocity amplitude. The amplitude of vibration response at a specific radial wave number, $k_r = [k_x^2 + k_y^2]^{0.5}$ can be then defined as an integral of $|V(k_x, k_y, f)|$ along the circle, $C(k_r)$ with the radius of k_r in the (k_x, k_y) domain: i.e.,

$$\bar{v}(k_r, f) = \oint_{C(k_r)} \left|V(k_x,k_y,f)\right| dk_r\,. \tag{2.21}$$

The resulting vibration response, $\bar{v}$ can be plotted as a (k_r, f) contour plot, where peak responses represent the dispersion relations of the structural waves propagating in the panel. In addition, the analytical dispersion curves of the sound wave, flexural wave,

core shear waves, and skin flexural wave can be overlaid on the top of the (k_r, f) contour plot. The dispersion curve of the flexural wave is represented as

$$k = \sqrt[4]{(2\pi f)^2 m / D}, \tag{2.22}$$

where m is the mass per unit area and D is the equivalent flexural stiffness calculated based on the assumption of a "thin" composite plate [39]. The core shear wave speed can be calculated by using the following equation: i.e.,

$$c_{C.S.} = \sqrt{\frac{G}{m}}, \tag{2.23}$$

where G is the core shear modulus. For an orthotropic core that has two different core shear moduli (e.g., G_{zx} and G_{yz} in Table 2), the core shear wave can have two different wave speeds depending on its wave propagation direction. The dispersion curve of the skin flexural wave is calculated as

$$k = \sqrt[4]{(2\pi f)^2 m / (2D_S)}, \tag{2.24}$$

where the mass per unit area is the half of the total mass per unit area, m of the panel [40]. In Eq. (2.24), the skin flexural stiffness, D_S is defined as

$$D_S = \frac{E_S t_S^3}{12(1-\mu_S^2)}, \tag{2.25}$$

where E_S, t_S, and μ_S are the Young's modulus, thickness, and Poisson's ratio of the skin, respectively [40].

Face Sheet (Isotropic Material)	Thickness (d)	5.842×10^{-4} m
	Density (ρ)	1716 kg/m^3
	Young's Modulus (E)	6.128×10^{10} Pa
	Poisson's Ratio (ν)	0.143
	Loss Factor (η)	0.05
Nomex Core (Orthotropic Material)	Thickness (d)	0.9017×10^{-2} m
	Density (ρ)	128.1 kg/m^3
	Young's Modulus (E_{xx})	6.895×10^{5} Pa
	Young's Modulus (E_{yy})	6.895×10^{5} Pa
	Young's Modulus (E_{zz})	5.792×10^{8} Pa
	Shear Modulus (G_{yz})	7.033×10^{7} Pa
	Shear Modulus (G_{zx})	1.570×10^{8} Pa
	Shear Modulus (G_{xy})	6.985×10^{5} Pa
	Poisson's Ratio (ν_{yz})	0.01
	Poisson's Ratio (ν_{zx})	0.01
	Poisson's Ratio (ν_{xy})	0.50
	Loss Factor (η)	0.05

Table 2: Material properties of honeycomb sandwich panels.

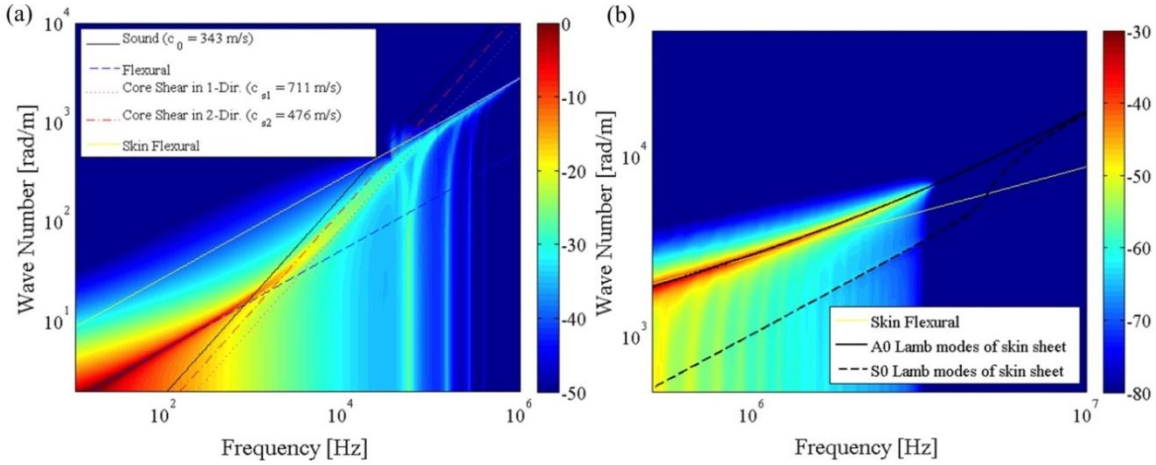

Figure 4: Dispersion relations of honeycomb sandwich panel: **(a)** Frequency range up to 1MHz and **(b)** Frequency range from 500 kHz to 10 MHz.

The material properties of the honeycomb sandwich panel are listed in Table 2. The resulting vibration response, $\bar{v}$ in Eq. (2.21) is plotted in Fig. 4 where the peak responses represent the dispersion relations of the structural waves propagating in the honeycomb sandwich panel. The vibration levels are presented in the dB scale referenced at the maximum vibration level. In Fig. 4, the dark red represents the highest vibration response while the dark blue indicates the lowest vibration response. In addition, the analytical dispersion curves of the sound wave (i.e., the black line in Fig. 4(a)), the flexural wave (i.e., the blue dashed line), the core shear waves (i.e., the magenta dotted and red dash dot lines), and the skin flexural wave (i.e., the yellow solid line) are overlaid on the top of the contour plot in Fig. 4(a). In Fig. 4(a), the flexural wave speed is slower than the sound wave speed at low frequencies (e.g., below 900 Hz) while it is faster than the sound wave speed at mid to high frequencies (e.g., above 900 Hz): note that the two wave speeds are coincident approximately at 900 Hz. The sound wave and core shear waves have the constant wave speeds: i.e., they are non-dispersive. The sound wave speed is 343m/s and the core shear wave speeds are 476m/s and 711m/s (see Eq. (2.23)). The core shear wave in the x-direction is faster than the core shear wave in the y-direction since G_{zx} is larger than G_{yz} (see Table 2). In Fig. 4(a), the peak response asymptotically converges to the analytical flexural wave at the low audible frequencies below 900 Hz. At high frequencies (e.g., 5 kHz to 50 kHz), there are two vibration peaks at a single frequency, each peak converging to one of the core shear waves. At low ultrasonic frequencies (e.g., from 100 kHz to 1 MHz), the vibration peak converges to the skin flexural wave. At high ultrasonic frequencies above 1 MHz in Fig. 4(b), the

vibration peak asymptotically converges to the skin Lamb A0 wave as the frequency increases. Therefore, at ultrasonic frequencies, it can be found that the face sheet is dominantly in control of the wave responses. The higher modes cut on at the frequencies of 70 kHz, 108 kHz, and so on.

2.2 Hybrid Analytical/Two-Dimensional Finite Element Method

2.2.1 Two-Dimensional HAFEM Equation

As shown in Fig. 5, a quadratic finite element with 9 nodes in the *x*-*y* coordinates can be mapped into the ξ-η coordinates in the domain of ξ = -1 to 1 and η = -1 to 1.

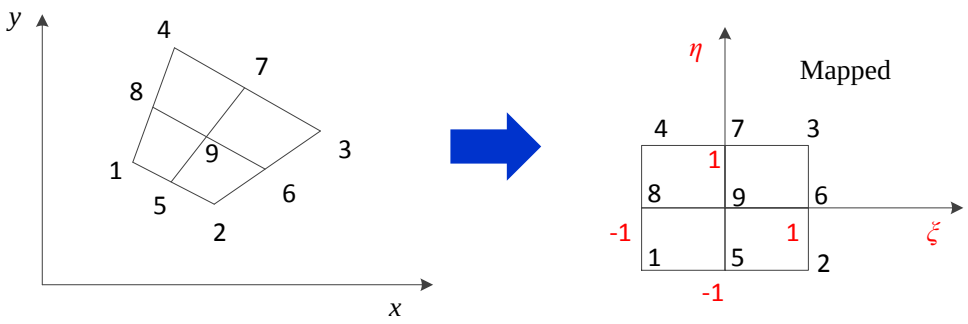

Figure 5: Coordinate transformation.

This mapping is defined as [41]

$$x(\xi,\eta) = \mathbf{N}^{\mathrm{T}}(\xi,\eta)\mathbf{x}\,, \tag{2.26a}$$

$$y(\xi,\eta) = \mathbf{N}^{\mathrm{T}}(\xi,\eta)\mathbf{y}\,, \tag{2.26b}$$

where

$$\mathbf{x} = [x_1 \; x_2 \; x_3 \; x_4 \; x_5 \; x_6 \; x_7 \; x_8 \; x_9]^{\mathrm{T}}, \tag{2.26c}$$

$$\mathbf{y} = [y_1 \; y_2 \; y_3 \; y_4 \; y_5 \; y_6 \; y_7 \; y_8 \; y_9]^{\mathrm{T}}, \tag{2.26d}$$

$$\mathbf{N}(\xi,\eta) = [N_1 \; N_2 \; N_3 \; N_4 \; N_5 \; N_6 \; N_7 \; N_8 \; N_9]^{\mathrm{T}}, \tag{2.26e}$$

$$N_1 = \frac{1}{4}\xi(\xi-1)\eta(\eta-1), \; N_2 = \frac{1}{4}\xi(\xi+1)\eta(\eta-1), \; N_3 = \frac{1}{4}\xi(\xi+1)\eta(\eta+1), \tag{2.27a - c}$$

$$N_4 = \frac{1}{4}\xi(\xi-1)\eta(\eta+1), \; N_5 = (1-\xi)(\xi+1)\frac{1}{2}\eta(\eta-1), \; N_6 = \frac{1}{2}\xi(\xi+1)(1-\eta)(\eta+1), \tag{2.27d - f}$$

$$N_7 = (1-\xi)(\xi+1)\frac{1}{2}\eta(\eta+1), \; N_8 = \frac{1}{2}\xi(\xi-1)(1-\eta)(\eta+1), \; N_9 = (1-\xi)(\xi+1)(1-\eta)(\eta+1). \tag{2.27g - i}$$

This coordinate transformation simplifies a spatial integral in the *x*-*y* domain dramatically by mapping this integral to the ξ-η domain. In order to implement this coordinate transformation, a chain rule is defined as

$$\begin{bmatrix} \dfrac{\partial f}{\partial \xi} \\ \dfrac{\partial f}{\partial \eta} \end{bmatrix} = \begin{bmatrix} \dfrac{\partial x}{\partial \xi} & \dfrac{\partial y}{\partial \xi} \\ \dfrac{\partial x}{\partial \eta} & \dfrac{\partial y}{\partial \eta} \end{bmatrix} \begin{bmatrix} \dfrac{\partial f}{\partial x} \\ \dfrac{\partial f}{\partial y} \end{bmatrix} = \mathbf{J} \begin{bmatrix} \dfrac{\partial f}{\partial x} \\ \dfrac{\partial f}{\partial y} \end{bmatrix}, \tag{2.28}$$

where **J** is the Jacobian matrix. By substituting Eqs. (2.26a) and (2.26b) into Eq. (2.28), the Jacobian matrix and its determinant can be represented, respectively, as

$$\mathbf{J} = \begin{bmatrix} \dfrac{\partial x}{\partial \xi} & \dfrac{\partial y}{\partial \xi} \\ \dfrac{\partial x}{\partial \eta} & \dfrac{\partial y}{\partial \eta} \end{bmatrix} = \begin{bmatrix} \dfrac{\partial \mathbf{N}^T(\xi,\eta)}{\partial \xi}\mathbf{x} & \dfrac{\partial \mathbf{N}^T(\xi,\eta)}{\partial \xi}\mathbf{y} \\ \dfrac{\partial \mathbf{N}^T(\xi,\eta)}{\partial \eta}\mathbf{x} & \dfrac{\partial \mathbf{N}^T(\xi,\eta)}{\partial \eta}\mathbf{y} \end{bmatrix} = \begin{bmatrix} J_{11} & J_{12} \\ J_{21} & J_{22} \end{bmatrix}, \tag{2.29}$$

and

$$\left|\mathbf{J}\right| = \det(\mathbf{J}) = \frac{\partial \mathbf{N}^T(\xi,\eta)}{\partial \xi}\mathbf{x}\frac{\partial \mathbf{N}^T(\xi,\eta)}{\partial \eta}\mathbf{y} - \frac{\partial \mathbf{N}^T(\xi,\eta)}{\partial \xi}\mathbf{y}\frac{\partial \mathbf{N}^T(\xi,\eta)}{\partial \eta}\mathbf{x}. \qquad (2.30)$$

For an element, vibration displacements in the ξ-η coordinates are approximated by applying the quadratic interpolation functions to the nodal displacements. In the *z*-direction, an analytical solution is assumed: i.e., the nodal displacements are the functions of the time and *z*-location. The displacement vector is then represented as

$$\boldsymbol{\psi}(\xi,\eta,z,t) = \begin{bmatrix} u(\xi,\eta,z,t) \\ v(\xi,\eta,z,t) \\ w(\xi,\eta,z,t) \end{bmatrix} = \mathbf{N}_u(\xi,\eta)\mathbf{u}(z,t) = \begin{bmatrix} N_1 & 0 & 0 & & N_9 & 0 & 0 \\ 0 & N_1 & 0 & \cdots & 0 & N_9 & 0 \\ 0 & 0 & N_1 & & 0 & 0 & N_9 \end{bmatrix} \begin{bmatrix} u_1 \\ v_1 \\ w_1 \\ \vdots \\ u_9 \\ v_9 \\ w_9 \end{bmatrix}. \qquad (2.31)$$

Then, a strain vector can be expressed by the partial derivatives of the displacements: i.e.,

$$\mathbf{e}(x,y,z,t) = \begin{bmatrix} \frac{\partial u}{\partial x} & \frac{\partial v}{\partial y} & \frac{\partial w}{\partial z} & \frac{\partial v}{\partial x}+\frac{\partial u}{\partial y} & \frac{\partial w}{\partial y}+\frac{\partial v}{\partial z} & \frac{\partial w}{\partial x}+\frac{\partial u}{\partial z} \end{bmatrix}^{\mathrm{T}}. \qquad (2.32)$$

The stress vector can be related to the strain vector by using a constitutive matrix **C**: i.e.,

$$\mathbf{s} = \mathbf{C}\mathbf{e}. \qquad (2.33)$$

For the case of orthotropic materials, the matrix C can be expressed as

$$\mathbf{C} = \begin{bmatrix} C_{11} & C_{12} & C_{13} & 0 & 0 & 0 \\ C_{12} & C_{22} & C_{23} & 0 & 0 & 0 \\ C_{13} & C_{23} & C_{33} & 0 & 0 & 0 \\ 0 & 0 & 0 & C_{44} & 0 & 0 \\ 0 & 0 & 0 & 0 & C_{55} & 0 \\ 0 & 0 & 0 & 0 & 0 & C_{66} \end{bmatrix}. \qquad (2.34)$$

In order to derive the 2-D HAFEM EOM for a single element, the virtual work principle is applied: i.e.,

$$\delta(U - T - W) = 0, \tag{2.35}$$

where the potential energy, the kinetic energy, and the work are represented, respectively, as

$$U = \frac{1}{2}\int_t\int_x\int_y\int_z \left(\mathbf{e}^{\mathrm{H}}\mathbf{C}\mathbf{e}\right) dx\,dy\,dz\,dt, \tag{2.36}$$

$$T = \frac{1}{2}\int_t\int_x\int_y\int_z \rho \frac{\partial \mathbf{u}^{\mathrm{H}}}{\partial t}\mathbf{N}_u^{\mathrm{H}}\mathbf{N}_u \frac{\partial \mathbf{u}}{\partial t} dx\,dy\,dz\,dt, \tag{2.37}$$

$$W = \frac{1}{2}\int_t\int_z \mathbf{u}^{\mathrm{H}}\mathbf{f}\, dz\,dt. \tag{2.38}$$

Finally, the equation of motion for the element can be obtained by substituting Eqs. (2.29), (2.31), (2.32), and (2.36) – (2.38) into Eq. (2.35): i.e.,

$$\bar{\mathbf{K}}_{zz}\frac{\partial^2 \mathbf{u}}{\partial z^2} + \bar{\mathbf{K}}_{(\xi+\eta)z}\frac{\partial \mathbf{u}}{\partial z} + \bar{\mathbf{K}}_{\xi+\eta}\mathbf{u} + \bar{\mathbf{M}}\frac{\partial^2 \mathbf{u}}{\partial t^2} = \mathbf{f}^{\mathrm{i}} + \mathbf{f}^{\mathrm{e}}, \tag{2.39}$$

where

$$\bar{\mathbf{K}}_{zz} = -\int_{\xi=-1}^{1}\int_{\eta=-1}^{1} \mathbf{B}_z^{\mathrm{H}}\mathbf{C}\mathbf{B}_z \left|\mathbf{J}\right| d\xi d\eta, \tag{2.40}$$

$$\bar{\mathbf{K}}_{(\xi+\eta)z} = \int_{\xi=-1}^{1}\int_{\eta=-1}^{1} (\mathbf{B}_{\xi+\eta}^{\mathrm{H}}\mathbf{C}\mathbf{B}_z - \mathbf{B}_z^{\mathrm{H}}\mathbf{C}\mathbf{B}_{\xi+\eta})\left|\mathbf{J}\right| d\xi d\eta, \tag{2.41}$$

$$\bar{\mathbf{K}}_{\xi+\eta} = \int_{\xi=-1}^{1}\int_{\eta=-1}^{1} \mathbf{B}_{\xi+\eta}^{\mathrm{H}}\mathbf{C}\mathbf{B}_{\xi+\eta} \left|\mathbf{J}\right| d\xi d\eta dz dt, \tag{2.42}$$

$$\bar{\mathbf{M}} = \int_{\xi=-1}^{1}\int_{\eta=-1}^{1} \rho \mathbf{N}_u^{\mathrm{H}} \mathbf{N}_u \left|\mathbf{J}\right| d\xi d\eta, \tag{2.43}$$

$$\mathbf{B}_{\xi+\eta} = \begin{bmatrix} B_{(\xi+\eta),1} & B_{(\xi+\eta),2} & B_{(\xi+\eta),3} & B_{(\xi+\eta),4} & B_{(\xi+\eta),5} & B_{(\xi+\eta),6} & B_{(\xi+\eta),7} & B_{(\xi+\eta),8} & B_{(\xi+\eta),9} \end{bmatrix}, \tag{2.44a}$$

$$\mathbf{B}_z = \begin{bmatrix} B_{z,1} & B_{z,2} & B_{z,3} & B_{z,4} & B_{z,5} & B_{z,6} & B_{z,7} & B_{z,8} & B_{z,9} \end{bmatrix}, \tag{2.44b}$$

$$\mathbf{B}_{(\xi+\eta),i} = \begin{bmatrix} \frac{\partial N_i}{\partial \xi}(\mathbf{J}^{-1})_{11} + \frac{\partial N_i}{\partial \eta}(\mathbf{J}^{-1})_{12} & 0 & 0 \\ 0 & \frac{\partial N_i}{\partial \eta}(\mathbf{J}^{-1})_{22} + \frac{\partial N_i}{\partial \xi}(\mathbf{J}^{-1})_{21} & 0 \\ 0 & 0 & 0 \\ \frac{\partial N_i}{\partial \xi}(\mathbf{J}^{-1})_{21} + \frac{\partial N_i}{\partial \eta}(\mathbf{J}^{-1})_{22} & \frac{\partial N_i}{\partial \xi}(\mathbf{J}^{-1})_{11} + \frac{\partial N_i}{\partial \eta}(\mathbf{J}^{-1})_{12} & 0 \\ 0 & 0 & \frac{\partial N_i}{\partial \xi}(\mathbf{J}^{-1})_{21} + \frac{\partial N_i}{\partial \eta}(\mathbf{J}^{-1})_{22} \\ 0 & 0 & \frac{\partial N_i}{\partial \xi}(\mathbf{J}^{-1})_{11} + \frac{\partial N_i}{\partial \eta}(\mathbf{J}^{-1})_{12} \end{bmatrix}, \tag{2.44c}$$

$$\mathbf{B}_{z,i} = \begin{bmatrix} 0 & 0 & N_i & 0 & 0 & 0 \\ 0 & 0 & 0 & 0 & N_i & 0 \\ 0 & 0 & 0 & 0 & 0 & N_i \end{bmatrix}^{\mathrm{T}}. \tag{2.44d}$$

In Eq. (2.39), the superscripts, "e" and "i" on the force vector **f** represent the "external" and "internal" forces, respectively. The double integrals in Eqs. (2.40) – (2.43) can be calculated by using the Gauss-Legendre quadrature [41]. For a FE system with multiple elements, the global HAFEM EOM is obtained by assembling all of the individual stiffness and mass matrices and force vectors. During this global assembly process, the internal forces are cancelled out. For convenience, the same notation for both the local and global nodal displacement vectors is used although the upper bar in the local

stiffness and mass matrices in Eqs. (2.39) – (2.43) are dropped for the global matrices: i.e.,

$$\mathbf{K}_{zz}\frac{\partial^2\mathbf{u}}{\partial z^2}+\mathbf{K}_{(\xi+\eta)z}\frac{\partial\mathbf{u}}{\partial z}+\mathbf{K}_{\xi+\eta}\mathbf{u}+\mathbf{M}\frac{\partial^2\mathbf{u}}{\partial t^2}=\mathbf{f}\,. \tag{2.45}$$

2.2.2 Forced Response of Two-Dimensional HAFEM System

When a system is excited at a single angular frequency of ω, the global HAFEM EOM can be rewritten from Eq. (2.45) as

$$\mathbf{L}(1-i\eta)\mathbf{u}-\omega^2\mathbf{M}\mathbf{u}=\mathbf{f}(\mathbf{x})\,, \tag{2.46}$$

where η is the structural loss factor and $\mathbf{L}$ is the linear operator defined as

$$\mathbf{L}=\mathbf{K}_{zz}\frac{\partial^2}{\partial z^2}+\mathbf{K}_{(\xi+\eta)z}\frac{\partial}{\partial z}+\mathbf{K}_{\xi+\eta}\,. \tag{2.47}$$

For finite-size structures, the modal displacement vector can be written as

$$\mathbf{u}_m(z,t)=\mathbf{U}_m\exp(-i\omega_m t)\,, \tag{2.48}$$

$$\mathbf{U}_m(z,t)=\beta_m\boldsymbol{\Psi}_m(z)\boldsymbol{\varphi}_m\,, \tag{2.49}$$

where $\boldsymbol{\varphi}_m$ is the modal amplitude vector. In Eq. (2.49), the diagonal element of the diagonal matrix, $\boldsymbol{\Psi}_m$ for a circular pipe with the simply-supported boundary condition is written as [39]

$$\psi_m(z)=\begin{cases}\sin(m\pi z/L), & \text{for } x\text{-direction nodal displacement}\\ \sin(m\pi z/L), & \text{for } y\text{-direction nodal displacement}\\ \cos(m\pi z/L), & \text{for } z\text{-direction nodal displacement}\end{cases}, \tag{2.50}$$

where L is the length of the pipe in the z-direction. In Eq. (2.48), β_m is the mode normalization factor with respect to the mass matrix **M**: i.e.,

$$\int_0^L \beta_m^2 \boldsymbol{\varphi}_m^{\mathrm{H}} \boldsymbol{\Psi}_m^{\mathrm{H}}(z) \mathbf{M} \boldsymbol{\Psi}_m(z) \boldsymbol{\varphi}_m dz = 1. \tag{2.51}$$

Equation (2.48) satisfies Eq. (2.46) for an undamped, free-vibration case (i.e., **f** = **0** and η = 0). In this case, by substituting Eq. (2.48) into Eq. (2.46), an eigenvalue problem for calculating the modal amplitude vector can be represented as

$$\mathbf{L} \boldsymbol{\Psi}_m(z) \boldsymbol{\varphi}_m - \omega_m^2 \mathbf{M} \boldsymbol{\Psi}_m(z) \boldsymbol{\varphi}_m = 0. \tag{2.52}$$

The cosine and sine components of Eq. (2.52) are cancelled out since each row has only one cosine or sine function. Therefore, Eq. (2.52) can be rewritten as

$$\mathbf{S}_m \boldsymbol{\varphi}_m - \omega_m^2 \mathbf{M} \boldsymbol{\varphi}_m = 0. \tag{2.53}$$

For a harmonic excitation at an angular frequency of ω, the forced solution is then expressed as the superposition of the modes: i.e.,

$$\mathbf{u}(z,t) = \sum_m C_m \beta_m \boldsymbol{\Psi}_m(z) \boldsymbol{\varphi}_m \exp(-i\omega t), \tag{2.54}$$

where C_m is the modal contribution coefficient for the m-th mode. By substituting Eq. (2.54) into Eq. (2.46) and applying the orthogonality of $\mathbf{U}_n^{\mathrm{H}}(z)$, the modal contribution coefficient can be obtained as

$$C_m = \frac{f_m}{(1 - \mathrm{i}\eta)\omega_m^2 - \omega^2}, \tag{2.55}$$

where f_m is the modal force represented as

$$f_m = \int_0^L \beta_m \boldsymbol{\varphi}_m^{\mathrm{H}} \boldsymbol{\Psi}_m^{\mathrm{H}}(z) \mathbf{f} dz \,. \tag{2.56}$$

2.2.3 Dispersion Relation of Circular Pipe

When it is assumed that there is no reflection wave (e.g., infinite length in the *z*-direction), a wave solution can be set as

$$\mathbf{u} = \mathbf{u_0} \exp^{i(kz-\omega t)} \,. \tag{2.57}$$

By substituting Eq. (2.57) into Eq. (2.45) for the free vibration case [18], an eigenvalue problem is derived as

$$\left(\begin{bmatrix} 0 & \mathbf{K}_{\xi+\eta} - \omega^2 \mathbf{M} \\ \mathbf{K}_{\xi+\eta} - \omega^2 \mathbf{M} & i\mathbf{K}_{(\xi+\eta)z} \end{bmatrix} - k \begin{bmatrix} \mathbf{K}_{\xi+\eta} - \omega^2 \mathbf{M} & 0 \\ 0 & \mathbf{K}_{zz} \end{bmatrix} \right) \begin{bmatrix} \mathbf{U} \\ k\mathbf{U} \end{bmatrix} = 0 \,. \tag{2.58}$$

The dispersion relation between the wavenumber k and the angular frequency ω can be obtained by solving the eigenvalue problem in Eq. (2.58). Although a large number of FE nodes in the *z*-direction are required for a full 3-D FE model, the proposed HAFEM procedure for calculating the dispersion relation makes it possible to use a small number of finite elements in a computationally efficient manner by considering an analytical wave solution in the *z*-direction as in Eq. (2.57).

2.2.4 Validation Cases: Natural Frequencies and Forced Responses of Simply-Supported Pipes

In this section, the forced, flexural vibration responses of simply-supported, hollow, circular pipes obtained from 2-D HAFEM models at low frequencies are compared to the analytical vibration responses calculated by using the Euler-Bernoulli beam theory

[38]. Figure 8 shows an example of a 2-D HAFEM model for analyzing the pipe system. As shown in Fig. 6, the cross-section of the pipe is modeled by using the finite elements while an analytical solution is assumed in the *z*-direction.

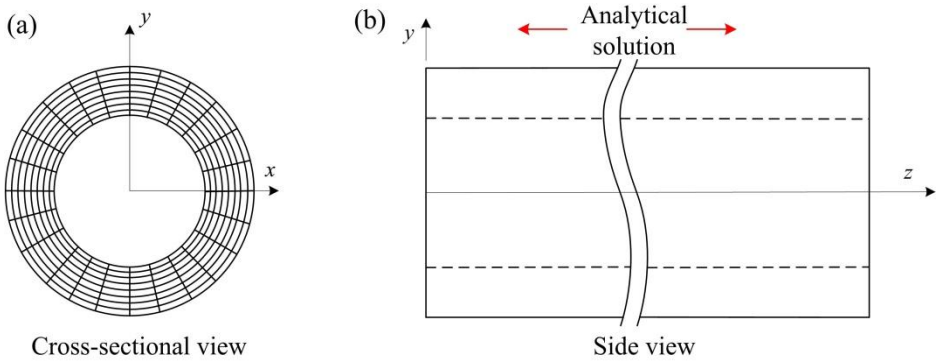

Figure 6: Illustration of 2-D HAFEM model for analyzing hollow, cylindrical pipes: **(a)** FE approximation on cross-section and **(b)** Analytical solution in axial direction.

An 1 mm thick aluminum pipe simply-supported at the both ends is used for validating the proposed 2-D HAFEM procedure. The material properties and geometry information of this pipe are shown as Case I in Table 3. Regarding the cross-sectional FE mesh, it consists of 9 nodes in the *r*-direction and 24 nodes in the θ-direction. Therefore, the cross-section is discretized by using 48 elements with 216 nodes (216 = 9 × 24). For a harmonic, point excitation in the *y*-direction with the excitation frequencies of 100 Hz and 200 Hz at z = 0.3 m, the resulting natural frequencies and displacements obtained by using both of the 2-D HAFEM and analytical methods are shown in Table 4 and Fig. 7, respectively. From Table 4 and Fig. 7, it is shown that the natural frequencies and the vibration forced responses obtained by both of the approaches are

almost identical except the very low natural frequencies (i.e., from 0.106 Hz to 0.405 Hz). These low natural frequencies are associated with rigid body motions. Since the HAFEM model contains the natural frequencies of the *x*- and *y*-direction rigid body motions and the cross-section of the pipe is symmetry with respect to the *x*- and *y*-axes, the duplicated natural frequencies are calculated from the HAFEM model as shown in Table 4.

	Case I	Case II
Material	Aluminum	
Young's modulus [Pa]	7.1×E10	
Density [kg/m^3]	2700	
Poisson's Ratio	0.33	
Structural damping coefficient	0.01	
Outer diameter [mm]	6	40
Thickness [mm]	1	3
Length [m]	1	N/A

Table 3: Material properties and geometry information of hollow, circular pipe.

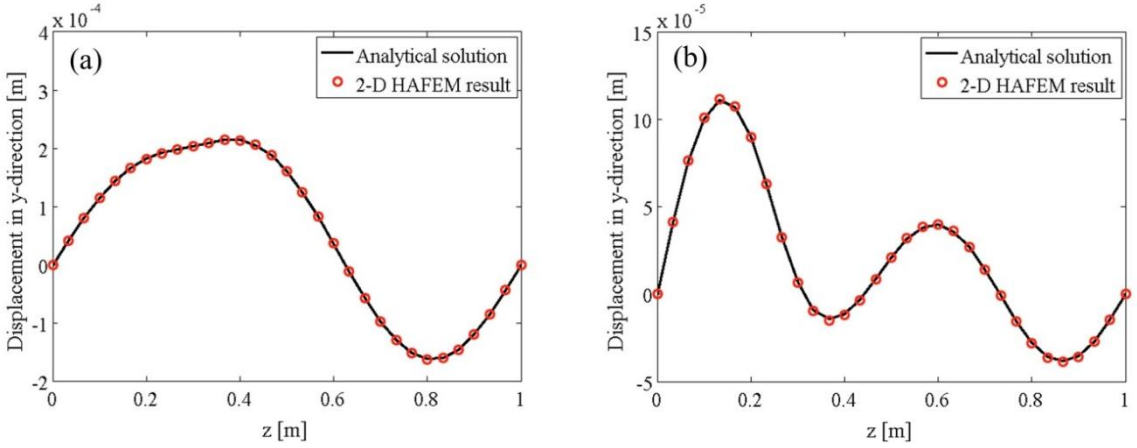

Figure 7: Displacement amplitudes in *y*-direction for Case I in Table 3 when excited by *y*-directional, harmonic, point force excitation at z = 0.3m: **(a)** 100 Hz and **(b)** 200 Hz.

Method	Natural frequencies [Hz]							
Analytical					14.52		58.07	
	130.7		232.3	···				
HAFEM	0.106	0.197	0.299	0.405	14.52	14.52	58.07	58.07
	130.6	130.6	232.0	232.0	···			

Table 4: Natural frequencies of simply-supported pipe (Case I in Table 3).

2.2.5 Dispersion Relations in Ultrasonic Frequency Range

Figure 8(a) shows the dispersion relations of axisymmetric longitudinal and torsional modes up to 1.5 MHz for Case II in Table 3. In order to obtain the axisymmetric modes, it is assumed that ultrasonic wave responses have no spatial variation in the circumferential direction. In order to realize this condition in the HAFEM model, all of the displacements in the θ-direction set to be equal and the dimension of the stiffness and mass matrices in Eq. (2.58) is then reduced from 648 × 648 (648 = 9×24×3) to 27 × 27 (27 = 9×3): the HAFEM model has 24 nodes in the circumferential direction. The dispersion curves are then calculated from Eq. (2.58) with the reduced stiffness and mass matrices. As shown in Fig. 8(a), the dispersion relations obtained by using the HAFEM agree well with the analytical dispersion relations obtained from Eq. (C.51).

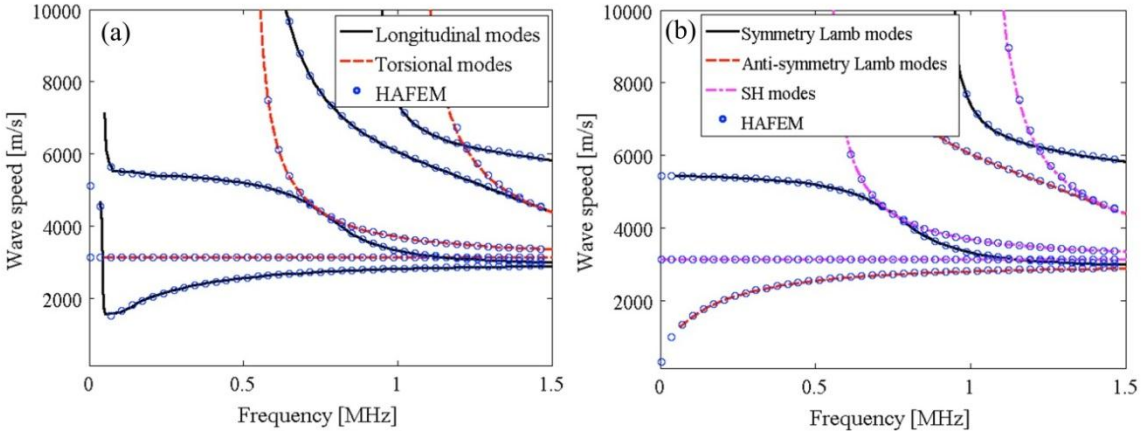

Figure 8: Dispersion relations up to 1.5 MHz for Case II in Table 3: **(a)** Outer diameter of 40 mm and **(b)** Outer diameter of 1 km.

As shown in Fig. 8(b), the HAFEM wave modes in the second validation case of the extremely large radius case (e.g., $r = 1\ km$) become the Lamb wave or SH modes of the equivalent flat aluminum plate (i.e., $r = \infty$) with the same thickness of 3 mm. The analytical dispersion relations for the Lamb wave modes are obtained from Eqs. (C.25) and (C.26). For the SH modes, the analytical dispersion equation is represented as Eq. (C.33).

2.3 Hybrid Analytical/Two-Dimensional Finite Element Method for Modeling Fluid-Filled Pipe

When a pipe system is used to transport a fluid, the dispersion curves obtained from a "hollow" pipe model can mislead NDE results of the pipe system. Therefore, dispersion curves including fluid loading effects is essential for obtaining accurate NDE results. In this section, the existing 2-D HAFEM procedure with the solid elements is

extended by developing fluid elements and solid-fluid boundary conditions. Since the detailed information on the solid element is presented in Section 2.2, the only fluid elements will be discussed in this section. In this research, it is not considered for the case of existing bubbles in a fluid or a mean flow in a pipe.

2.3.1 Governing Equation

The constitutive equation for a Newtonian fluid is [42]

$$\sigma_{ij} = -p\delta_{ij} + \mu\left(\frac{\partial \dot{u}_j}{\partial x_i} + \frac{\partial \dot{u}_i}{\partial x_j}\right) + \lambda\delta_{ij}\dot{\mathbf{e}}_{kk} \,. \tag{2.59}$$

By approximating the volume change as $\Delta V/V \cong e_{xx} + e_{yy} + e_{zz}$ and expressing the pressure in Eq. (2.59) as $p = -\kappa\Delta V/V$, Eq. (2.59) can be rewritten as

$$\mathbf{s} = \mathbf{C}_1\mathbf{e} + \mathbf{C}_2\dot{\mathbf{e}} \,. \tag{2.60}$$

In a full matrix form, Eq. (2.60) can be represented as

$$\begin{bmatrix} \sigma_{xx} \\ \sigma_{yy} \\ \sigma_{zz} \\ \tau_{xy} \\ \tau_{yz} \\ \tau_{zx} \end{bmatrix} = \begin{bmatrix} \kappa & \kappa & \kappa & 0 & 0 & 0 \\ \kappa & \kappa & \kappa & 0 & 0 & 0 \\ \kappa & \kappa & \kappa & 0 & 0 & 0 \\ 0 & 0 & 0 & 0 & 0 & 0 \\ 0 & 0 & 0 & 0 & 0 & 0 \\ 0 & 0 & 0 & 0 & 0 & 0 \end{bmatrix} \begin{bmatrix} e_{xx} \\ e_{yy} \\ e_{zz} \\ \gamma_{xy} \\ \gamma_{yz} \\ \gamma_{zx} \end{bmatrix} + \begin{bmatrix} 2\mu+\lambda & \lambda & \lambda & 0 & 0 & 0 \\ \lambda & 2\mu+\lambda & \lambda & 0 & 0 & 0 \\ \lambda & \lambda & 2\mu+\lambda & 0 & 0 & 0 \\ 0 & 0 & 0 & \mu & 0 & 0 \\ 0 & 0 & 0 & 0 & \mu & 0 \\ 0 & 0 & 0 & 0 & 0 & \mu \end{bmatrix} \begin{bmatrix} \dot{e}_{xx} \\ \dot{e}_{yy} \\ \dot{e}_{zz} \\ \dot{\gamma}_{xy} \\ \dot{\gamma}_{yz} \\ \dot{\gamma}_{zx} \end{bmatrix}, \tag{2.61}$$

where κ is the bulk modulus, μ is the dynamic viscosity coefficient, and λ is the bulk viscosity coefficient. For a non-Newtonian fluid case, a linearization around an equilibrium point is required to build a constitutive matrix such as Eq. (2.61). By

applying the variational principle in Eq. (2.35), 2-D HAFEM equation of motion for the single element can be obtained in Eq. (2.62).

$$\bar{\mathbf{K}}_{zz}\frac{\partial^2\mathbf{u}}{\partial z^2}+\bar{\mathbf{K}}_{(x+y)z}\frac{\partial\mathbf{u}}{\partial z}+\bar{\mathbf{K}}_{x+y}\mathbf{u}+\bar{\mathbf{M}}\frac{\partial^2\mathbf{u}}{\partial t^2}=\mathbf{f}^{\mathrm{i}}+\mathbf{f}^{\mathrm{e}}, \tag{2.62}$$

where $\bar{\mathbf{K}}$ is the element stiffness matrix, $\bar{\mathbf{M}}$ is the element mass matrix, $\mathbf{u}$ is the nodal displacement vector of the element, and $\mathbf{f}^{\mathrm{i}}$ and $\mathbf{f}^{\mathrm{e}}$ represent the internal and external forces. For a harmonic excitation, the stiffness matrices and mass matrix of this fluid element can be expressed as

$$\bar{\mathbf{K}}_{zz}(\omega)=-\int_{\xi=-1}^{1}\int_{\eta=-1}^{1}(\mathbf{B}_z^{\mathrm{H}}\mathbf{C}_1\mathbf{B}_z-i\omega\mathbf{B}_z^{\mathrm{H}}\mathbf{C}_2\mathbf{B}_z)\left|\mathbf{J}\right|d\xi d\eta, \tag{2.63}$$

$$\bar{\mathbf{K}}_{(x+y)z}(\omega)=\int_{\xi=-1}^{1}\int_{\eta=-1}^{1}(\mathbf{B}_{\xi+\eta}^{\mathrm{H}}\mathbf{C}_1\mathbf{B}_z-\mathbf{B}_z^{\mathrm{H}}\mathbf{C}_1\mathbf{B}_{\xi+\eta}+i\omega\mathbf{B}_{\xi+\eta}^{\mathrm{H}}\mathbf{C}_2\mathbf{B}_z-i\omega\mathbf{B}_z^{\mathrm{H}}\mathbf{C}_2\mathbf{B}_{\xi+\eta})\left|\mathbf{J}\right|d\xi d\eta, \tag{2.64}$$

$$\bar{\mathbf{K}}_{\xi+\eta}(\omega)=\int_{\xi=-1}^{1}\int_{\eta=-1}^{1}(\mathbf{B}_{\xi+\eta}^{\mathrm{H}}\mathbf{C}_1\mathbf{B}_{\xi+\eta}+i\omega\mathbf{B}_{\xi+\eta}^{\mathrm{H}}\mathbf{C}_2\mathbf{B}_{\xi+\eta})\left|\mathbf{J}\right|d\xi d\eta dz dt, \tag{2.65}$$

$$\bar{\mathbf{M}}=\int_{\xi=-1}^{1}\int_{\eta=-1}^{1}\rho\mathbf{N}^{\mathrm{H}}\mathbf{N}\left|\mathbf{J}\right|d\xi d\eta. \tag{2.66}$$

For a multi-element FE system, the global HAFEM equation is obtained by assembling the local element stiffness matrices, mass matrix, and force vectors in the global coordinate. The internal forces are cancelled out during this global assembly process. For convenience, the same notations used in the local matrices is reused for the global matrices after dropping the upper bars in Eq. (2.62): i.e.,

$$\mathbf{K}_{zz}\frac{\partial^2\mathbf{u}}{\partial z^2}+\mathbf{K}_{(x+y)z}\frac{\partial\mathbf{u}}{\partial z}+\mathbf{K}_{x+y}\mathbf{u}+\mathbf{M}\frac{\partial^2\mathbf{u}}{\partial t^2}=\mathbf{f}. \tag{2.67}$$

Structural waves in real structures decay out due to the structural damping. In order to consider this damping effect when $\exp(ikx\text{-}i\omega t)$ is assumed as the positive-propagating wave exponential function, the complex Young's modulus [43] is defined as

$$\bar{E} = E(1-\eta i), \tag{2.68}$$

where E is the Young's modulus and η is the structural damping coefficient. The structural damping coefficient can be obtained by using the following relation [44,45]: i.e.,

$$\eta = 2\xi, \tag{2.69}$$

where ξ is the viscous damping ratio which can be measured by using the half power method [46].

2.3.2 Dispersion Relation in Low Audible Frequencies

From Eq. (2.58), the wavenumbers associated with longitudinal, torsional, and flexural waves at each frequency can be obtained (i.e., at a single frequency, two longitudinal wavenumbers k_{L+} and k_{L-}, two torsional wavenumbers k_{T+} and k_{T-}, and four flexural wavenumbers, k_{FR+}, k_{FR-}, k_{FI+} and k_{FI-} can be obtained by solving Eq. (2.58)). When there are N nodes in a 2-D HAFEM model, $3\times N$ wavenumbers satisfying Eq. (2.58) are obtained. Except the wavenumbers associated with the longitudinal, torsional, flexural waves, other wavenumbers can be ignored due to their large imaginary parts. As shown in Fig. 9, the dispersion relations for the longitudinal and torsional waves can be obtained for the given material properties of a hollow pipe in Table 5. For the HAFEM

model, 5 nodes in the r-direction and 16 nodes in the θ-direction are used. The HAFEM model is validated by comparing the analytical dispersion relations obtained by using $\omega = k(E/\rho)^{1/2}$ for longitudinal waves and $\omega = k(G/\rho)^{1/2}$ for torsional waves where G and ρ are the shear modulus and density, respectively. The dispersion curves obtained from the HAFEM are well aligned to the analytical dispersion curves. In Fig. 9, the positive wavenumbers represent positive-going waves and the negative wavenumbers, negative-going waves.

Young's Modulus [GPa]	201
Density [kg/m^3]	7400
Thickness [mm]	3.55
Outer diameter [mm]	42.2
Poisson's ratio	0.285

Table 5: Material properties of hollow pipe.

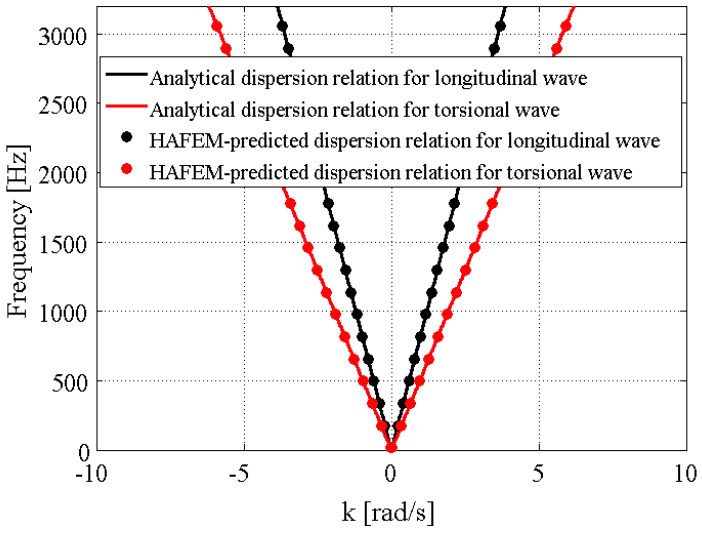

Figure 9: Dispersion relations of longitudinal and torsional waves for hollow pipe in Table 5.

In Fig. 10, the dispersion relations for the flexural waves are plotted. Bulk waves such as longitudinal and torsional waves in low frequencies are dependent on material properties. (i.e., $c_p = (E/\rho)^{0.5}$ and $c_p = (G/\rho)^{0.5}$) However, flexural waves even in low frequencies and guided waves in ultrasonic frequencies depend on geometry information as well as material properties. Both the real and imaginary wavenumbers are plotted in Fig. 10. The imaginary wavenumbers are associated with exponentially-decaying evanescent waves. Note that the two real and two imaginary wavenumbers are required to describe the flexural wave motions properly at a single frequency. As the frequency increases, the discrepancy between the analytical and HAFEM results become larger since the analytical solution obtained from the Bernoulli–Euler beam theory (i.e., $k = (\omega^2 \rho A/E/I)^{1/4}$) is supposed to be valid only for slander beams under the condition that the flexural waves are not coupled with other waves in low frequencies where the wavelength are much larger than the cross-sectional dimensions. Therefore, the dispersion curves obtained from both the analytical and HAFEM analyses becomes identical at low frequencies.

Water (at 15 ℃)	Density [kg/m^3]	998.2
	Bulk viscosity [Pa·s]	3.1×10^{-3}
	Dynamic viscosity [Pa·s]	1.155×10^{-3}
	Bulk modulus [GPa]	2.2

Table 6: Material properties of water filled inside of pipe in Table 5.

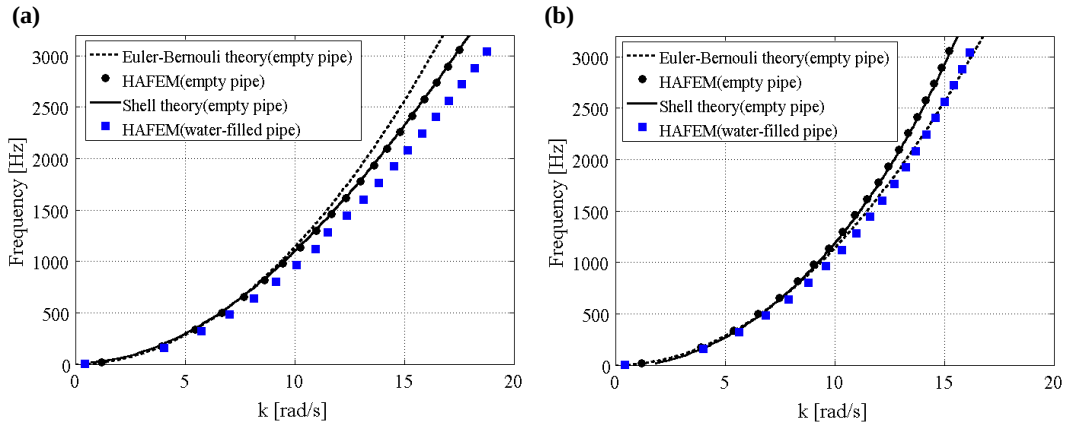

Figure 10: Dispersion relations of flexural wave for water-filled pipe in Tables 5 and 6: **(a)** Real parts of wavenumbers and **(b)** Imaginary parts of wavenumbers.

In order to validate the HAFEM dispersion results, the dispersion curves based on the thick shell theory are introduced and compared with the HAFEM dispersion results in Fig. 10. The five governing equations [39] to describe the motion of the empty pipe modeled by using the thick shell theory including the effects of shear deformation and rotary inertia are expressed as

$$\frac{k'Gh}{a}\frac{\partial \varepsilon_{r\theta}}{\partial \theta}+k'Gh\frac{\partial \varepsilon_{rz}}{\partial z}-\frac{N_{\theta\theta}}{a}-\rho h\frac{\partial^2 u_r}{\partial t^2}=0, \tag{2.70}$$

$$\frac{1}{a}\frac{\partial N_{\theta\theta}}{\partial \theta}+\frac{\partial N_{\theta z}}{\partial z}+\frac{k'Gh\varepsilon_{r\theta}}{a}-\rho h\frac{\partial^2 u_\theta}{\partial t^2}=0\ , \tag{2.71}$$

$$\frac{1}{a}\frac{\partial N_{\theta z}}{\partial \theta}+\frac{\partial N_{zz}}{\partial z}-\rho h\frac{\partial^2 u_z}{\partial t^2}=0, \tag{2.72}$$

$$\frac{\partial M_{z\theta}}{\partial z}+\frac{1}{a}\frac{\partial M_{\theta\theta}}{\partial \theta}-k'Gh\varepsilon_{r\theta}-\frac{\rho h^3}{12}\frac{\partial^2 \beta_\theta}{\partial t^2}=0\ , \tag{2.73}$$

$$\frac{\partial M_{zz}}{\partial z}+\frac{1}{a}\frac{\partial M_{\theta z}}{\partial \theta}-k'Gh\varepsilon_{rz}-\frac{\rho h^3}{12}\frac{\partial^2 \beta_z}{\partial t^2}=0\ , \tag{2.74}$$

where u is the displacement in the direction denoted by its subscript, N_{ij} ($i, j = r, \theta,$ z) is the in-plane force, β is the rotating angle, and k' is the shear coefficient. The shear coefficient can be expressed for a circular pipe as [47]

$$k'=\frac{6(1+\nu)(1+(\frac{r_i}{r_o})^2)^2}{(7+6\nu)(1+(\frac{r_i}{r_o})^2)^2+(20+12\nu)(\frac{r_i}{r_o})^2}, \tag{2.75}$$

where r_i and r_o are the inner and outer radii of the circular pipe, respectively and ν is the Poisson's rato. Then, the assumed wave solutions of Eqs. (2.70) – (2.74) for a harmonic excitation can be written as

$$u_r=U_r e^{in\theta}e^{ikz}e^{-i\omega t}, \tag{2.76}$$

$$u_\theta=U_\theta e^{in\theta}e^{ikz}e^{-i\omega t}, \tag{2.77}$$

$$u_z=U_z e^{in\theta}e^{ikz}e^{-i\omega t}, \tag{2.78}$$

$$\beta_\theta=B_\theta e^{in\theta}e^{ikz}e^{-i\omega t}, \tag{2.79}$$

$$\beta_z=B_z e^{in\theta}e^{ikz}e^{-i\omega t}. \tag{2.80}$$

By substituting Eqs. (2.76) – (2.80) into Eqs. (2.70) – (2.74), an eigenvalue problem can be formulated as

$$\mathbf{Z}\begin{bmatrix}U_r & U_\theta & U_z & B_\theta & B_z\end{bmatrix}^{\mathrm{T}}=\mathbf{0}. \tag{2.81}$$

For a non-trivial solution, the determinant of the matrix **Z** in Eq. (2.81) should be zero: i.e.,

$$\left|\mathbf{Z}(k,\omega)\right| = 0\,. \tag{2.82}$$

By solving Eq. (2.82), the dispersion relations can be obtained and they are overlaid in Fig. 10. The HAFEM dispersion curves are matched well with those obtained from the shell theory which includes the coupling effects between propagation waves. Since there is no specific assumption for HAFEM, its results are expected to be more accurate than those of the Bernoulli-Euler theory which is valid only for the thin beams.

In addition, the dispersion relations in the water-filled pipe are also presented in Fig. 10 with the water properties in Table 6. When water is filled inside the pipe, the wavenumber increases at each frequency as shown in Fig. 12 and, therefore, the associated phase speed decreases.

2.3.3 Dispersion Relations in Ultrasonic Frequencies

In order to validate the HAFEM procedure in an ultrasound frequency range, the dispersion curves for the axisymmetric, longitudinal modes obtained from a HAFEM model are compared with the results presented in Ref. [7]. The material properties and geometry information of the water-filled pipe in Ref. [7] are presented in Table 7. For the HAFEM model, 9 nodes in the *r*-direction for the pipe structure, 11 nodes in the *r*-direction for water, and 36 nodes in the θ-direction are used. Thus, the total of 684 (= (9+11-1)×36) nodes are used for this model. The dispersion curves of both the empty and water-filled cases are presented in Fig. 11. It is shown that the dispersion curves

obtained from the proposed HAFEM agree well with the dispersion curves presented in Ref. [7].

Young's Modulus [GPa]	113.6
Density [kg/m^3]	7100
Thickness [mm]	16
Outer radius [mm]	143
Poisson's ratio	0.28

Table 7: Material properties of pipe in Fig. 11 and Ref. [7].

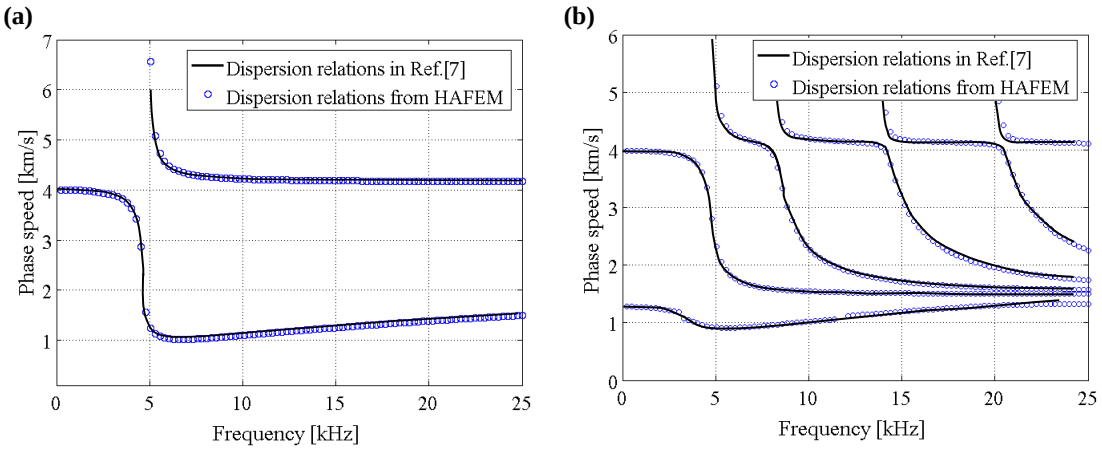

Figure 11: Comparison of dispersion curves for axisymmetric, longitudinal wave modes: **(a)** Empty case and **(b)** Water-filled case.

In addition to the dispersion curves of the axisymmetric, longitudinal modes in Fig. 11, the dispersion curves of the longitudinal wave modes for the same material properties and geometries in Tables 5 and 6 are estimated from the HAFEM model up to 200 kHz. The dispersion curves for longitudinal modes are shown in Fig. 12. When the pipe is filled with water, as shown in Fig. 12(b), the second mode of the hollow pipe is

separated to several modes and an additional mode, that is referred to as the α mode [7], can be observed. In low frequencies (e.g., below 30 kHz), the phase speed of this α mode converges to the non-dispersive leak noise propagation velocity defined as [7].

$$V = c_L \left(1 + \frac{\kappa 2a}{Ed}\right)^{-1/2}, \tag{2.83}$$

where κ is the bulk modulus of water, a is the radius of the inner pipe, d is the thickness of the pipe, and c_L is the wave speed in water.

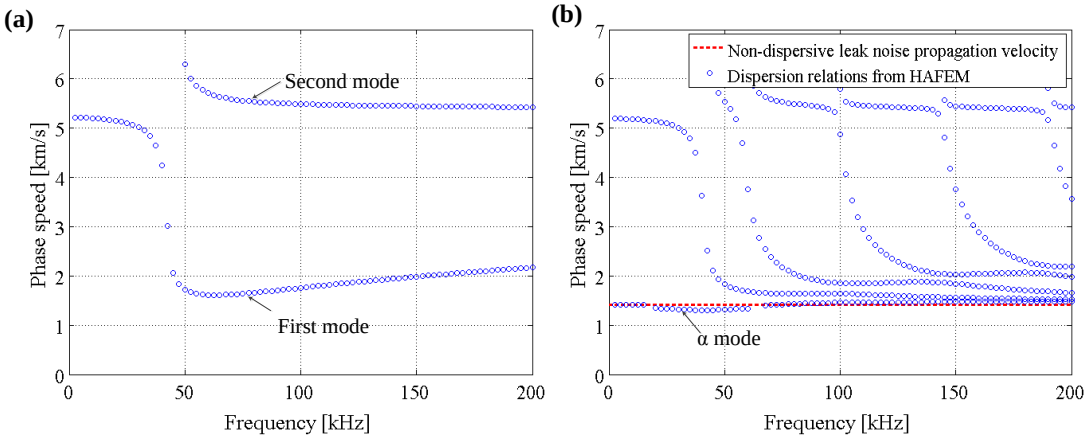

Figure 12: Dispersion curves for longitudinal wave modes obtained by using HAFEM: **(a)** Empty case and **(b)** Water-filled case.

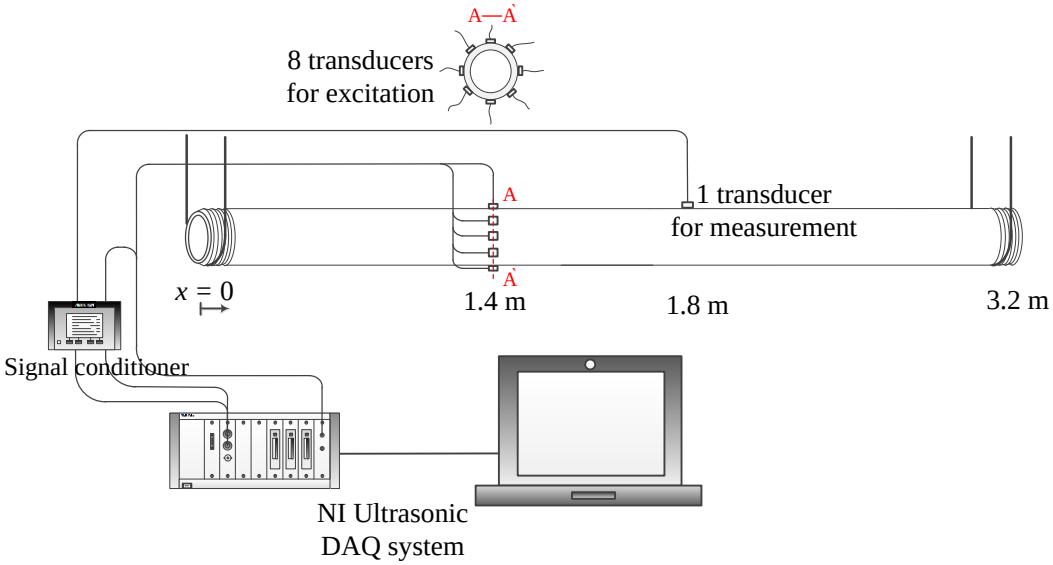

Figure 13: Experimental setup for measuring ultrasonic wave speeds in hollow pipe.

In order to validate the proposed HAFEM modeling procedure experimentally, as shown in Fig. 13, the eight piezoelectric transducers (APC-851 manufactured by APC International, Ltd.) are attached to the pipe in the circumferential direction to generate longitudinal modes. The material properties and geometric information of this pipe are same as the previous simulation case in Table 5 and the size of each transducer is 7 × 7 mm. The excited waves are then propagating and measured by using a transducer placed 40 cm apart from the excitation transducers. A National Instruments (NI) system equipped with a PXIe-5122 ultrasonic data acquisition (DAQ) module, a PXI-5421 signal generator, and an in-house LabView code is used to generate a burst sinusoidal wave. A Brüel & Kjæ r Type 2693 Nexus conditioning amplifier is used to amplify the measured ultrasonic wave signals before the signals are fed to the NI DAQ system. The measured ultrasonic wave signals are recorded for 0.05 seconds at the sampling

frequency of 20 MHz. In order to compensate a time-lag from the signal conditioner, the excitation signals are also measured to the NI DAQ system through the signal conditioner as described in Fig. 13. In order to determine the wave speeds of the longitudinal modes, the Hilbert transformation is applied to the measured signals as shown in Figs. 14(a) and 14(b) to extract the envelopes of the measured signals and then the peak envelope locations are used to calculate group velocities. The group velocity can be obtained by using a finite difference approximation as [48]

$$f \approx \frac{f_1 + f_2}{2}, \quad v_g = \frac{\partial \omega}{\partial k} \approx \frac{\omega_2 - \omega_1}{k_2 - k_1}, \tag{2.84}$$

where the subscripts represent two adjacent data points. The dispersion curves in terms of the group velocity in Fig. 14(c) are obtained by applying Eq. (2.84) with $\Delta f = f_2 - f_1 =$ 5 kHz to the HAFEM results in Fig. 12(a). Figure 14(c) shows that the measured group velocities are well matched to the HAFEM-predicted group velocities.

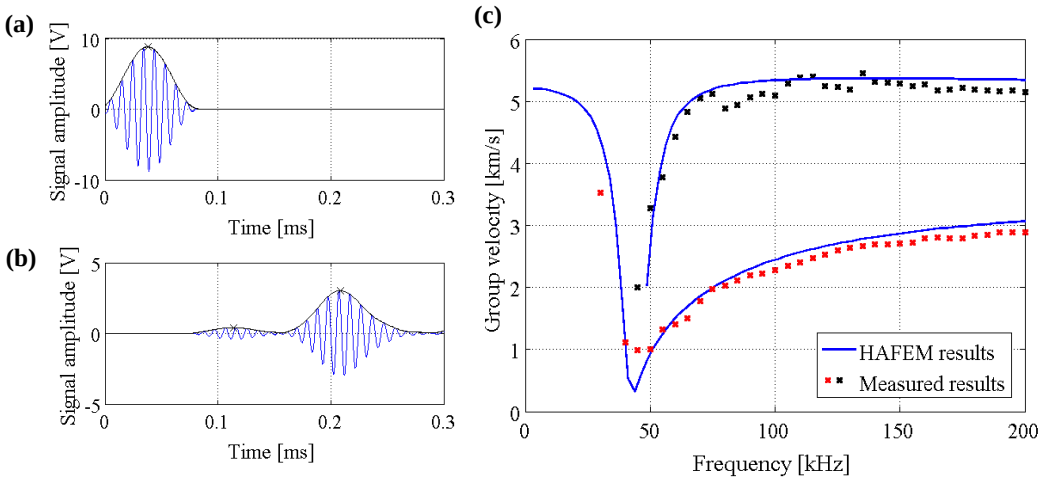

Figure 14: Measured wave signals and dispersion curves: **(a)** Excitation signals, **(b)** Measured signal, and **(c)** Comparison of experimental and HAFEM-predicted dispersion curves.

2.4 HAFEM-Based Acoustic Transfer Function Approach for Modeling Multi-Cross-Sectional Pipe System

Although the HAFEM modeling is useful to understand the wave propagation characteristics of fluid-filled, multi-layered composite pipes with arbitrary cross-sections, the cross-sectional shapes should not change in the axial direction. In order to consider a pipe system assembled with multiple pipe sections with different cross-sections, an acoustic transfer matrix is derived from the HAFEM formation.

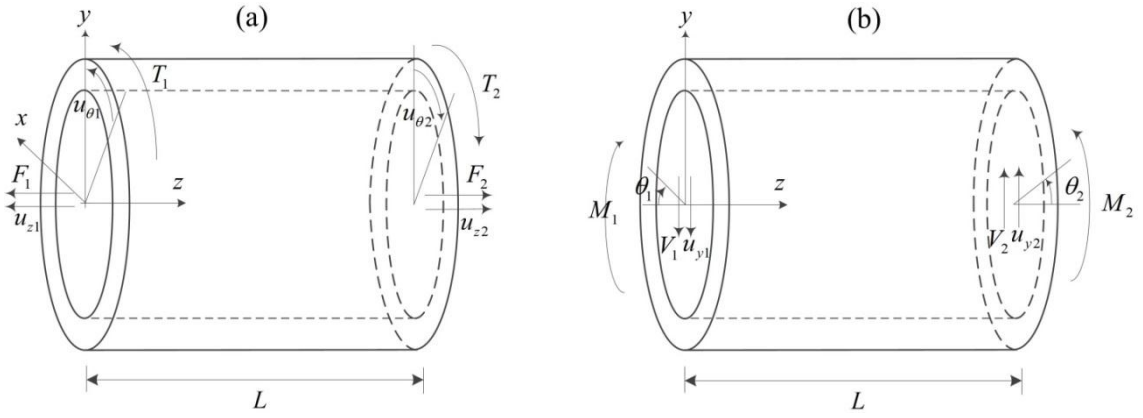

Figure 15: Sign convention of acoustic variables: (a) Longitudinal and torsional waves and (b) Flexural waves.

As presented in Sections 2.2 and 2.3, an analytical solution is assumed in the axial direction (i.e., *z*-direction) while FE approximations are applied to the cross-section of a pipe or joint (see Fig. 6). Since the displacements are approximated by combining the nodal displacements and quadratic interpolation functions in the cross-sectional directions, there are nine nodes in one element. By solving a characteristics equation at

each frequency, the wavenumbers for the longitudinal, torsional, flexural waves are obtained. Then, an acoustic transfer matrix between two axial locations is derived by using three wave equations. The sign convention for an acoustic transfer matrix is described in Fig. 15.

2.4.1 Longitudinal Wave

For the pipe system in Fig. 15, the longitudinal equation [38] is represented as

$$\frac{\partial^2 u_z}{\partial z^2} = \frac{1}{c_L^2}\frac{\partial^2 u_z}{\partial t^2}, \tag{2.85}$$

where c_L (=$(E/\rho)^{1/2}$) is the longitudinal wave speed and u_z is the displacement in the z-direction. The assumed solution for Eq. (2.85) can be expressed as

$$u_z = (B_1 e^{ik_{L+}z} + B_2 e^{ik_{L-}z})e^{-i\omega t}, \tag{2.86}$$

where k_{L+} and k_{L-} are obtained at each angular frequency ω in Section 2.3.2. The longitudinal wave solution in Eq. (2.86) is based on the assumption that only plane waves are propagating through the pipe section. That is, except for the longitudinal, torsional, flexural wave modes, other wavenumbers that have large imaginary parts in low frequencies are ignored. By using the axial force and displacement relation, $F = -EA\partial u_z/\partial z$ and Eq. (2.86) at $z = 0$ and L, the relations between the axial displacements and the axial forces at the two z-locations can be expressed in a matrix form as

$$\begin{bmatrix} u_{z2} \\ F_2 \end{bmatrix} = \frac{1}{k_{L+} - k_{L-}} \begin{bmatrix} -k_{L-}\mathrm{e}^{ik_{L+}L} + k_{L+}\mathrm{e}^{ik_{L-}L} & \frac{i}{EA}(\mathrm{e}^{ik_{L+}z} - \mathrm{e}^{ik_{L-}z}) \\ k_{L-}\mathrm{EA}ik_{L+}\mathrm{e}^{ik_{L+}z} - k_{L+}\mathrm{EA}ik_{L-}\mathrm{e}^{ik_{L-}z} & k_{L+}\mathrm{e}^{ik_{L+}z} + k_{L-}\mathrm{e}^{ik_{L-}z} \end{bmatrix} \begin{bmatrix} u_{z1} \\ F_1 \end{bmatrix}, \quad (2.87)$$
$$= \mathbf{T}_L \begin{bmatrix} u_{z1} \\ F_1 \end{bmatrix}$$

where A is the cross-sectional area. Since k_{L+} and k_{L-} are calculated at each angular frequency ω by solving Eq. (2.58), the resulting axial displacements and forces in Eq. (2.87) are also a function of ω.

2.4.2 Torsional Wave

The torsional wave equation [38] can be represented as

$$\frac{\partial^2 u_\theta}{\partial z^2} = \frac{1}{c_T^2}\frac{\partial^2 u_\theta}{\partial t^2}, \quad (2.88)$$

where $c_T = (G/\rho)^{1/2}$ is the torsional wave speed and u_θ is the torsional angular displacement as described in Fig. 15(a). By using $T = -J\partial u_\theta/\partial z$, similar to the procedure in Section 2.4.1, the relations between the angular displacements and the torsional moments at $z = 0$ and L can be obtained as

$$\begin{bmatrix} u_{\theta 2} \\ T_2 \end{bmatrix} = \frac{1}{k_{T+} - k_{T-}} \begin{bmatrix} -k_{T-}\mathrm{e}^{ik_{T+}L} + k_{T+}\mathrm{e}^{ik_{T-}L} & \frac{i}{J}(\mathrm{e}^{ik_{T+}z} - \mathrm{e}^{ik_{T-}z}) \\ k_{T-}\mathrm{J}ik_{T+}\mathrm{e}^{ik_{L+}z} - k_{T+}\mathrm{J}ik_{T-}\mathrm{e}^{ik_{T-}z} & k_{T+}\mathrm{e}^{ik_{T+}z} + k_{T-}\mathrm{e}^{ik_{T-}z} \end{bmatrix} \begin{bmatrix} u_{\theta 1} \\ T_1 \end{bmatrix}, \quad (2.89)$$
$$= \mathbf{T}_T \begin{bmatrix} u_{\theta 1} \\ T_1 \end{bmatrix}$$

where k_{T+} and k_{T-} are obtained at each angular frequency ω as described in Section 2.3.2 and J is the torsional rigidity of the system.

2.4.3 Flexural Wave

The flexural wave equation [38] can be expressed as

$$EI_{FR}\frac{\partial^4 u_y}{\partial z^4}+\rho A\frac{\partial^2 u_y}{\partial t^2}=0, \tag{2.90}$$

where u_y is the transverse displacement as shown in Fig. 15(b) and I_{FR} is the area moment of inertia. Then, the flexural wave solution of Eq. (2.90) can be assumed as

$$u_y=(C_1\mathrm{e}^{ik_{FR+}z}+C_2\mathrm{e}^{ik_{FR-}z}+C_3\mathrm{e}^{ik_{FI+}z}+C_4\mathrm{e}^{ik_{FI-}z})\mathrm{e}^{-i\omega t}. \tag{2.91}$$

Then, the flexural wave variables at $z = L$ is expressed as

$$\begin{aligned}\begin{pmatrix}u_{y2}\\ \theta_2\\ M_2\\ V_2\end{pmatrix}&=\begin{bmatrix}1 & 1 & 1 & 1\\ ik_{FR+} & ik_{FR-} & ik_{FI+} & ik_{FI-}\\ -EI_{FR}k_{FR+}^2 & -EI_{FR}k_{FR-}^2 & -EI_{FR}k_{FI+}^2 & -EI_{FR}k_{FI-}^2\\ iEI_{FR}k_{FR+}^3 & iEI_{FR}k_{FR-}^3 & iEI_{FR}k_{FI+}^3 & iEI_{FR}k_{FI-}^3\end{bmatrix}\begin{bmatrix}\mathrm{e}^{ik_{FR+}z} & 0 & 0 & 0\\ 0 & \mathrm{e}^{ik_{FR-}z} & 0 & 0\\ 0 & 0 & \mathrm{e}^{ik_{FI+}z} & 0\\ 0 & 0 & 0 & \mathrm{e}^{ik_{FI-}z}\end{bmatrix}\begin{pmatrix}C_1\\ C_2\\ C_3\\ C_4\end{pmatrix}\\ &=\mathbf{T}_{F1}\mathbf{T}_{F2}\begin{bmatrix}C_1 & C_2 & C_3 & C_4\end{bmatrix}^{\mathrm{T}}\end{aligned}, \tag{2.92}$$

where

$$\theta=\frac{\partial u_y}{\partial z}, \tag{2.93}$$

$$M=EI_{FR}\frac{\partial^2 u_y}{\partial z^2}, \tag{2.94}$$

$$V=-EI_{FR}\frac{\partial^3 u_y}{\partial z^3}. \tag{2.95}$$

The four coefficients C_1 to C_4 can be expressed by using the flexural wave variables at z = 0 and the relation between the flexural wave variables at z = 0 and L is then obtained as

$$\begin{pmatrix} u_{y2} \\ \theta_2 \\ M_2 \\ V_2 \end{pmatrix} = \mathbf{T}_{F1}\mathbf{T}_{F2}\mathbf{T}_{F1}^{-1} \begin{pmatrix} u_{y1} \\ \theta_1 \\ M_1 \\ V_1 \end{pmatrix}. \tag{2.96}$$

2.4.4 Acoustic Transfer Matrix

By combining Eqs. (2.87), (2.89), and (2.96) into a single matrix form, the 8×8 acoustic transfer matrix **T** can be obtained as

$$\mathbf{U}_{z=L} = \begin{bmatrix} \mathbf{T}_L & \vec{0} & \vec{0} \\ \vec{0} & \mathbf{T}_T & \vec{0} \\ \vec{0} & \vec{0} & \mathbf{T}_{F1}\mathbf{T}_{F2}\mathbf{T}_{F1}^{-1} \end{bmatrix} \mathbf{U}_{z=0} = \mathbf{T}\mathbf{U}_{z=0}, \tag{2.97}$$

where

$$\mathbf{U} = \left[u_z \; F \; u_\theta \; T \; u_y \; \theta \; M \; V \right]^{\mathrm{T}}. \tag{2.98}$$

In Eq. (2.97), the matrices $\mathbf{T}_L$, $\mathbf{T}_T$, $\mathbf{T}_{F1}$, **and** $\mathbf{T}_{F2}$ are defined in Eqs. (2.87), (2.89), and (2.96). For a fluid-filled pipe system with multiple pipe sections and joints, the total acoustic transfer matrix can be determined by multiplying all individual acoustic transfer matrices, each is obtained from a single pipe or joint. Therefore, once a measurement is done at one end of the combined system, the acoustic wave variables at the other end can be estimated from the total acoustic transfer matrix without a measurement at this end.

Furthermore, by controlling the length of a pipe virtually, with acoustic data measured at one end, the acoustic wave variables at arbitrary points can be also estimated.

2.4.5 Validation Cases: Two Hollow Pipes Connected by Joint

The experimental setup is shown in Fig. 16. Two empty pipes with the same cross-section are connected with a joint in the middle and the combined pipe system is hanged by using two steel cables at z = 2.94 m and 6.80 m. Table 8 shows the geometric dimensions and the material properties of the pipe system. The damping coefficient in Table 8 is obtained by using Eq. (2.69) and applying the half power method to the experimental data.

By exciting the left end of the pipe using a Brüel & Kjær (B&K) Type 8206 impact hammer, longitudinal and flexural waves are generated. For the purpose of generating the flexural waves, a vertical impact force is applied to the pipe end by using the impact hammer. In order to generate the longitudinal waves, after attaching a circular cover to the left end of the pipe, the impact hammer then is used to excite the center of the glued circular cover.

With a PCB Piezotronics "triaxial" accelerometer (Model: 356A24) attached on the pipe, the acceleration data is measured for 8 seconds at a sampling frequency of 1600 Hz by using a B&K PULSE system (Model: 3560-B-130). Three-directional accelerations for the axial and transversal excitation cases are measured at 4 measurement points at z = 0 m, 2.13 m, 4.84 m, and 9.75 m as shown in Fig. 16.

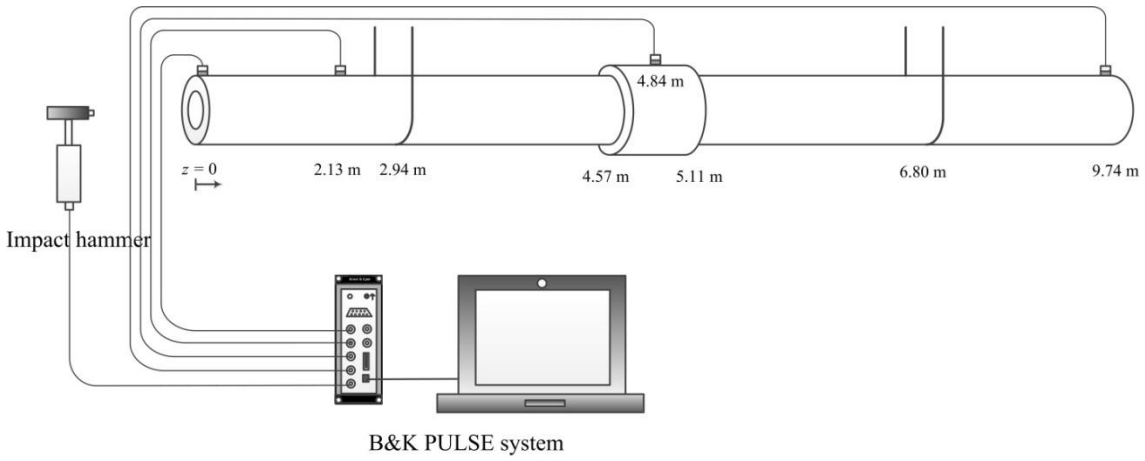

Figure 16: Experimental setup for two hollow pipes connected by joint case.

	Pipe	Joint
Young's Modulus [Pa]	2.08×10^{11}	
Density [kg/m^3]	7856	
Structural damping coefficient	0.0044	
Outer diameter [mm]	73.03	104.78
Inner diameter [mm]	54.65	50.8

Table 8: Material properties and diameters of drill pipe system for experimental setup in Fig. 16.

In addition to validate the proposed method experimentally, finite element (FE) analyses are also performed by using a commercial FE software package, ANSYS. Since it is difficult to excite pure torsional waves experimentally, torsional wave cases are only validated by using the FE results. The material properties and geometry information listed in Table 8 are used to build a FE model of the pipe system illustrated in Fig. 16. The solid element of SOLID187 is used with 15443 nodes to build the FE model. The maximum axial space between two neighboring nodes of the FE model is

about 0.09 m. The maximum frequency of interest is 400 Hz and the flexural waves have the slowest axial-direction phase speed of 610 m/s in this frequency range. Therefore, the smallest wavelength at 400 Hz is 1.53 m and at least 16.9 nodes per one wavelength are guaranteed, which are enough number of nodes for an accurate FE result. A longitudinal force of 1 N, a torsional moment of 1 N·m, and a vertical force of 1 N are exerted to the left end surface for the longitudinal, torsional, and transversal excitation. By using a harmonic solver in ANSYS, the FRF results at four acceleration locations (i.e., z = 0 m, 2.13 m, 4.84 m, and 9.74 m) are calculated up to 400 Hz with the frequency resolution of 2 Hz.

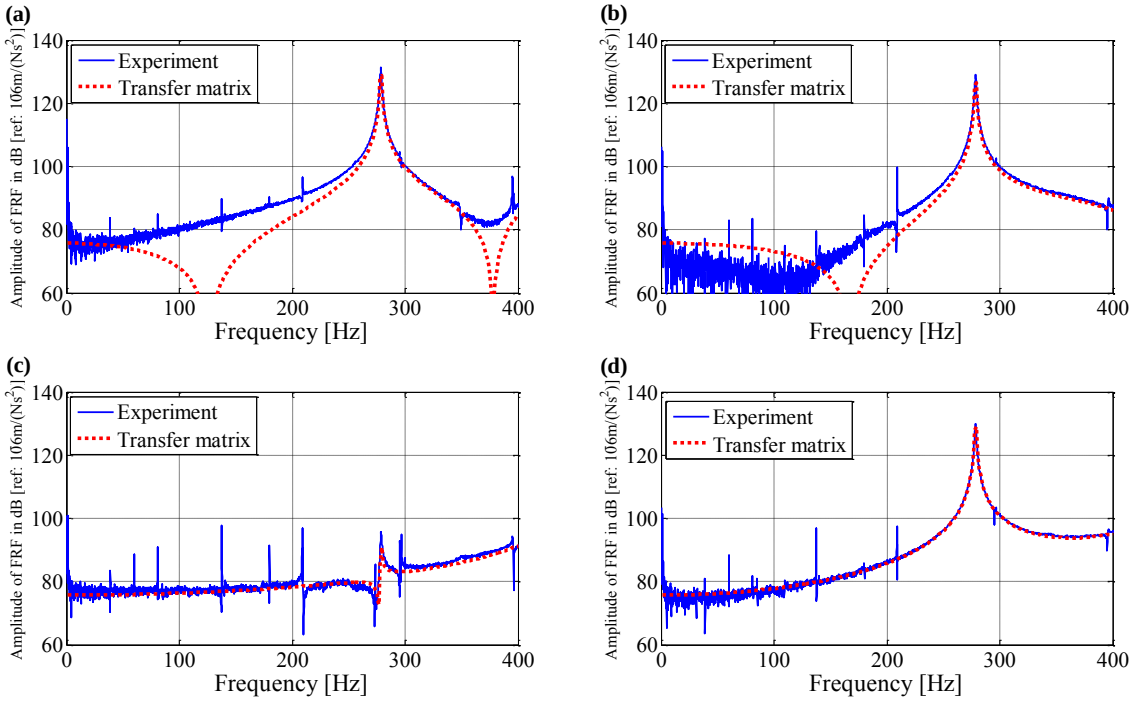

Figure 17: Experimental and HAFEM-predicted FRF results for "longitudinal" excitation case (L = 9.74 m): **(a)** z = 0, **(b)** z = 0.219L, **(c)** z = 0.5L, and **(d)** z = L.

The HAFEM model is built with 160 nodes (i.e. 5 nodes in the r-direction $\times$ 16 nodes in the θ-direction $\times$ 2 pipe/connector sections). For the "longitudinal" excitation cases, the FRFs in Fig. 17 estimated by using the proposed HAFEM-based transfer matrix method agree well with the experimental FRF results except for some valley locations at approximately 140 Hz, 160 Hz, and 380 Hz in Fig. 17(a) and 17(b). Due to the low signal to noise ratio (SNR) and the high sensitivity of accelerometer position error at these valley locations (i.e. anti-resonance locations), the measured amplitudes at the anti-resonance locations are expected to be imprecise. For the FRFs at the accelerometer locations of z = 0 m, 2.19L, and L, there are the large longitudinal peaks at about 280 Hz while this peak becomes small at the joint (i.e., z = 0.5L) as shown in Fig. 17.

For the "torsional" excitation case in Fig. 18, the FRFs obtained from the proposed HAFEM-based method are also well in line with the ANSYS analysis results.

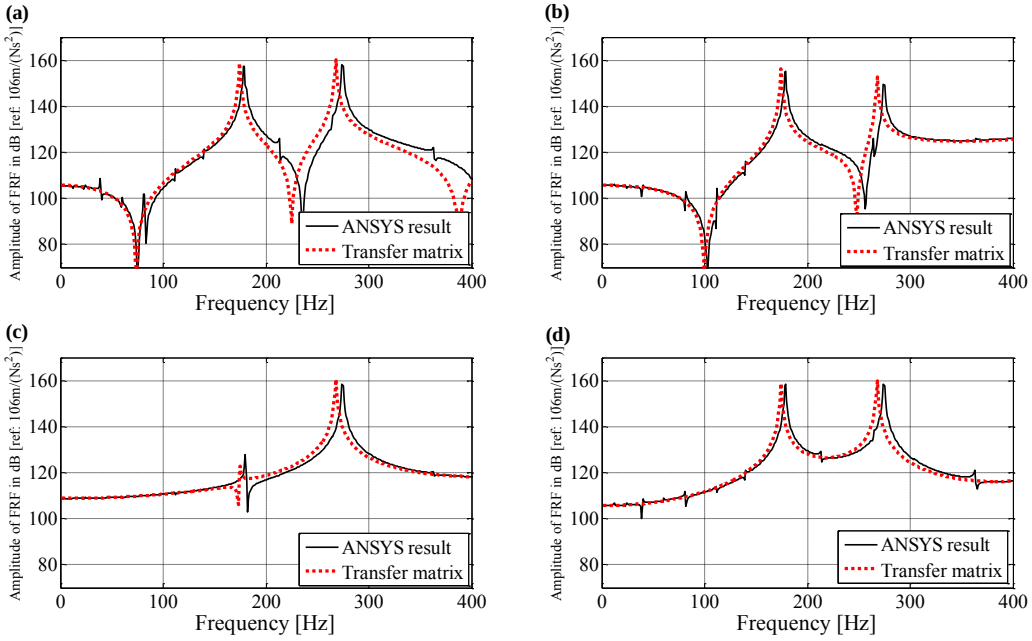

Figure 18: ANSYS and HAFEM-predicted FRF results for "torsional" excitation case (L = 9.74 m): **(a)** z = 0, **(b)** z = 0.219L, **(c)** z = 0.5L, and **(d)** z = L.

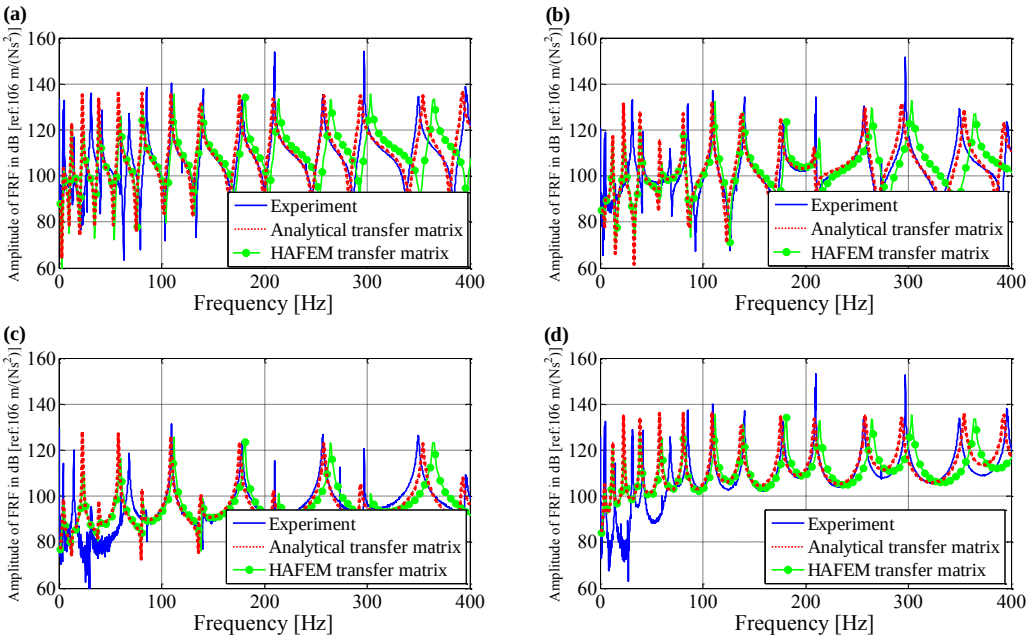

Figure 19: Experimental, HAFEM-predicted, and ANSYS FRF results at for "flexural" excitation case (L = 9.74 m): **(a)** z = 0, **(b)** z = 0.219L, **(c)** z = 0.5L, and **(d)** z = L.

For the "flexural" excitation case in Fig. 19, there is the discrepancy between the predicted and measured results at low frequencies (e.g., below 100 Hz). Since the pipe system is hanged by using two steel cables as described in Fig. 16, it cannot be assumed as a free-free boundary condition, in particular, in the low frequencies, while the predicted FRFs are based on the free-free boundary condition. However, at the high frequencies above 100 Hz, the discrepancy becomes insignificant and the predicted FRF results agree well with the experimental results. As shown in Fig. 10, the wavenumbers obtained from the HAFEM model and the analytical solution (i.e., $k = (\omega^2 \rho A/E/I)^{1/4}$) are slightly different. In order to investigate these differences in detail, the analytical FRF results are also plotted in Fig. 19. At the high frequencies above 250 Hz, the HAFEM-predicted FRFs are matched better to the measured results than the analytical FRF results since the HAFEM model can be used to predict the wavenumbers more accurately than the analytical solution based on the Bernoulli–Euler beam theory which is valid for thin structures.

	Resonance frequency [Hz]								Σ|Difference|
Experiment	110	140	178	209	257	297	350	396	Baseline
HAFEM Transfer matrix	109	138	176	208	258	294	354	393	17
ANSYS	112	139	181	214	264	303	365	409	52

Table 9: Resonance peak frequencies and frequency differences of flexural wave case in Fig. 19.

In Table 9, the resonance frequencies obtained from the HAFEM-based transfer matrix approach, the ANSYS analysis, and the experiment and their frequency differences from the experimental resonance frequencies are presented. The proposed, HAFEM-based acoustic transfer matrix approach generates the best results matched to the measured data with the total frequency difference of 17 Hz, while the ANSYS approach results in the frequency difference of 52 Hz. For in-plane motions such as longitudinal and torsional waves, attenuations in a real pipe system are small. In ref. 49, by performing field tests of a drill pipe system, the longitudinal signal attenuation of 4 dB/1000 ft is calculated. Therefore, the proposed approach can estimate vibration responses of a long pipe system.

2.4.6 Validation Case: Fluid-Filled Single Pipe

The experimental setup with a water-filled pipe is shown in Fig. 20. The 1.83 m pipe is hanged by using two steel cables at z = 0.3 m and 1.53 m. Table 5 shows the material properties of the pipe. The density of the pipe is determined by measuring its weight and dimensions. The Young's modulus is decided by fitting predicted and measured natural frequencies for a longitudinal excitation with the empty pipe condition and the damping coefficient is obtained by applying Eq. (2.69) and the half power method to the experimental data.

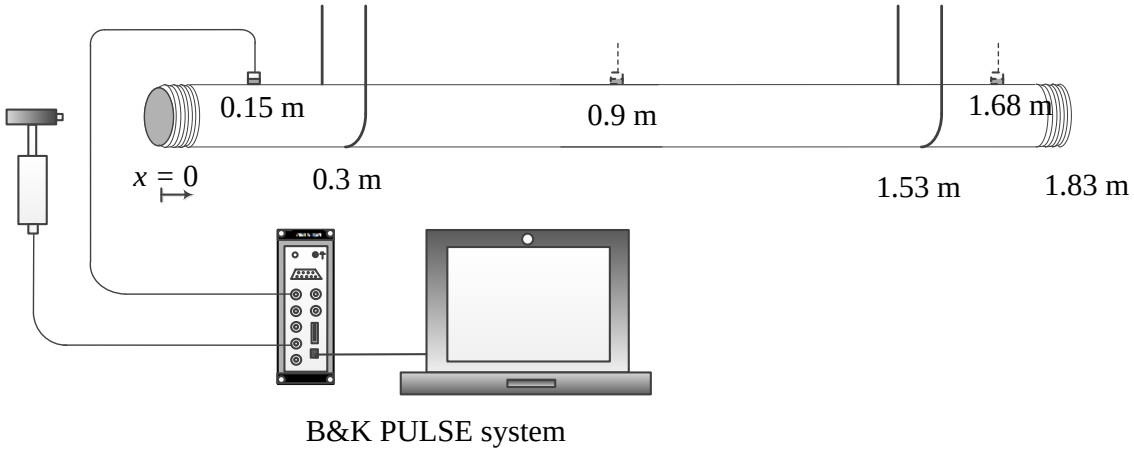

Figure 20: Experimental setup with fluid-filled single pipe.

Similarly as in Section 2.4.5, the longitudinal and flexural waves are generated by exciting the left end of the pipe using a Brüel & Kjæ r (B&K) Type 8206 impact hammer. For the purpose of generating the flexural waves, a vertical force is applied to the pipe end by using the impact hammer. In order to generate the longitudinal waves, a circular cover is glued to the left end of the pipe and the impact hammer is then used to excite the center of the glued circular cover. On the other side of the water-filled pipe, a thin plastic wrap is installed by using a thin steel cable and tape to hold water, minimizing additional mass effects.

The acceleration data is measured by attaching a PCB Piezotronics "triaxial" accelerometer (Model: 356A24) on the pipe for 2 seconds at a sampling frequency of 6400 Hz. A B&K PULSE system (Model: 3560-B-130) is connected to the accelerometer for acquiring three-directional accelerations for the axial and transversal excitation cases at the three measurement points at z = 0.15 m, 0.9 m, and 1.68 m as

shown in Fig. 20. Ten measurements are repeatedly made at each location and linearly averaged.

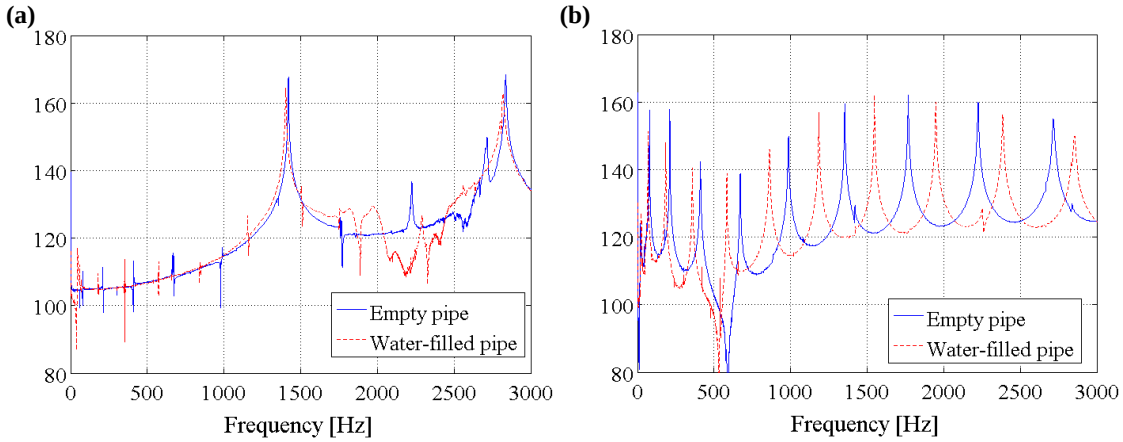

Figure 21: Experimental FRF results at z = 0.15 m: **(a)** "Longitudinal" excitation and **(b)** "Flexural" excitation.

In order to see the effects of the water inside the pipe, the measured FRFs for both the empty and water-filled pipe cases are compared in Fig. 21. The resonance frequencies, in particular, for the flexural wave excitation case decrease when the pipe is filled with water as shown in Fig. 21(b) although this frequency shift is insignificant for the longitudinal excitation case in Fig. 21(a).

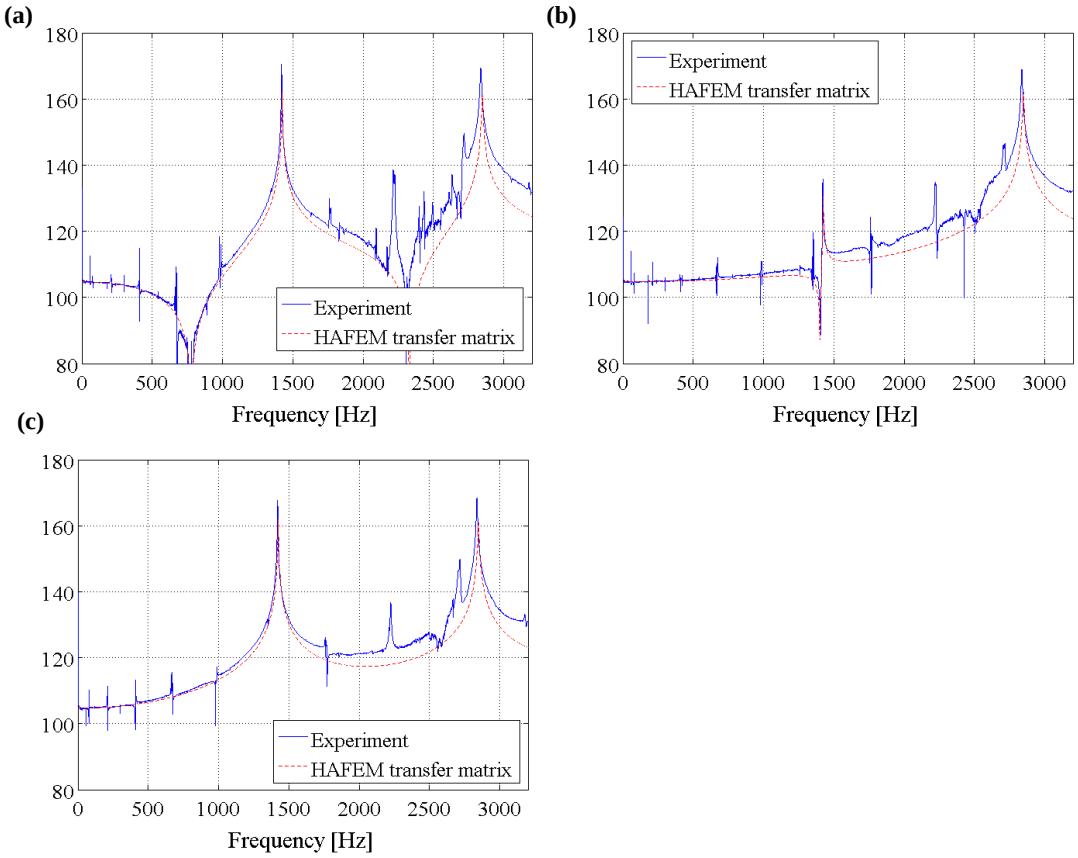

Figure 22: Experimental and predicted FRF results of empty pipe for "longitudianl" excitation case: **(a)** z = 0.15 m, **(b)** z = 0.9 m, and **(c)** z = 1.68 m.

For the empty pipe case, the experimental results are compared with the HAFEM-estimated results. As shown in Fig. 22, these two results are well aligned with each other.

In Fig. 23, the FRFs of the water-filled pipe are estimated by using the proposed HAFEM-based acoustic transfer function approach and compared with the experimental results. Although the resonance frequencies are shift significantly, in particular, for the flexural excitation case as shown in Fig 21 (b) when the pipe is filled with water, the

HAFEM estimates the FRFs of the water filled pipe precisely. Unlike the previous results for the flexural excitation case in Section 2.4.5, the FRF results match well at even low resonance frequencies. The weight of the multi-sectional pipe system in Section 2.4.5 is about 150 kg while that of this single pipe is only about 5.84 kg. Therefore, the reaction forces at the cable hanging positions of the multi-sectional pipe system cannot be ignored when compared to the impact excitation force. Thus, the multi-sectional pipe system cannot be assumed to have free-free boundary conditions, which results in the discrepancy in the low frequencies below 100 Hz. On the other hand, since the reaction forces in the single pipe are much smaller than the former case, the assumption of the free-free boundary conditions is valid even at the lowest resonance frequency.

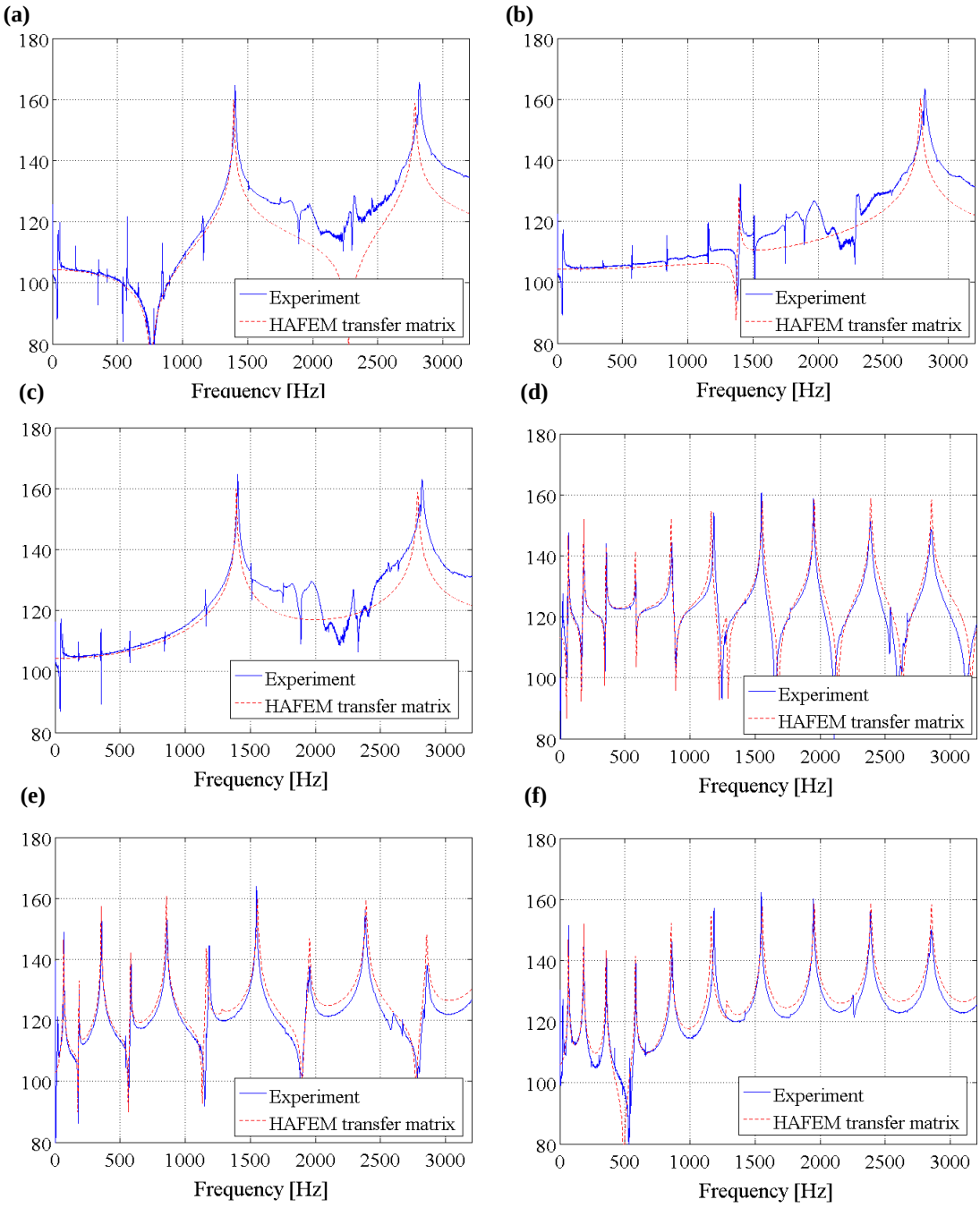

Figure 23: Experimental and predicted FRF results at for “longitudianl” excitation of the water-filled pipe: **(a)** z = 0.15 m, **(b)** z = 0.9 m, **(c)** z = 1.68 m and for “flexural” excitation of the water-filled pipe: **(d)** z = 0.15 m, **(e)** z = 0.9 m, and **(f)** z = 1.68 m.

3. TIME-FREQUENCY MUSIC FOR DETECTING STRUCTURAL DEFFECTS OF PLATE USING ULTRASONIC LAMB WAVE

3.1 Background

3.1.1 Beamforming-Based Nondestructive Evaluation

The basic idea of a beamforming procedure is to reconstruct a beamforming power map by comparing acoustic signals "measured" by using a transducer array with "assumed" acoustic signals radiated from a known free-field source placed at a scanning location. Here, the assumed acoustic signals can be represented as a vector that is referred to as the "steering vector". When a scanning location is coincident with the location of a "real" source, the beamforming power at this scanning location becomes a local maximum. By repeating the same procedure at all scanning points in a given space, the beamforming power map in the space can be reconstructed. Then, the local maximum locations on the reconstructed beamforming power map can be identified as the locations of the "real" sources. Therefore, the performance of the beamforming procedures is strongly dependent on how well the real acoustic field of interest can be represented by an assumed acoustic field. In general, acoustic monopoles and their combinations with anechoic or semi-anechoic boundary conditions are used to generate the assumed acoustic field.

The latter procedure can be used to detect both "active" and "passive" sources. An "active" source can generate acoustic waves actively, while a "passive" source can only

reflect an incident wave. In order to detect passive sources, an external source should be used to generate an acoustic wave and the waves reflected from the passive sources are measured by using a transducer array. Since structural damages can be considered as passive sources, they can be also detected by exciting an acoustic wave and measuring its reflected waves from the structural damages by using a transducer array.

3.1.2 Single Lamb Wave Mode Excitation

When multiple Lamb wave modes that have different wave speeds are excited, it is difficult to identify structural defect locations from measured reflection signals. Thus, it is required to generate a single Lamb wave mode whose wave speed is known prior to Non-Destructive Evaluations (NDEs).

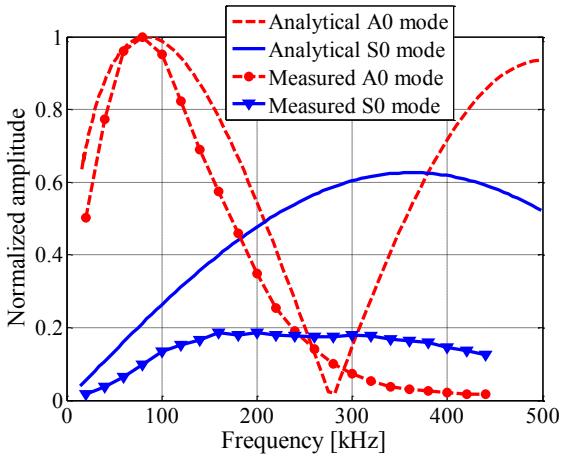

Figure 24: Normalized amplitudes of analytical and measured S0 and A0 Lamb wave modes.

In order to excite a single Lamb wave mode, two strain equations of a rectangular PWAS installed on a plate are considered in this section (see Ref. [21] and Appendix.A).

From these strain equations (i.e., Eqs. (A.8) and (A.9)), analytical strain responses can be found for a 7 mm PWAS glued on a 2.03 mm thick aluminum plate and plotted as a function of frequency in Fig. 24. The experimental results in Fig. 24 will be discussed in Section 3.6. The A0 mode (i.e., the first anti-symmetric mode represented by the dotted line in Fig. 24) is dominant at low frequencies (e.g., below 50 kHz), while the S0 mode (i.e., the first symmetric mode) of the solid line in Fig. 24 is dominant around 280 kHz for the given PWAS dimension, plate dimension, and plate material properties.

3.2 Theory

3.2.1 Time-frequency MUSIC Beamforming

Amongst various beamforming algorithms, the MUSIC beamforming algorithm [37] is widely used due to its high spatial resolution capability. Here, the proposed time-frequency MUSIC beamforming algorithm is applied to the time-averaged spectral (i.e., frequency) data obtained by applying the Discrete Fourier Transform (DFT) to a short period temporal (i.e., time) data at each specific time. The temporal signals including the direct excitation wave signals generated from an excitation and the reflective wave signals from defects and boundaries are assumed to be measured using M array transducers with a sampling frequency of f_s.

Assume that $x_m(t)$ is the measured time data at the m-th transducer. For a specific time at t_n, $\mathbf{x}_m(t_n)$ is defined as an instantaneous time data vector containing the N time data points of $x_m(t)$ where t_n is corresponding to the middle of the row vector. Then, in order to perform time-averaging for minimizing noise effects, this time data vector is

separated to J partial time data vectors. Each partial data vector has the length of D and is weighted with a time window such as the Hanning window. Note that the length of overlapped data points between two adjacent partial time data sets is generally set to 75 % (i.e., 0.75×D) for the Hanning window. Define the index of j to express the j-th partial time data vector among the total J partial time data vectors. In order to improve the frequency resolution of this short partial time data, it is recommended to extend the length of each partial time data vector to N_{fft} by applying zero-padding to the windowed partial time data vector. After applying the DFT to the j-th windowed and zero-padded partial data vector, a spectral vector $\mathbf{X}j$ can be obtained as

$$\mathbf{X}_j(t_n, f_l) = [X_{j,1}(t_n, f_l)\ \ X_{j,2}(t_n, f_l)\ X_{j,3}(t_n, f_l) \cdots X_{j,M}(t_n, f_l)]^{\mathrm{T}}\ , \qquad (3.1)$$

where the subscript l represents the frequency index. Then, by applying an averaging procedure, the $M \times M$ cross-spectral matrix $\mathbf{R}$ at a specific time, $t_{n,}$ and a specific frequency, f_l can be represented as

$$\mathbf{R}(t_n, f_l) = \frac{1}{J}\sum_{j=1}^{J} \mathbf{X}_j(t_n, f_l) \cdot \mathbf{X}_j^{\mathrm{H}}(t_n, f_l)\,. \qquad (3.2)$$

The Singular Value Decomposition (SVD) is applied to the cross-spectral matrix in Eq. (3.2): i.e.,

$$\mathbf{R}(t_n, f_l) = \mathbf{U}(t_n, f_l)\mathbf{\Sigma}(t_n, f_l)\mathbf{V}^{\mathrm{H}}(t_n, f_l)\,. \qquad (3.3)$$

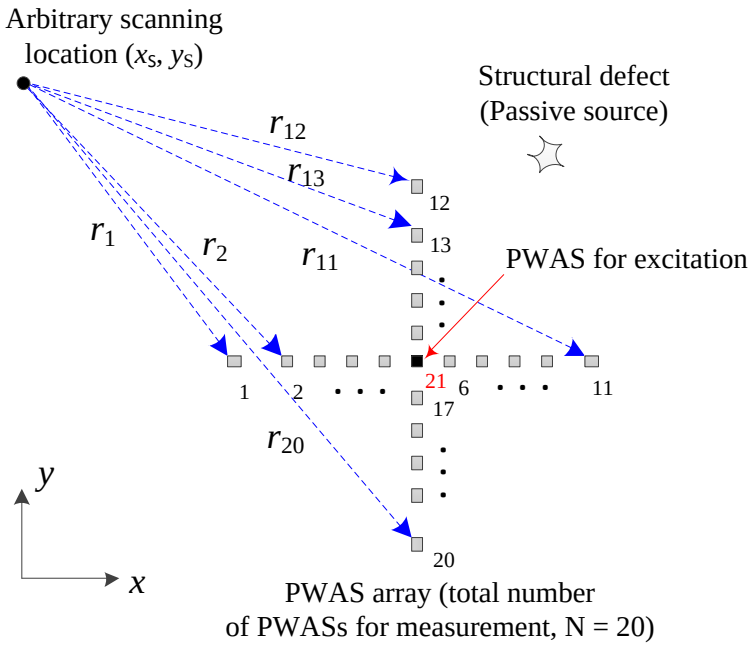

Figure 25: Illustration of arbitrary scanning location, (xs,ys) with respect to PWAS array (the black PWAS is used for excitation and the others, for measuring ultrasonic wave signals).

The time-frequency MUSIC power is then calculated at each scanning point as

$$P_{\text{MUSIC}}(t_n, f_l, \mathbf{r}_s) = \frac{1}{\sum_{i=p+1}^{N} \left| \mathbf{g}^{\text{H}}(\mathbf{r}_s) \cdot \mathbf{u}_i(t_n, f_l) \right|^2}, \tag{3.4}$$

where **g** is the steering vector of the acoustic signals at the transducer locations calculated by placing a free-field source at the scanning location, $\mathbf{r}_s$ is the scanning location vector (for example, see Fig. 25) represented as

$$\mathbf{r}_s(x_s, y_s) = \left[r_1(x_s, y_s) \quad r_2(x_s, y_s) \quad \cdots \quad r_N(x_s, y_s) \right]^{\text{T}}, \tag{3.5}$$

$\mathbf{u}_i$ is the i-th column vector of the matrix $\mathbf{U}(t_n,f_l)$ in Eq. (3.3), and p is the dimension of the signal space. Thus, $\mathbf{u}_{p+1}$, $\mathbf{u}_{p+2}$, … , and $\mathbf{u}_N$ in the denominator of Eq. (3.4) are the noise subspace basis vectors. When the scanning location is coincident to the source location, the inner product between the steering vector and the noise subspace spanned by the noise subspace basis vectors in the denominator of Eq. (3.4) becomes a small value since they are orthogonal to each other. Then, the MUSIC power is locally maximized at this scanning location.

3.2.2 Wave Propagation Models and Steering Vector

Since the performance of the source localization by using a MUSIC beamforming algorithm strongly depends on how well a steering vector represents the spatial distribution of the acoustic field of interest, it is important to precisely model wave propagation characteristics of a plate structure in the steering vector. In this article, 3-D, 2-D, and 1-D analytical steering vectors are proposed to be investigated to identify the best steering vector among these three. These steering vectors represent spherical, cylindrical, and planar wave propagation models, respectively, in a reflection-free space: i.e.,

$$\mathbf{g} = [\frac{1}{r_1}\exp^{-ikr_1}\ \frac{1}{r_2}\exp^{-ikr_2}\ \cdots \frac{1}{r_N}\exp^{-ikr_N}]^{\mathrm{T}}, \tag{3.6}$$

$$\mathbf{g} = [\frac{1}{\sqrt{r_1}}\exp^{-ikr_1}\ \frac{1}{\sqrt{r_2}}\exp^{-ikr_2}\ \cdots \frac{1}{\sqrt{r_N}}\exp^{-ikr_N}]^{\mathrm{T}}, \tag{3.7}$$

$$\mathbf{g} = [\exp^{-ikr_1}\ \exp^{-ikr_2}\ \cdots \exp^{-ikr_N}]^{\mathrm{T}}. \tag{3.8}$$

These steering vectors behave well when the measurement surface is apart from the scanning surface where the singularity at $r = 0$ can be avoided in Eqs. (3.6) and (3.7). However, since the measurement and scanning surface are coincident in the simulation and experiment setups as described below, the assumed acoustic field represented by the steering vectors in Eqs. (3.6) and (3.7) becomes infinity at $r = 0$. Then, the MUSIC power in Eq. (3.4) becomes zero since the denominator containing the steering vector in Eq. (3.4) is infinity. For this reason, when a defect locates very close to the array, the resulting MUSIC power has an extremely small value at this defect location. In other words, the MUSIC power map shows the maximum value at a large r, which makes it impossible to have a local maximum MUSIC power at a defect location. In order to avoid this abnormality, it is proposed that the steering vector is normalized as

$$\mathbf{g}_{\text{normalized}} = \frac{\mathbf{g}}{\|\mathbf{g}\|}. \tag{3.9}$$

In addition to the geometrical wave decays associated with $1/r$ or $1/r^{0.5}$ in Eqs. (3.6) and (3.7), there is also a spatial decay induced by the structural damping. In this paper, a complex wave number is used in Eqs. (3.6) to (3.8) to describe the structural-damping-induced spatial decay: i.e.,

$$\bar{k} = k(1 - i\beta). \tag{3.10}$$

The relation between the spatial decay rate β and the structural damping coefficient η can be obtained by assuming that the A0 Lamb wave at a low ultrasonic frequency such as 20 kHz can be regarded as a flexural wave [50]: i.e., $\beta = \eta/4$. The detailed

derivation process of this relation is described in Appendix B. In this article, an optimal structural damping coefficient at ultrasonic frequencies of interest is determined by having the spatial resolution of the MUSIC power results maximized.

3.3 Simulation Result for Determining Array Shape

For the purpose of determining an array shape, nine numerical simulation cases with linear, circular, and cross-shaped arrays are performed. Table 10 shows the simulation conditions and Fig. 26 shows the simulation results.

In the simulations, a point acoustic source is assumed to be placed at each of its source locations (listed in Table 10) to generate a transient cylindrical wave field. The source locations are indicated by using the red "x" marks in Fig. 26. A burst sinusoidal signal with a center frequency of 20 kHz and a SNR of 10 dB is used to drive the point source.

Figure number	3(a)	3(b)	3(c)	3(d)	3(e)	3(f)	3(g)	3(h)	3(i)
Array shape	Line				Cross	Circle	Line	Cross	Circle
Source location, (x,y) [m]	(0.21, 0.7)			(0.21, 0.42)			(0.21, 0.7)		
Array center location, (x,y) [m]	(0.5, 0.42)			(0.6, 0.42)					
Array spacing [cm]	1	0.1	1						
Number of array sensors	20								
Structural damping in wave propagation	0.01								
Structural damping in steering vectors	0	0	0.01	0			0.01		

Table 10: Simulation conditions for MUSIC power result plots in Fig. 28.

The wave speed at this excitation frequency is assumed to be 615 m/s that is corresponding to the A0 Lamb wave speed in a 2 mm aluminum plate. The structural damping coefficient for this cylindrical wave is set to 0.01.

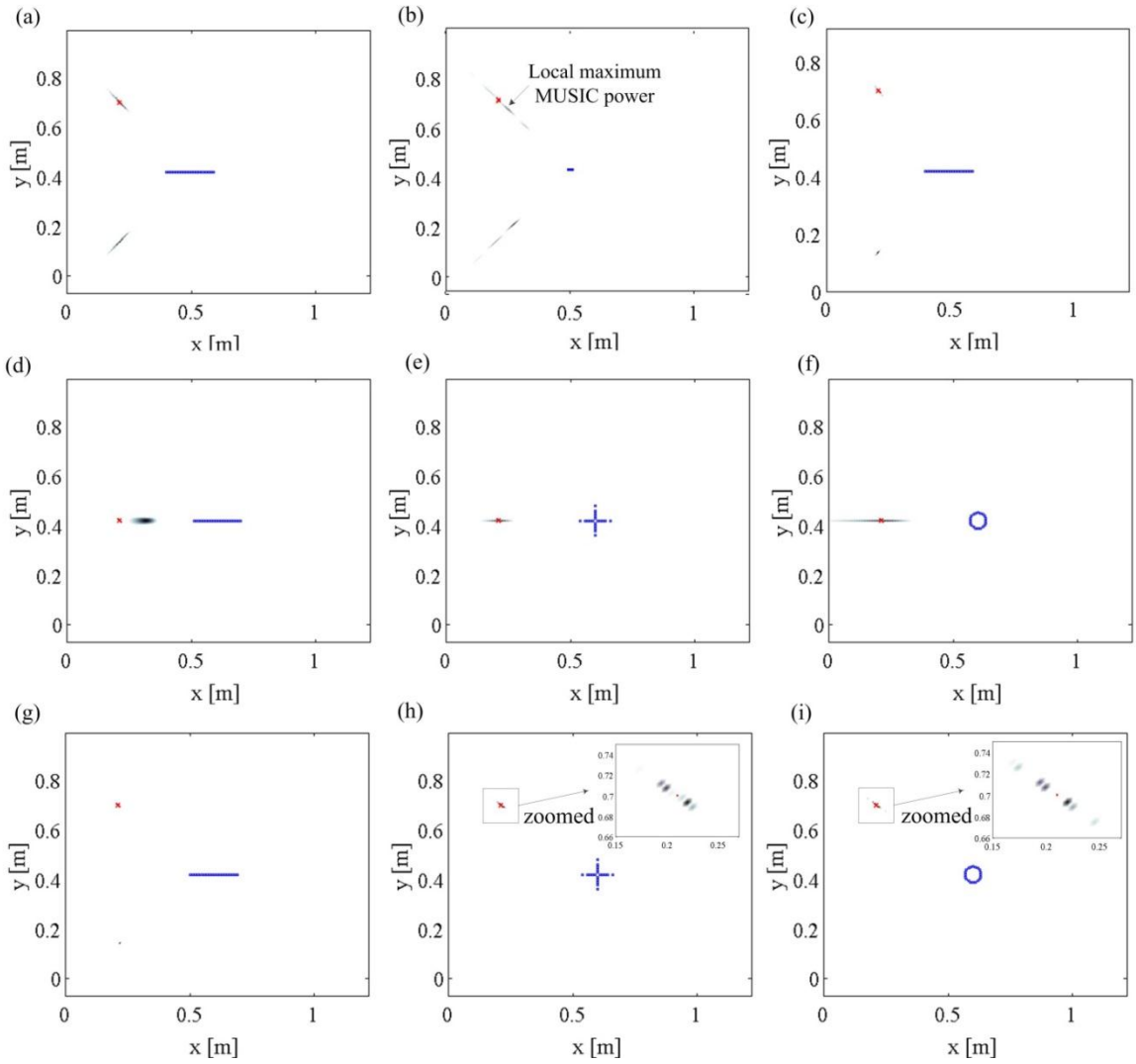

Figure 26: MUSIC power results of transient, cylindrical point source simulations with different array sizes and shapes. (refer to Table 10 for the detailed conditions)

A linear, circular, or cross-shaped array of 20 sensors is then used to measure the radiated cylindrical wave field. The linear array has the sampling space of 1 cm between two adjacent sensors as shown in Table 10 except that for Fig. 26(b), it has 0.1 cm sampling space. For the cross-shaped array, the sampling space is 1 cm except that its outer four sensors are placed 2 cm apart to increase its measurement aperture (see Fig. 25). The radius of the circular array, 3.2 cm, is determined to have the sampling space of 1 cm between two neighboring sensors. For all simulation cases, the sampling frequency is set to 10 MHz.

The normalized, cylindrical, 2-D steering vectors for calculating the MUSIC powers in these simulations are given in Eqs. (3.7), (3.9), and (3.10). For the cases of Figs. 26(a), 26(b), and 26(d) to 26(f) in Table 10, the structural damping coefficient is set to zero in the steering vectors although a damping coefficient of 0.01 is applied to the cylindrical wave fields generated by the point sources. The dynamic range of the MUSIC powers are fixed to be 10 dB so that the lowest MUSIC power is forced to be 10 dB lower than the maximum MUSIC power for all of the result plots in Fig. 26.

In order to investigate the effects of the linear array size, the MUSIC power results obtain by using two linear arrays with the two different sampling spaces of 1 cm and 0.1 cm are presented in Figs. 26(a) and 26(b) (i.e., the measurement aperture sizes are 19 cm and 1.9cm, respectively). As shown Figs. 26(a) and 26(b), the array size affects the maximum MUSIC location and the spatial resolution of the MUSIC power maps. Through the comparison between Figs. 26(a) and 26(b), it can be concluded that the

larger array results in the more accurate source location as well as the higher spatial resolution.

For the case of Fig 26(c), the steering vectors are generated with the structural damping of 0.01 in Eq. (3.10) while the other simulation parameters are same as the case of Fig. 26 (a). By comparing the MUSIC results in Figs. 26 (a) and 26 (c), the spatial resolution gets improved when the structural damping is considered in the steering vectors.

In the cases of the linear arrays, there are mirrored virtual MUSIC power maxima, e.g., around (0.21, 0.14) in Figs. 26 (a) to 26 (c) since the linear arrays cannot be used to distinguish the cylindrical waves generated from both the original and mirrored source locations. Thus, it is difficult to identify the source location accurately with a linear array. Therefore, 2-D arrays such as the cross-shaped and circular arrays are investigated below.

For the cases of Figs. 26 (d) to 26 (f), the source is placed at (0.21, 0.42) m on the left line extended through the linear array. In this source placement, the mirrored local MUSIC power maximum disappears in Fig 26 (d). However, due to the effects of the structural damping, the linear array cannot be used to find the source location precisely in Fig. 26 (d). However, the cross-shaped array and the circular array can be used to identify the source location precisely even without the structural damping in the steering vectors as shown in Figs. 26 (e) and 26 (f), respectively. When comparing Figs. 26 (e) and 26 (f), the spatial resolution of the cross-shaped array is higher than that of the circular array since the measurement aperture size of the cross-shaped array is larger

than the circular array: i.e., the x-direction aperture size of the cross-shaped array is 12 cm, while that of the circular array is 6.4 cm.

For the cases of Figs. 26 (g) to 26 (i), the structural damping coefficient of 0.01 is included in the steering vectors. It is shown that all of the arrays can be used to successfully identify the source location with the high spatial resolution except that the mirrored local MUSIC power maximum of the linear array at (0.21, 0.14) m. The performance of the cross-shaped array is slightly better than that of the circular array when the zoomed MUSIC power results in the upper right corners of Figs. 26 (h) and 26 (i) are compared. Therefore, it can be concluded that for a given number of sensors, the proposed cross-shaped array has the best performance amongst the linear, circular, and cross-shaped arrays, since the cross-shaped array can have larger measurement aperture than the circular array without mirrored virtual maxima. In this paper, the cross-shaped array is thus chosen for the experiment.

3.4 Experimental Setup

A cross-shaped array of 21 PWASs (APC-851 manufactured by American Piezo Ceramics Inc.) is attached on the 2.03 mm thick aluminum panel using superglue (see Figs. 25, 27, 28). The size of the PWAS is 7×7 mm and the sampling space between two adjacent PWASs is 10 mm. In order to have a bigger array aperture, the outer four PWASs are placed 20 mm apart from the closest PWASs. Then, coins or washers are glued on the aluminum panel to simulate structural defects. The dimensions and weights of the simulated defects are shown in Table 11.

	Diameter [mm]	Thickness [mm]	Weight [g]
Quarter coin	24.26	1.75	5.67
Dime coin	17.91	1.35	2.268
Washer	11.11 (Outer Diameter) 4.76 (Inner Diameter)	1.19	0.775

Table 11: Dimensions and weights of simulated defects.

For the purpose of investigating the size and mass effect of the simulated defects in a simple way, instead of machining a real defect, coins and a washer which have a standard size and mass are attached on the panel. This scheme, which is bonding a mass, is also used in ref. 27 and 28, resulting in wave scattering by changing the flexural stiffness and the inertia. In addition, at low frequencies, adding a mass can represent the flexural wave scattering caused by a delamination by means of lowering a flexural stiffness [27]. Figures 27 and 28 show experimental setups to conduct the experiments listed in Table 12.

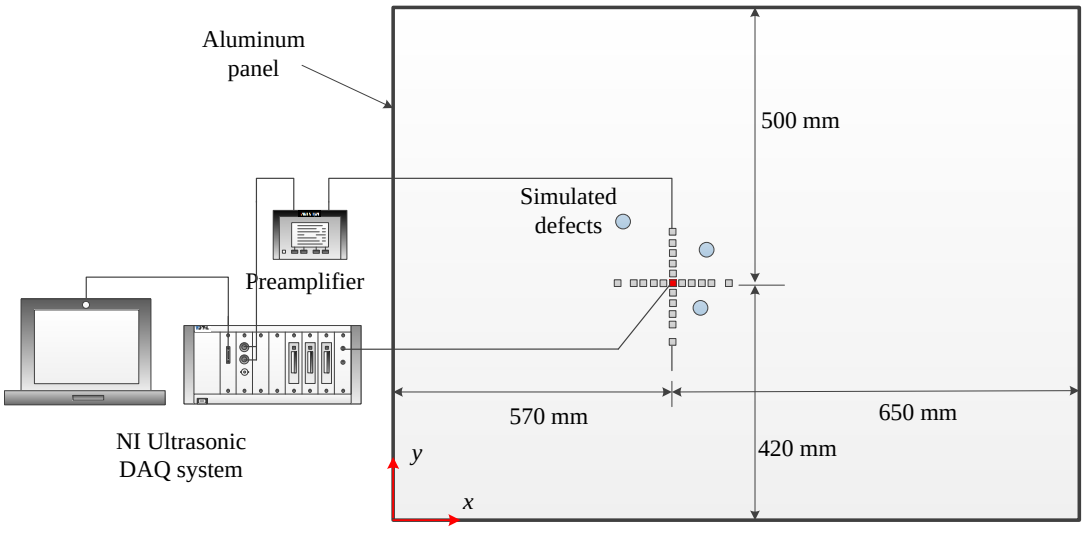

Figure 27: Sketch of experimental setup.

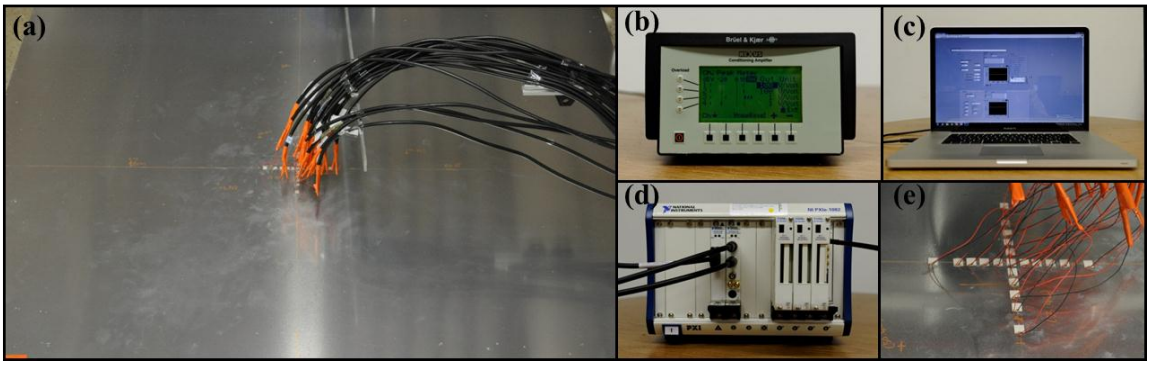

Figure 28: Photos of experimental setup: **(a)** Aluminum panel with PWAS array, **(b)** Brüel & Kjæ r signal conditioning amplifier, **(c)** Laptop with in-house LabVIEW data acquisition program, **(d)** National Instruments ultrasonic data acquisition system, and **(e)** Cross-shaped array (zoomed).

In Table 12, each Experimental Configuration represents a single experiment: e.g., three coins are installed for Experimental Configuration I and a single coin, for Experimental Configuration II. A National Instruments (NI) system equipped with a PXIe-5122 ultrasonic data acquisition (DAQ) module, a PXI-5421 signal generator, and an in-house LabView code is used to generate a burst sinusoidal wave and measure ultrasonic data. Figure 29 shows the burst sinusoidal signal with the center frequency of 20 kHz to excite the panel at the center PWAS. The excitation frequency is determined by using the criterion described in Section 3.6 to generate a single mode Lamb wave. Then, the other PWASs are used to measure the direct and reflective waves. A Brüel & Kjæ r Type 2693 Nexus conditioning amplifier is used to amplify the measured ultrasonic wave signals before the signals are fed to the NI DAQ system. The measured ultrasonic wave signals are recorded for 0.1 seconds at the sampling frequency of 10 MHz.

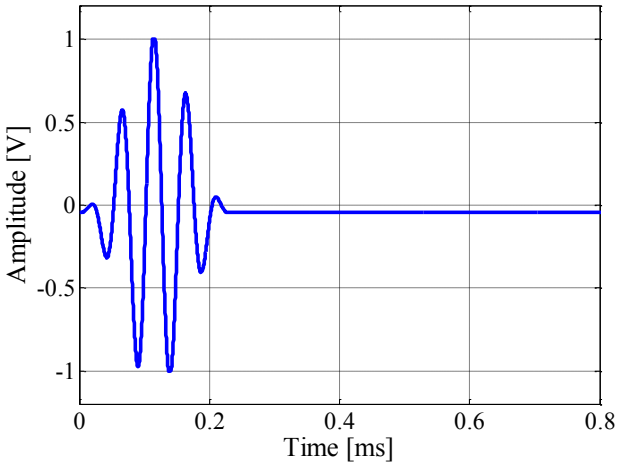

Figure 29: Burst sinusoidal signal with center frequency of 20 kHz for exciting aluminum panel.

Configuration number	Defect number	Coin location, (x, y) [m]	Type of simulated defect	Distance from array center [m]
I	1	(0.63, 0.34)	Quarter coins	0.1
	2	(0.69, 0.58)		0.2
	3	(0.39, 0.66)		0.3
II	4	(0.63, 0.34)	Quarter coin	0.1
III	5		Dime coin	
IV	6		Washer	
V	7	(0.64, 0.34)	Quarter coins	0.106
	8	(0.5, 0.5)		0.106
	9	(0.49, 0.35)		0.106
VI	10	(0.84, 0.06)	Quarter coin	0.45

Table 12: Experimental configurations based on geometric information of simulated defects (i.e., coins and washer) with respect to PWAS array center.

3.5 Time-Frequency Analysis Procedure

A time data block of 20 × 1024 data points is chosen from the measured ultrasonic data at each time step for calculating an instantaneous 20 × 20 cross-spectral matrix in Eq. (3.2): i.e., M = 20 and N = 1024. For a smoothing time transition, 95% of each time data block (i.e., 973 time data points) is overlapped to the next time step. In order to obtain MUSIC power maps, the SVD procedure is additionally applied to the calculated cross-spectral matrix (see Eq. (3.3)). At each time step, an instantaneous MUSIC power map in a scanning area is calculated at the excitation center frequency. Then, the entire procedure is repeated at the next time step. Therefore, the resulting MUSIC beamforming power is presented as the function of time and scanning location.

3.6 Determination of Excitation Frequency

Figure 24 shows the analytical and experimental amplitudes of the symmetric (S0) and anti-symmetric (A0) Lamb wave modes as a function of frequency. The analytical results are discussed in Appendix A. In order to obtain the experimental results in Fig. 24, a PWAS is used to excite the aluminum panel with a burst sinusoidal signal at a center frequency from 20 kHz to 440 kHz. The frequency step (i.e., frequency resolution) is set to 20 kHz. The resulting waves are then measured using the two PWASs placed 17.1 cm and 22 cm apart from the excitation point. Here, the two S0 and A0 Lamb modes are differentiated by their arrival times to the two PWASs since these two modes have different wave speeds. The measured amplitudes are then linearly averaged by repeating the same measurement ten times. In Fig. 24, the measured

amplitudes of the two Lamb wave modes are overlaid with the analytical ones as a function of the excitation frequency. At high frequencies above approximately 300 kHz, the experimental S0 and A0 results have large differences from the analytical results. The analytical strain equations in Eqs. (A.8) and (A.9) are derived under the ideal bonding condition that the bonding layer thickness is zero and the shear stress only exists at the ends of a PWAS. However, in the real experimental case, the bonding layer thickness is not zero and may be also non-uniform. Although the shear stress distribution in Eq. (A.1) can be applied at low frequencies where the wavelength of Lamb waves is much larger than the bonding layer thickness, it cannot be assumed at high frequencies where the bonding layer thickness cannot be ignored when compared to the wavelength. Although no conclusion can be drawn at high frequencies due to the discrepancy between the analytical and experimental results, it can be concluded that the A0 mode is dominant at low frequencies approximately from 20 kHz to 80 kHz.

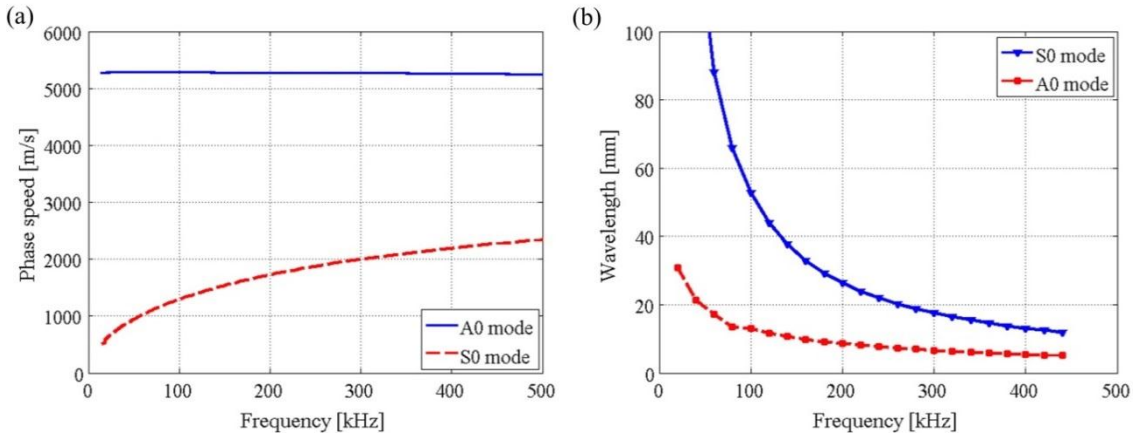

Figure 30: Analytical properties of S0 and A0 Lamb wave modes: **(a)** Phase speeds and **(b)** Wave lengths.

In addition that an excitation frequency is selected where a single Lamb wave mode is dominant, the selected frequency should satisfy the Nyquist Sampling Theorem to avoid any spatial aliasing problems. This Nyquist requirement is represented as

$$d < \frac{\lambda}{2} = \frac{c_p}{2f}, \tag{3.11}$$

where c_p is the phase speed of a Lamb wave. Figure 30(a) is the analytical phase speeds of the S0 and A0 Lamb wave modes for the 2.03 mm aluminum panel that are obtained from the dispersion equations in Eqs. (C.24) and (C.25). Then, the wavelengths of the two wave modes can be calculated as shown in Fig. 30(b). Since the PWAS size is 7 mm × 7 mm and the minimal sampling space between adjacent two PWASs is approximately 10 mm, the wavelength should be larger than 20 mm to avoid the spatial aliasing as shown in Eq. (3.11). The wavelength of the A0 mode is larger than 20 mm below 40 kHz where the A0 mode is dominant. Since the amplitude of the S0 mode can be ignored at 20 kHz when compared to that of the A0 mode, 20 kHz is chosen as the excitation frequency where the wave speed and wavelength are 615 m/s and 30.75 mm, respectively. For a case of detecting a small-sized defect, a PWAS array with a smaller sampling space between adjacent two PWASs can be used with higher ultrasonic frequency waves.

3.7 Time-frequency Analysis Results

Experimental Configurations are described in Table 12. In Experimental Configuration I, three quarter coins with three different distances (i.e. 10 cm, 20 cm, and

30 cm) from the array center are glued on the aluminum panel to simulate three structural defects. The normalized, cylindrical, 2-D steering vector obtained from Eqs.(3.7) and (3.9) is used as a default steering vector since the aluminum panel can be regarded as a 2-D surface. Figure 31(a) shows the beamforming result calculated by applying the conventional, frequency-domain MUSIC algorithm to the entire time records (i.e., 0.1 second data) for Experimental Configuration I. As shown in Fig. 31(a), the conventional MUSIC algorithm cannot be used to identify the simulated defect locations (represented by the circles) due to multiple wave reflections, in particular, from the panel edges (i.e., boundaries) as well as the direct excitation wave.

The performance of the conventional MUSIC algorithm can be improved by removing the partial time data of the direct excitation wave and the boundary-reflected waves from the entire time data. The performance of the time-frequency MUSIC algorithm is then compared to that of this time-gating beamforming approach. By applying the time-frequency MUSIC algorithm to the measured array signals, the maximum beamforming power on the scanning area (i.e., the panel surface) can be identified from the calculated beamforming map at each time. The resulting maximum MUSIC power is shown in Fig. 31(b) as a function of time for Experimental Configuration I in Table 12. In this plot, the marked peaks (at t = 0.145 ms, 0.2521 ms, and so on) indicate the arrival of the direct-excitation or reflective waves to the array. The first peak at t = 0.145 ms represents the direct excitation wave, the next three peaks at t = 0.2521 ms, 0.4102 ms, and 0.5683 ms are induced by the reflected waves from the

three simulated defects, and the fifth peak at t = 0.7468 ms is from the bottom boundary that is the nearest boundary location from the array.

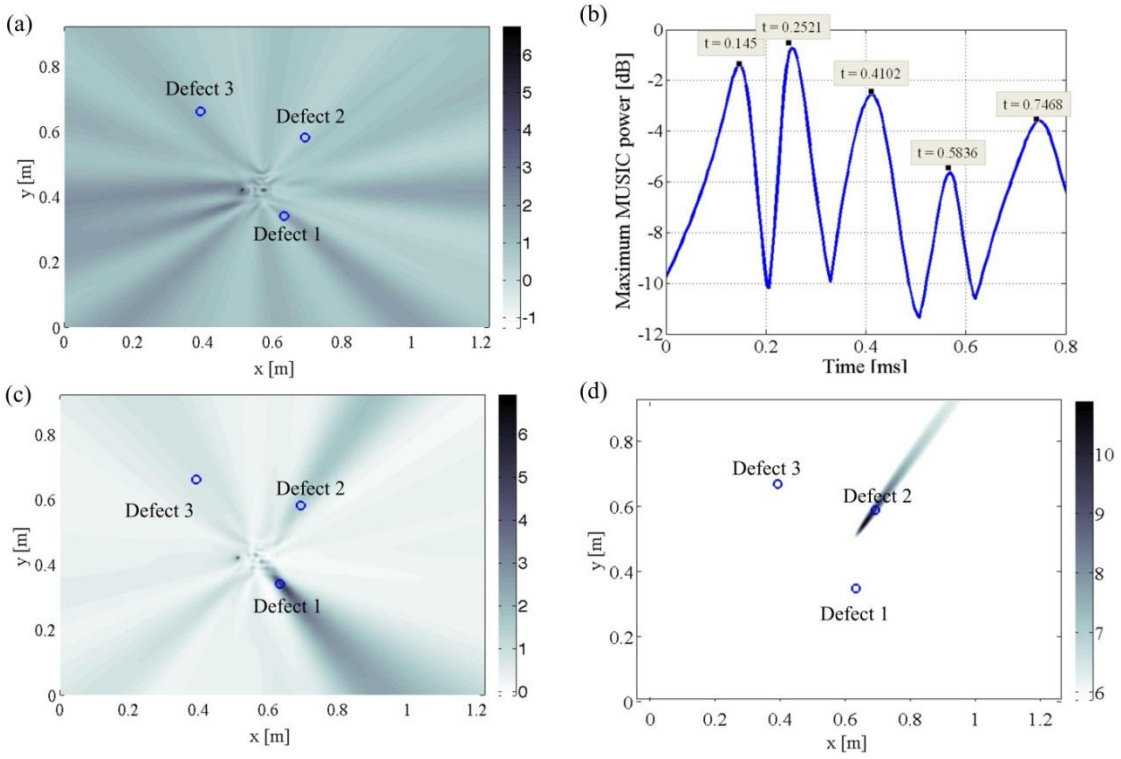

Figure 31: MUSIC power results in dB scale for Experimental Configuration I (refer to Table 12 for the defect numbers): **(a)** Conventional frequency-domain MUSIC algorithm applied to entire time data (i.e., 0.1 second data), **(b)** Maximum instantaneous MUSIC power, **(c)** Conventional MUSIC algorithm applied to time data gated from t = 0.2 ms to 0.62 ms, and **(d)** Time-frequency MUSIC algorithm at t = 0.4102 ms.

In order to compare the performance of the time-gating and time-frequency MUSIC algorithms, the measured time data is truncated before t = 0.2 ms and after 0.62 ms so that only the defect-reflected wave signals can be used for the conventional MUSIC beamforming processing. As shown in Fig. 31(c), the conventional MUSIC result

obtained from the time-gated array signals can be used to identify the nearest coin location although the other two coins are hardly identified from this result due to its poor spatial resolution around these two coins. On the other hand, the time-frequency MUSIC result, for example, at t = 0.4102 ms in Fig. 31(d) has much higher spatial resolution than the result in Fig. 31(c) to accurately detect the second coin. Since the time-frequency MUSIC beamforming analysis at each time step is conducted with a short length of the time data, the resulting MUSIC result can be focused on a specific defect-induced reflection event that generally occurs in a short time period. Therefore, it is possible to obtain the MUSIC power maps with much higher spatial resolution by using the time-frequency MUSIC algorithm than the conventional beamforming algorithm applied to the time-gated array signals.

The time-frequency beamforming results in Figs. 32 – 37 are calculated by applying the time-frequency MUSIC algorithms to the measured array data. They are represented as the function of time and space. The time-frequency MUSIC powers at the last four peak locations in Fig. 31(b) are plotted in Fig. 32 as a function of scanning location. In Figs. 32(a) – 32(c), the three coin locations can be identified at the maximum MUSIC power locations. The minimum distance differences (i.e., errors) between the locations of the coins and the MUSIC power maxima range from 0 cm to 5.1 cm (see Fig. 39(a) for Defects 1 – 3). The bottom boundary location can be also identified from the MUSIC power plot in Fig. 32(d) at t = 0.7468 ms.

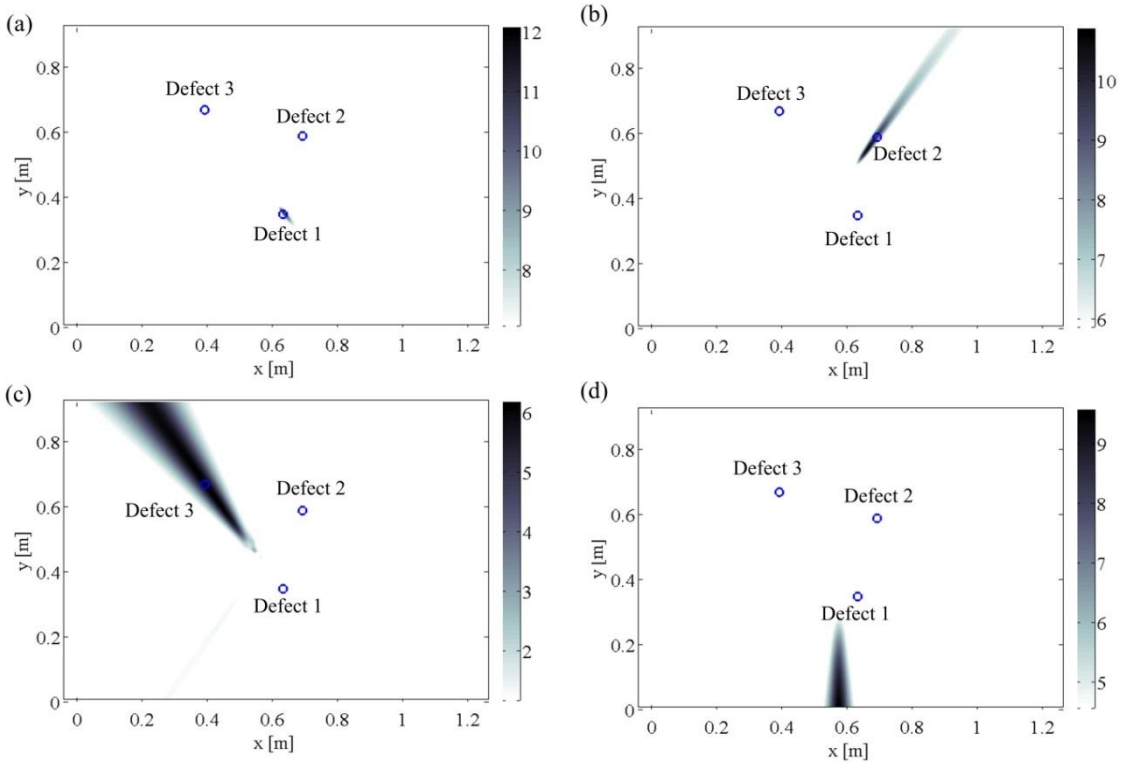

Figure 32: Time-frequency MUSIC power results in dB scale for Experiment Configuration I (refer to Table 12 for the defect numbers): **(a)** Time = 0.2521 ms, **(b)** Time = 0.4102 ms, **(c)** Time = 0.5836 ms, and **(d)** Time = 0.7468 ms.

The time-frequency MUSIC power results for Experimental Configuration I are summarized in Figs. 33(a) and 33(b) in terms of the maximum beamforming power locations, coin locations, and -0.5 dB contour lines (i.e., 0.5 dB lower than a local maximum MUISIC power level). For example, Fig. 33(a) is obtained by combining Figs 32(a) – 32(c). Figure 33(a) show the MUSIC power result from the second to fourth peak times (in Fig. 31(b)) to identify the three coin locations, while Fig. 35(b) shows the MUSIC power result that can be used to identify all of the four boundary reflections. By comparing the contoured areas at t = 0.2521 ms, 0.4102 ms, and 0.5836 ms in Fig. 33(a),

it is shown that the spatial resolution of the proposed algorithms is getting low as the defect distance increases.

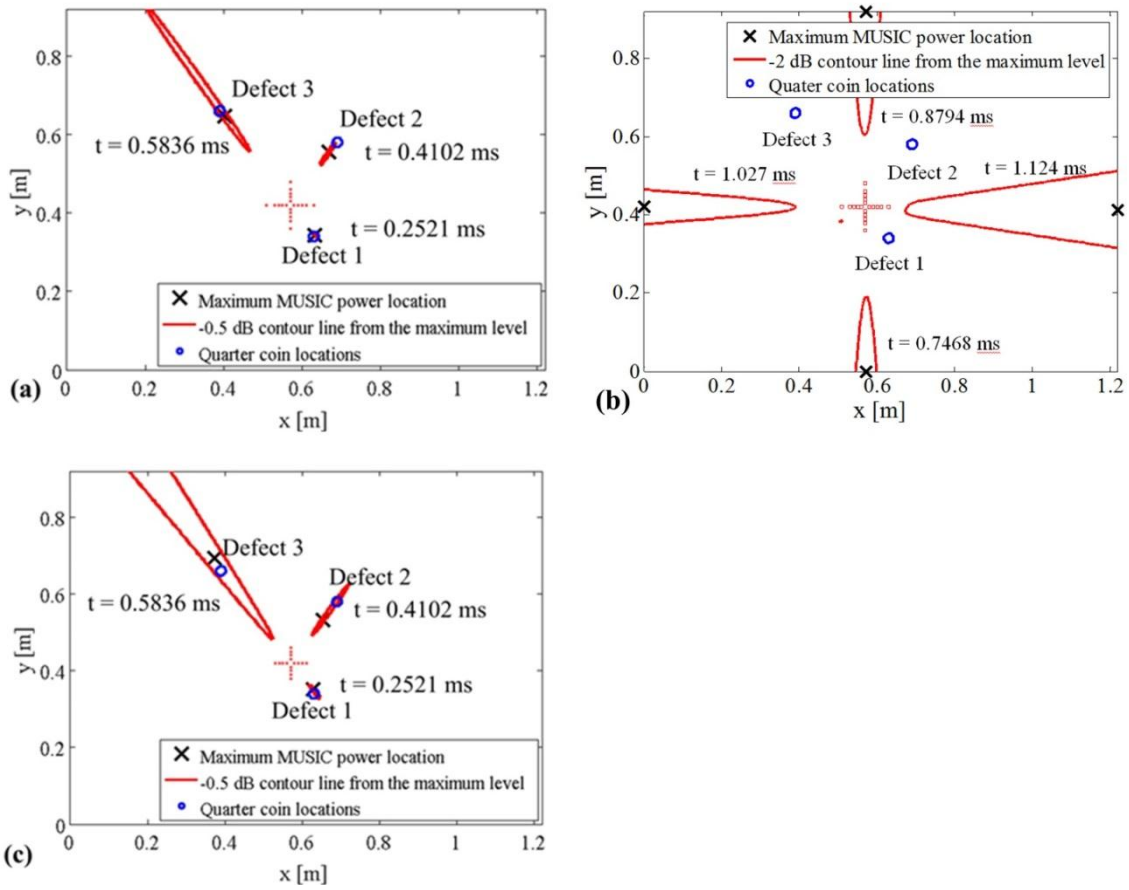

Figure 33: Time-frequency MUSIC power results for Experiment Configuration I of Table 12: **(a)** MUSIC power at t = 0.2521 ms, 0.4102 ms, and 0.5836 ms, **(b)** MUSIC power at t = 0.7468 ms, 0.8794 ms, 1.027 ms, and 1.124 ms, and **(c)** MUSIC power, at t = 0.2521 ms, 0.4102 ms, and 0.5836 ms, obtained by removing outer 4 transducer data.

In order to check the effects of the outer four sensors in the cross-shaped array, the data measured with outer 4 transducers is removed from the total array data and the MUSIC power result of this reduced data is shown in Fig. 33(c). By comparing Fig.

33(c) to Fig. 33(a) where the total array data is applied, it can be found that the full cross-shaped array improve the spatial resolution of the MUSIC power result by increasing the measurement aperture size.

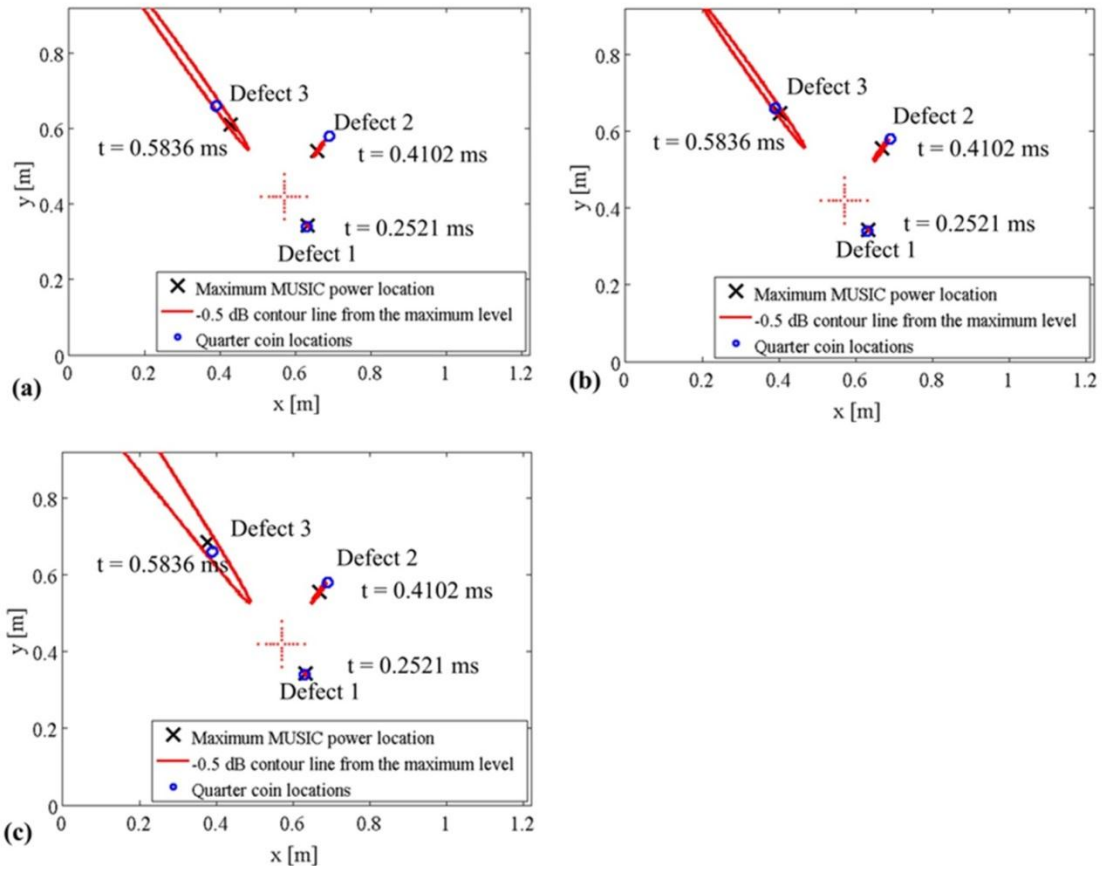

Figure 34: Time-frequency MUSIC power results for Experiment Configuration I in Table 13 with undamped 1-D, 2-D, and 3-D steering vectors at t = 0.2521 ms, 0.4102 ms, and 0.5836 ms: **(a)** 1-D steering vector in Eq. (4.8), **(b)** Normalized 2-D steering vector in Eqs. (4.7) and (4.9), and **(c)** Normalized 3-D steering vector in Eqs. (4.6) and (4.9).

Figure 34 shows the MUSIC power results obtained by applying the planar, 1-D steering vector in Eq. (3.8), the normalized, cylindrical, 2-D steering vector in Eqs. (3.7)

and (3.9), and the normalized, spherical, 3-D steering vector in Eqs. (3.6) and (3.9). Here, the structural damping is not considered in all of the steering vectors. One of interesting findings from this figure is that the 1-D steering vector can be used to identify the defect location in the nearfield of the array although this 1-D steering vector has the only phase information in the exponential function without a geometrical decaying factor such as the $1/r^{0.5}$ or $1/r$ term (see Eq. (3.8)). From Fig. 34, it is shown that the time-frequency MUSIC result with the 2-D steering vector has the highest spatial resolution since it has the smallest area surrounded by the -0.5 dB contour lines at t = 0.5836 ms. It is also shown the farther a defect locates from the array center, the more accurate wave propagation model (i.e., the cylindrical wave propagation model) for the steering vector is required to identify the defect location accurately.

Figure 35 shows the effects of the spatial decay induced by the structural damping (see Eq. (3.10)) in the cylindrical, 2-D steering vectors. The highest spatial resolution of the time-frequency MUSIC results can be achieved at the structural damping coefficient of 0.03 as shown in Fig. 35 (in particular, see the -0.5 dB contour lines around Defect 3).

Experimental Configurations II, III, and IV in Table 12 are designed to investigate the effect of the different defect sizes and weights in Table 11. The MUSIC power maximum locations in Figs. 36(a) and 36(b) are exactly coincident with the locations of the quarter coin for Experimental Configuration II (see Fig. 36(a)) and the dime coin for Experimental Configuration III (see Fig. 36(b)).

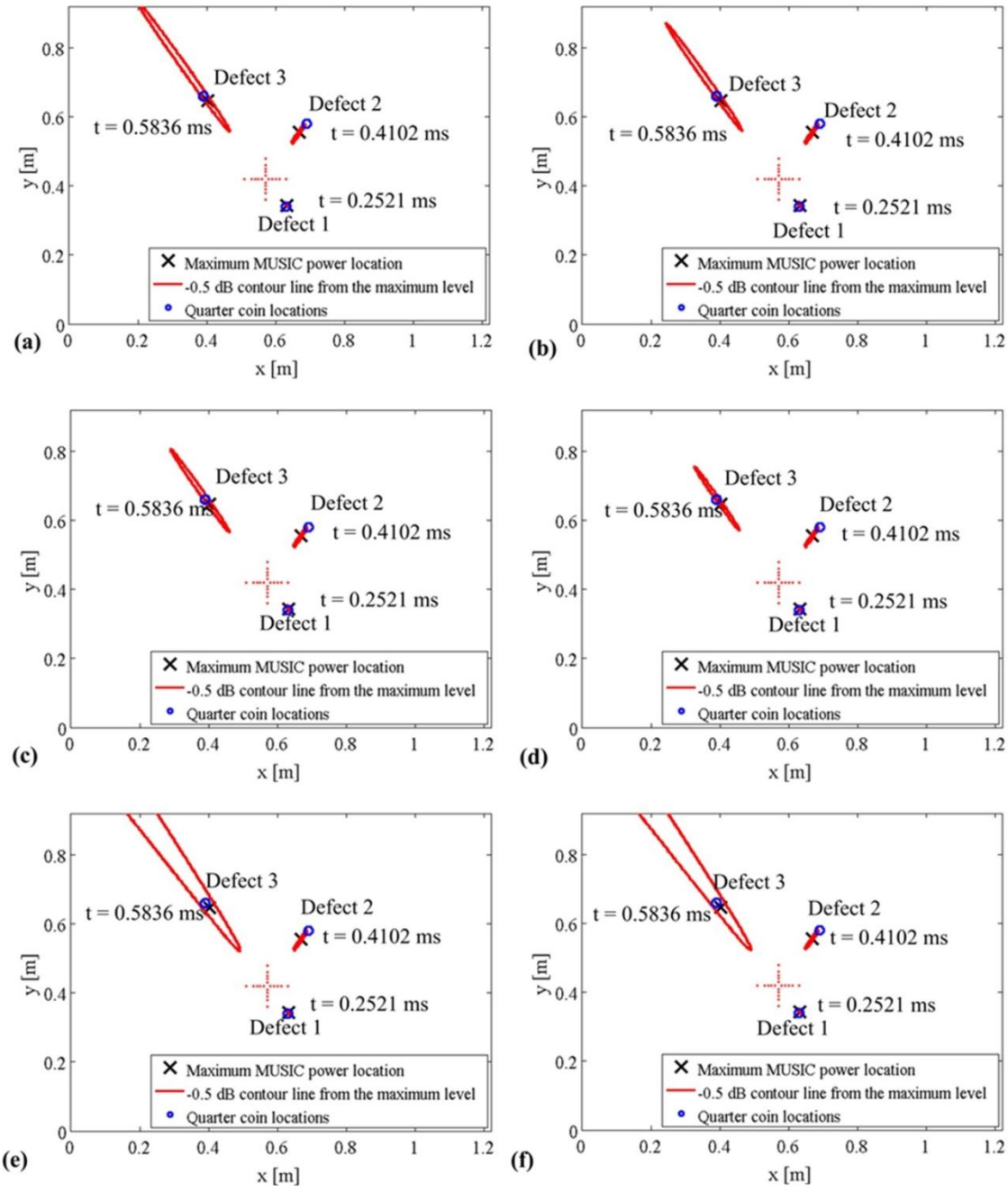

Figure 35: Time-frequency MUSIC power results for Experiment Configuration I of Table 12 with cylindrical 2-D steering vectors including structural damping: **(a)** $\eta = 0$, **(b)** $\eta = 0.01$, **(c)** $\eta = 0.02$, **(d)** $\eta = 0.03$, **(e)** $\eta = 0.04$, and **(f)** $\eta = 0.05$.

For the washer in Experimental Configuration IV, the washer location (i.e., the location of Defect 6) predicted by using the time-frequency MUSIC algorithm is a little off from the actual location due to the washer's small size and weight (see the case of Defect 6 in Figs. 39(a)–39(b)) although the washer's direction with respect to the array center is accurately identified by the proposed MUSIC algorithm (see the Defect 6 case in Fig. 39(c)).

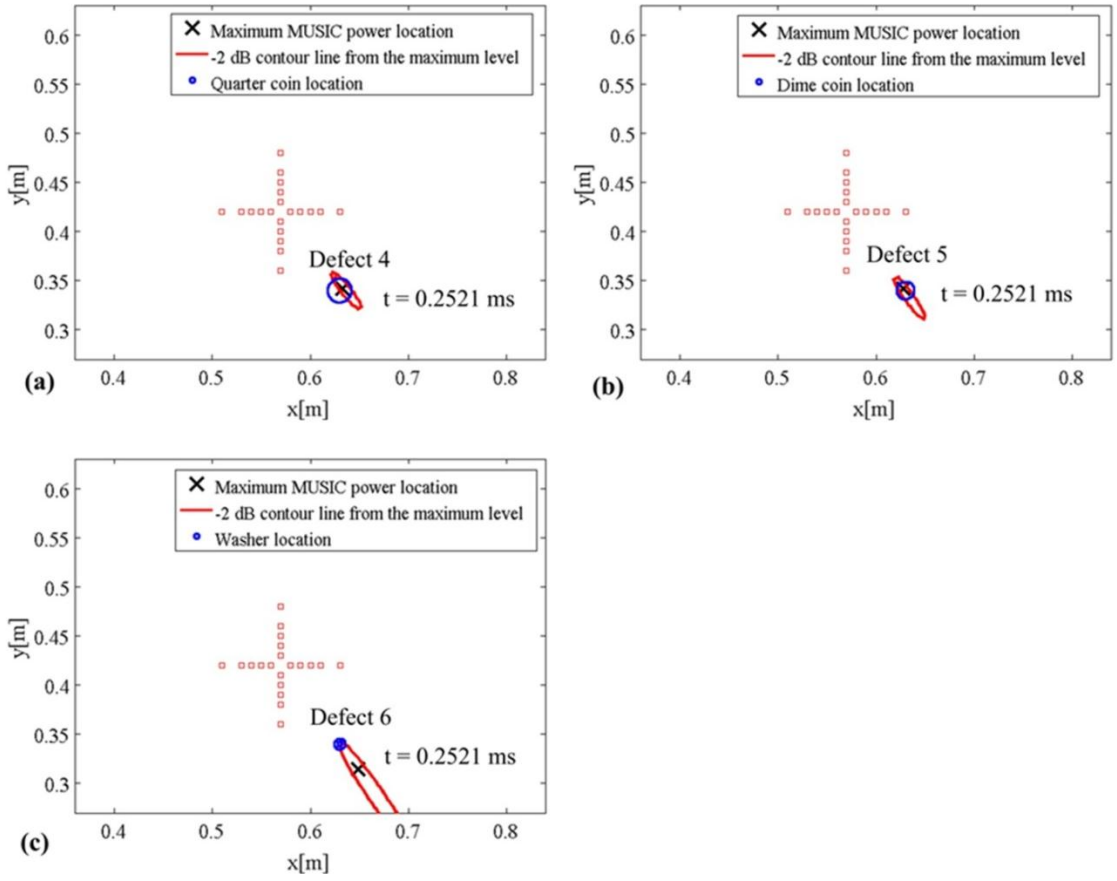

Figure 36: Time-frequency beamforming powers in dB scale for Experiment Configurations II, III, and IV at t = 0.2521 ms for different defects (refer to Table 12 for the defect numbers): **(a)** Quarter coin, **(b)** Dime coin, and **(c)** Washer.

In order to validate the performance of the proposed methods with the simulated defects located at a same distance from the array center, the three quarter coins are placed at a 10.6 cm distance from the array center in Experimental Configuration V (see Table 12). As shown in Fig. 37, the MUSIC power map at t = 0.2521 ms can be used to identify all of the three coin locations. The maximum distance differences between the actual coin locations and the local maximum MUSIC power locations are 0 cm, 0.9 cm, and 0.5 cm as shown in the Defects 7 – 9 cases of Figs. 39(a) –39(b).

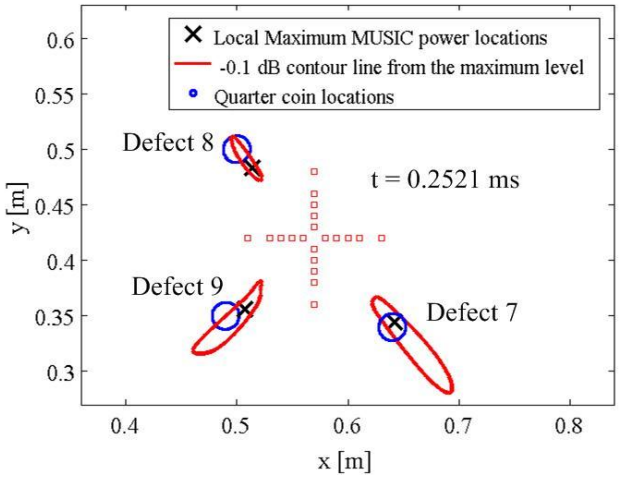

Figure 37: Time-frequency beamforming powers in dB scale at t = 0.2521 ms for Experiment Configuration V (refer to Table 12 for the defect numbers).

The proposed time-frequency MUSIC can be used to detect a structural defect that is farther away from the array than one of the boundary edges. As shown in Experimental Configuration VI in Table 12, a quarter coin is attached on the aluminum plate at a distance of 45 cm from the array center (i.e., x = 0.84 m and y = 0.06 m). This coin location is farther than the bottom boundary at a distance of 40 cm and closer than the

upper boundary at a 50 cm distance. Figure 38(a) shows the conventional MUSIC power map obtained from the time data gated from t = 0.2 ms to t = 0.92 ms to exclude the direct excitation wave and the left- and right-boundary-reflected waves. The time-frequency beamforming result associated with the second eigenvector at t = 0.7937 ms is also presented in Fig. 38(b). Due the strong reflected waves from the edges, the conventional MUSIC result cannot be used to identify the simulated defect even after gating the time data as shown in Fig. 38(a). However, the time-frequency beamforming MUSIC power map shows a local maximum power around the defect. Hence, it can be concluded that the time-frequency MUSIC algorithm can be used to identify the structural defect located beyond the shortest boundary distance from the array.

As the summary of the above results, the distance and angle differences (i.e., errors) between the simulated defects and the local MUSIC power maxima are presented in Fig. 41. Here, the distance difference is defined as the smallest length between a point within a coin or washer and the corresponding local maximum MUSIC power location. Similarly, the angle difference is defined as the minimum absolute value of the angle difference between an angle of a point within a coin or washer and the angle of the corresponding local maximum MUSIC power location with respect to the array center.

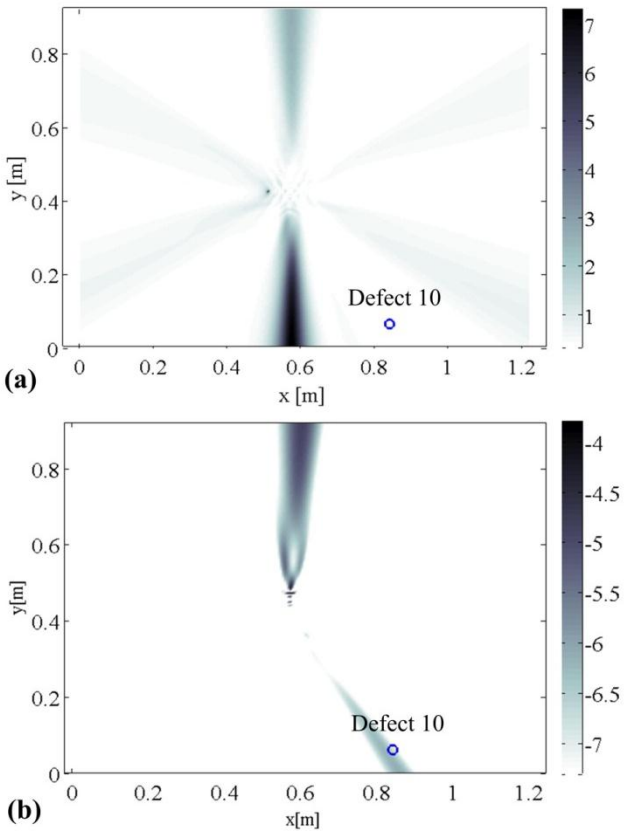

Figure 38: MUSIC power results in dB scale for Experimental Configuration VI in Table 12: **(a)** Conventional MUSIC algorithm applied to time data gated from t = 0.2 ms to 0.92 ms and **(b)** Time-frequency MUSIC algorithm at t = 0.7937 ms.

Figure 39(a) shows the distance errors for the cases of the undamped steering vector (i.e., $\eta = 0$). As shown in Fig. 39(a), the distance error increases as the distance between a simulated defect and the array center increases (e.g., see the cases of Defects 1 – 3) when the 1-D plane-wave-type steering vector in Eq. (3.8) is applied. Since the 1-D steering vectors cannot accurately represent the real ultrasonic wave propagation in the aluminum plate, the distance error becomes large as the distance increases. When the 2-D steering vector is applied, the distance error decreases, in particular, for the farfield defect cases (e.g., the cases of Defects 2 and 3 in Fig. 38(a)). When the defects locate

close to the array, the distance errors are insensitive to the wave propagation models of the steering vectors.

Figure 39(b) shows the distance differences when the structural damping of $\eta = 0.03$ is applied to the steering vectors. By comparing Figs. 39(a) and 39(b), it can be found that there is no error reduction resulted in from the inclusion of the structural damping in the 2-D and 3-D steering vectors. In the 2-D and 3-D steering vectors, the structural-damping-induced spatial decay may be much less significant than the geometry-induced spatial decay (i.e., $1/r$ and $1/r^{0.5}$). However, for the case of the 1-D steering vector in which the only phase information is considered without the geometry-induced spatial decay, the distance errors are reduced by including the structural-damping-induced spatial decay in the steering vector (e.g., see the cases of Defects 2 and 3 in Figs. 39(a) and 39(b)). This distance error increases as the size and weight of a simulated defect decrease (see the Defects 4 – 6 cases in Figs. 39(a) and 39(b)). However, for all of the simulated defects investigated in this article, the angle errors are zero (see Fig. 39(c)), which indicates that the proposed time-frequency beamforming procedures can be used to accurately identify the directions of structural defects.

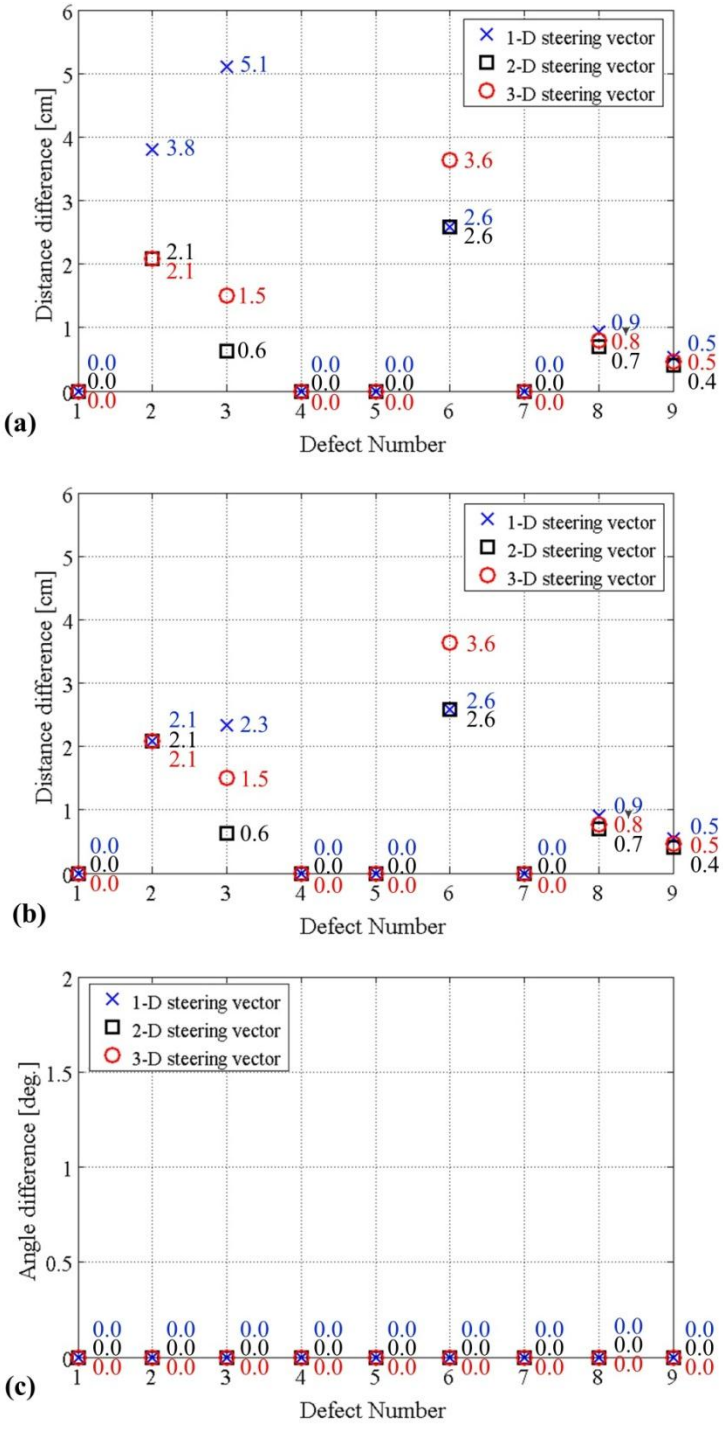

Figure 39: Distance and angle differences (i.e., errors) between simulated defects and MUSIC power maxima (refer to Table 12 for the "Defect Number"): **(a)** Distance errors when $\eta = 0$, **(b)** Distance errors when $\eta = 0.03$, and **(c)** Angle errors ($\eta = 0$ and $\eta = 0.03$).

4. CONCLUSION

In order to conduct NDEs of plates and pipes, the wave propagation characteristics of these shell structures are investigated by developing the HAFEM procedures. The proposed HAFEM approaches can be used to build computationally efficient models by combining a finite element approximation and an analytical wave solution. For the validation of the proposed HAFEM procedures, the analytical solutions of the simple panel and a circular plate are compared to the HAFEM-predicted results. The developed HAFEM procedures can be applied to model multi-layered composite panels and pipes, identifying the wave speeds and cross-sectional mode shapes. The wave speeds and mode shapes predicted by using the HAFEM are well matched with the analytical ones. In particular, the HAFEM-predicted dispersion curves in low frequencies are compared to those obtained from the Bernoulli-Euler theory and the shell theory. Since there is no specific assumption used for the HAFEM procedures, the HAFEM-predicted dispersion results match better with the experimental results than those obtained from the Bernoulli-Euler theory that is only valid with thin beams. They match well with those obtained from the shell theory for the empty pipe case.

In addition, the 2-D HAFEM procedure with the solid elements is extended by developing fluid elements and solid-fluid boundary conditions, resulting in the dispersion curves of fluid-filled pipes. In ultrasonic frequencies, the latter HAFEM procedure is validated by comparing the HAFEM-predict dispersion curves to the "experimental" ones for an empty pipe and the "analytical" ones for a fluid-filled pipe.

Although the HAFEM procedures are useful to understand the wave propagation characteristics of fluid-filled, multi-layered composite pipes with arbitrary cross-sections, the cross-sectional shapes should not change in the axial direction. In order to consider a pipe system assembled with multiple pipe sections with different cross-sections, the acoustic transfer function approach is derived from the HAFEM formation. By comparing the measured and predicated results, it is shown that the proposed acoustic transfer matrix approach can be used to accurately estimate all of the longitudinal, torsional, and flexural wave modes in the multi-sectional pipe system. The estimated FRFs by using both the HAFEM model with 160 nodes and the ANSYS model with 15443 nodes agree well with the experimental FRF results.

In order to non-destructively locate structural defects in plates by using a single-mode ultrasonic Lamb wave, the time-frequency MUSIC beamforming procedure that can be used to distinguish the effects of the direct excitation and boundary-reflected waves are proposed in this research. In the proposed procedure, a burst sinusoidal signal is used to excite a plate with a single-mode Lamb wave. Then, the resulting ultrasonic wave signals are measured using a sensor array. Then, the proposed time-frequency MUSIC beamforming algorithm is applied to the measured array data to obtain the beamforming maps, as the functions of time and scanning location, whose local maxima at specific time instants (between the arrival times of the direct excitation wave and the boundary-reflected waves) can be identified as structural defect locations.

In this research, by properly choosing the excitation center frequency of the burst sinusoidal excitation signal, it is shown analytically and experimentally that the single

anti-symmetric A0 Lamb mode can be exclusively excited in the 2.03 mm aluminum plate.

Due to the strong reflective waves generated from the boundaries of the aluminum panel, the conventional, steady-state MUSIC beamforming algorithm cannot be used to identify the simulated defect locations. When the proposed time-frequency MUSIC beamforming algorithms are applied to process the measured array data, the simulated defect locations can be identified from the spatial beamforming power maps at the specific times, while the effects of the direct excitation and boundary-reflected waves appear at the different times. In order to improve the spatial resolution of the time-frequency MUSIC algorithm, the structural-damping-induced spatial decay model is proposed to be considered in the steering vectors. In addition, a cross-shaped array is selected to further improve the spatial resolution and to avoid mirrored virtual image effects. When the normalized, cylindrical 2-D steering vectors are applied, the distance error can be minimized since they represent the real wave propagation in the aluminum panel. For the case of the multiple defects at the same distance (i.e. 10.6 cm), the proposed methods can be used to identify the multiple locations successfully within a distance error of 0.9 cm. It is also shown that the time-frequency MUSIC algorithm can be used to identify the structural defect located beyond the shortest boundary distance from the array. Finally, the proposed time-frequency MUSIC beamforming procedure does not require undamaged state data as a baseline.

REFERENCES

[1] Z. Su, L. Ye, and Y. Lu, "Guided Lamb waves for identification of damage in composite structures: a review," *Journal of Sound and Vibration* 295, 753-780, (2006).

[2] J.L. Rose, "A baseline and vision of ultrasonic guided wave inspection potential," *Journal of Pressure Vessel Technology Transactions of ASME* 124, 273-282, (2002).

[3] J.L. Rose, *Ultrasonic Waves in Solid Media*, Cambridge University Press, (1999).

[4] N.A. Haskell, "The dispersion of surface waves on multilayered media," *The Seismological Society of America,* 17-34, (1953).

[5] D.C. Gazis, "Three-dimensional investigation of the propagation of waves in hollow circular cylinders. I. analytical foundation," *Journal of the Acoustical Society of America* 31, 568-572, (1959).

[6] C.R. Fuller and F.J. Fahy, "Characteristics of wave propagation and energy distributions in cylindrical elastic shells filled with fluid", *Journal of Sound and Vibration* 81, 501-518, (1982).

[7] R. Long, P. Cawley, and M. Lowe, "Acoustic wave propagation in buried iron water pipes", *Proceedings of the Royal Society A* 459, 2749-2770, (2003).

[8] S. Dong and R. Nelson, "On natural vibrations and waves in laminated orthotropic plates," *Journal of Applied Mechanics* 39, 739-745, (1972).

[9] R. Nelson and S. Dong, "High frequency vibrations and waves in laminated orthotropic plates," *Journal of Vibration and Acoustics* 30 (1), 33-44, (1973).

[10] P. Shorter, "Wave propagation and damping in linear viscoelastic laminates," *Journal of the Acoustical Society of America* 115 (5), 1917-1925, (2004).

[11] Y.-J. Kim and J.H. Han, "Identification of acoustic characteristics of honeycomb sandwich composite panels using hybrid analytical/finite element method," *Journal of Vibration and Acoustics Transactions of ASME* 135, 011006 (11 pages), (2013).

[12] Y. K. Cheung, *Finite Strip Method in Structural Analysis*, Pergamon Press, (1976).

[13] H. Taweel, S.B. Dong, and M. Kazic, "Wave reflection from the free end of a cylinder with an arbitrary cross-section", *International Journal of Solids and Structures* 37, 1701-1726, (2000).

[14] Y.-J. Kim and J. S. Bolton, "Analysis of tire vibration by using a hybrid two-dimensional finite element based on composite shell theory," *Proceedings of Inter-Noise 2003*, (2003).

[15] Y-J. Kim and J. S. Bolton, "Effects of rotation on the dynamics of a circular cylindrical shell with application to tire vibration," *Journal of Sound and Vibration* 275, 605-621, (2004).

[16] Y.-J. Kim, "Identification of sound transmission characteristics of honeycomb sandwich panels using hybrid analytical/one-dimensional finite element method," *Proceedings of Inter- Noise 2006*, Honolulu, USA, (2006).

[17] Y.-J. Kim, "Acoustical characteristics of honeycomb sandwich composite panels," *The 160th Meeting of the Acoustical Society of America*, Seattle, WA, (2011).

[18] T. Hayashi, W.-J. Song, and J.L. Rose, "Guided wave dispersion curves for a bar with an arbitrary cross-section, a rod and rail example", *Ultrasonics* 41, 175-183, (2003).

[19] J.H. Han and Y.-J. Kim, "Ultrasonic Lamb wave propagation characteristics in hollow cylindrical pipes," *Proceedings of Inter-Noise 2012*, (2012).

[20] J.H. Han and Y.-J. Kim, "Modeling of wave propagation in drill strings using acoustic transfer matrix methods", *Journal of the Acoustical Society of America*, in print, (2013).

[21] V. Giurgiutiu, "Tuned Lamb wave excitation and detection with piezoelectric wafer active sensors for structural health monitoring," *Journal of Intelligent Material Systems and Structures* 16, 291-305, (2005).

[22] G.B. Santoni, L. Yu, B. Xu, and V. Giurgiutiu, "Lamb wave-mode tuning of piezoelectric wafer active sensors for structural health monitoring," *Journal of Vibration and Acoustics Transactions of ASME* 129, 752-762, (2007).

[23] E.F. Crawley and J. de Luis, "Use of piezoelectric actuators as elements of intelligent structures," *The American Institute of Aeronautics and Astronautics Journal* 25, 1373-1385, (1987).

[24] E.F. Crawley and E.H. Anderson, "Detailed models of piezoceramic actuation of beams," *Journal of Intelligent Material Systems and Structures* 1, 4-25, (1990).

[25] Z. Su, L. Ye, and Y. Lu, "Guided Lamb waves for identification of damage in composite structures: a review," *Journal of Sound and Vibration* 295, 753-780, (2006).

[26] V. Giurgiutiu, "Lamb wave generation with piezoelectric wafer active sensors for structural health monitoring," *Proceedings of the International Society for Optics and Photonics (SPIE)*, 5056, 111-122, (2003).

[27] C.H. Wang, J.T. Rose, and F.K. Chang, "A computerized time-reversal method for structural health monitoring," *Proceedings of the International Society for Optics and Photonics (SPIE)*, 48-58, (2003).

[28] C.H. Wang, J.T. Rose, and F.K. Chang, "A synthetic time-reversal imaging method for structural health monitoring," *Smart Materials and Structures* 13, 415-423, (2004).

[29] R. Ikegami and E.D. Haugse, "Structural health management for aging aircraft," *Proceedings of the International Society for Optics and Photonics (SPIE)*, 4332, 60-67, (2001).

[30] H. Sohn, H.W. Park, K.H. Law, and C.R. Farrar, "Combination of a time reversal process and a consecutive outlier analysis for baseline-free damage diagnosis," *Journal of Intelligent Material Systems and Structures* 18, 335–346, (2007).

[31] V. Giurgiutiu and J. Bao, "Embedded-ultrasonics structural radar for in situ structural health monitoring of thin-wall structures," *Structural Health Monitoring* 3, 121-140, (2004).

[32] F. Yan and J.L. Rose, "Guided wave phased array beam steering in composite plates," *Proceedings of the International Society for Optics and Photonics (SPIE)* 6532–65320G 1-9, (2007).

[33] J.L. Li, H.F. Zhao, and W. Fang, "Experimental investigation of selective localisation by decomposition of the time reversal operator and subspace-based technique," *Institution of Engineering and Technology (IET) Radar, Sonar and Navigation* 2, 426-434, (2008).

[34] F.K. Gruber, E.A. Marengo, and A.J. Devaney, "Time-reversal imaging with multiple signal classification considering multiple scattering between the targets," *Journal of the Acoustical Society of America* 115 (6), 3042-3047, (2004).

[35] D.W. Schindel, D.S. Forsyth, D.A. Hutchins, and A. Fahr, "Air-coupled ultrasonic NDE of bonded aluminum lap joints", *Ultrasonics* 35, 1-6, (1997).

[36] A. Belouchrani and M.G. Amin, "Time-frequency MUSIC," *IEEE Signal Processing Letters* 6 (5), 109-110, (1999).

[37] D.H. Johnson and D.E. Dudgeon, *Array Signal Processing: Concepts and Techniques*, Prentice-Hall, 111-198, (1993).

[38] K.F. Graff, *Wave Motion in Elastic Solids*, Dover Publications, (1991).

[39] W. Soedel, *Vibrations of Shells and Plates*, Marcel Dekker, Inc., (1993).

[40] Kurtze, K., and Watters, B. G., "New wall design for high transmission loss or high damping," *Journal of the Acoustical Society of America* 31(6), pp. 739–748, (1959).

[41] J. N. Reddy, *Introduction to the Finite Element Method*, McGraw Hill, (1993).

[42] I.G. Currie, *Fundamental Mechanics of Fluids*, 3rd edition. Marcel Dekker, Inc, (2003).

[43] F. Fahy, *Sound and Structural Vibration*, Academic Press, (1987).

[44] A.M. Horr and L.C. Schmidt, “Modeling of nonlinear damping characteristics of a viscoelastic structural damper”, *Engineering Structures* 18**,** 154-161, (1996).

[45] ASTM Standard E756-05, Standard test method for measuring vibration-damping properties of materials.

[46] D.J. Inman, *Engineering Vibration*, Prentice Hall, (2001).

[47] G. Cowper, “The shear coefficient in Timoshenko’s beam theory,” *Journal of Applied Mechanics* 335-340, (1966).

[48] H. Sato, M. Lebedev, and J. Akedo, “Theoretical and experimental investigation of propagation of guided waves in cylindrical pipe filled with fluid,” *Japanese Journal of Applied Physics* 45, 4573-4576, (2006).

[49] D.S. Drumheller, “Acoustical properties of drill strings,” *Journal of the Acoustical Society of America* 85**,** 1048-1064 (1989).

[50] V. Giurgiutiu, J. Bao, and W. Zhao, “Active sensor wave propagation health monitoring of beam and plate structures,” *Proceedings of the SPIE’s 8th International Symposium on Smart Structures and Materials, Newport Beach, CA, March 4-8,* (2001).

APPENDIX

A. Analytical Lamb Wave Generation Model

For the ideal bonding case with zero bonding layer thickness, Giurgiutiu derived the strain equation of a rectangular PWAS installed on a plate as a function of excitation frequency [26]. The shear stress at this ideal bonding layer can be expressed [26] as

$$\tau(x)\big|_{y=t_b/2} = a\tau_0[\delta(x-a)-\delta(x+a)], \tag{A.1}$$

where $2a$ is the PWAS length, $a\tau_0$ is the shear stress amplitude at the PWAS ends, and δ is the Dirac Delta function. For this shear stress condition, the x-direction strains resulted from symmetric and anti-symmetric Lamb wave modes can be represented [26] as

$$\varepsilon_x(x,t)\big|_{y=t_b/2} = -i\frac{a\tau_0}{G}\left[\sum_{k^S}\sin(k^S a)\frac{N_S(k^S)}{D_S'(k^S)}\mathrm{e}^{-i(k^S x-\omega t)} + \sum_{k^A}\sin(k^A a)\frac{N_A(k^A)}{D_A'(k^A)}\mathrm{e}^{-i(k^A x-\omega t)}\right], \tag{A.2}$$

where t_b is the plate thickness, G is the shear modulus of the plate, ω is the angular frequency, k is the wave number, and the superscripts or subscripts of S and A represent the symmetric and anti-symmetric modes, respectively. In Eqs. (A.1) and (A.2), the origins of the x- and y-axes are set to the center of the PWAS and the middle of the plate, respectively, and the PWAS is installed on the top plate surface. Additionally, N_S, D_S, N_A, and D_A in Eqs. (A.2) and (A.3) are represented as

$$N_S = kq(k^2 + q^2)\cos(p\frac{t_b}{2})\cos(q\frac{t_b}{2}), \tag{A.3}$$

$$N_A = kq(k^2 + q^2)\sin(p\frac{t_b}{2})\sin(q\frac{t_b}{2}), \tag{A.4}$$

$$D_S = (k^2 - q^2)^2\cos(p\frac{t_b}{2})\sin(q\frac{t_b}{2}) + 4k^2pq\sin(p\frac{t_b}{2})\cos(q\frac{t_b}{2}), \tag{A.5}$$

and

$$D_A = (k^2 - q^2)^2\sin(p\frac{t_b}{2})\cos(q\frac{t_b}{2}) + 4k^2pq\cos(p\frac{t_b}{2})\sin(q\frac{t_b}{2}). \tag{A.6}$$

In Eqs. (A.3) – (A.6), the p and q satisfy

$$p^2 = (\frac{\omega}{c_L})^2 - k^2,\ q^2 = (\frac{\omega}{c_T})^2 - k^2, \tag{A.7}$$

where c_L and c_T are the longitudinal and shear wave speeds, respectively, in the plate. In Eq. (A.2), k^S and k^A are the roots of $D_S = 0$ and $D_A = 0$ in Eqs. (A.5) and (A.6), respectively, and the prime symbol represents the derivative with respect to k. For the x-direction strains of the S0 and A0 modes, Eq. (A.2) can be simplified as

$$\varepsilon_x(x,t)\big|_{y=t_b/2}^{S_0} = -i\frac{a\tau_0}{G}\sin(k^{S_0}a)\frac{N_S(k^{S_0})}{D_S'(k^{S_0})}\mathrm{e}^{-i(k^{S_0}x-\omega t)}, \tag{A.8}$$

and

$$\varepsilon_x(x,t)\big|_{y=t_b/2}^{A_0} = -i\frac{a\tau_0}{G}\sin(k^{A_0}a)\frac{N_S(k^{A_0})}{D_S'(k^{A_0})}\mathrm{e}^{-i(k^{A_0}x-\omega t)}. \tag{A.9}$$

B. Relation between Structural Damping Coefficient and Imaginary Part of Wavenumber

Some wave types in this structural-damping-free system do not decay out, which is impossible in reality. In order to include structural damping effects, the "complex" Young's modulus [43] is here defined as

$$\bar{E} = E(1+\eta i)\,, \tag{B.1}$$

where η is the structural damping coefficient and E is the Young's modulus. For a low frequency component of A0 Lamb wave mode, it can be assumed as a flexural wave. This can be check by that dispersion curve of flexural wave is aligned to that of Lamb A0 mode at a low frequency [50]. Flexural wave equation is

$$\frac{EI}{1-\nu^2}(1+i\eta)\frac{\partial^4 u}{\partial x^4} + \rho h \frac{\partial^2 u}{\partial t^2} = 0\,. \tag{B.2}$$

By assuming solution as $u(x,t) =$ A $\exp(-ikx+i\omega t)$ and substituting into Eq. (B.2)

$$k = \left(\frac{\rho h(1-\nu^2)}{EI(1+\eta i)}\omega^2 \right)^{1/4}\,. \tag{B.3}$$

By using Eq. (B.4) and substituting into (B.3), Eq. (B.6) can be obtained.

$$1+\eta i = \sqrt{1+\eta^2}\,\mathrm{e}^{-i\theta}\,, \tag{B.4}$$

where

$$\tan\theta = \eta\,, \tag{B.5}$$

$$k = \left(\frac{\rho h(1-\nu^2)}{EI} \omega^2 \right)^{1/4} \frac{e^{-i\theta/4}}{(1+\eta i)^{1/8}} = k_{no\_decay} \{ \frac{\cos(\theta/4) - i\sin(\theta/4)}{(1+\eta i)^{1/8}} \} . \quad \text{(B.6)}$$

When η is small, finally, the relation, $\beta = \eta/4$, can be obtained.

$$k = k_{no\_decay}(1 - \eta/4\, i) = k_{no\_decay}(1 - \beta i) . \quad \text{(B.7)}$$

C. Identification of Structural Wave Propagation Characteristics Using Analytical Approach

C.1 Ultrasonic Lamb Wave Propagation on Panel

Figure 40 shows the stresses acting on the six surfaces of a small rectangular element. By applying the Newton's Second Law in the *x*-direction, Eq. (C.1) can be obtained as [38]

$$\frac{\partial \sigma_x}{\partial x} + \frac{\partial \tau_{yx}}{\partial y} + \frac{\partial \tau_{zx}}{\partial z} + \rho f_x = \rho \frac{\partial^2 u_x}{\partial t^2} , \quad \text{(C.1)}$$

where *f* is an external force and *u* is the displacement. By repeating in the *y*- and *z*-directions, the momentum equation can be represented in a tensor form as

$$\sigma_{ij,j} + \rho f_i = \rho \frac{\partial^2 u_i}{\partial t^2} . \quad \text{(C.2)}$$

Additionally, the strain-displacement and stress-strain relations [38] are expressed, respectively, as

$$\varepsilon_{ij} = \frac{1}{2}(u_{i,j} + u_{j,i}) , \quad \text{(C.3)}$$

$$\sigma_{ij} = \lambda \varepsilon_{kk} \delta_{ij} + 2\mu \varepsilon_{ij}, \tag{C.4}$$

where λ and μ are the Lamé constants. Eqs. (C.2) and (C.3) are valid for any continuous media, while Eq. (C.4) is applicable only to isotropic elastic materials. Therefore, in order to investigate orthotropic materials or anisotropic materials, Eq. (C.4) is required to be modified. By combining Eqs. (C.2), (C.3), and (C.4), the equation of motion can be obtained in terms of the displacements as

$$(\lambda + \mu) u_{j,ij} + \mu u_{i,jj} + \rho f_i = \rho \ddot{u}_i . \tag{C.5}$$

By setting the external force *f* to zero in Eq. (C.5) and expressing it in a vector form, Eq. (C.5) can be rewritten as

$$(\lambda + \mu) \nabla \nabla \cdot \mathbf{u} + \mu \nabla^2 \mathbf{u} = \rho \frac{\partial^2 \mathbf{u}}{\partial t^2} . \tag{C.6}$$

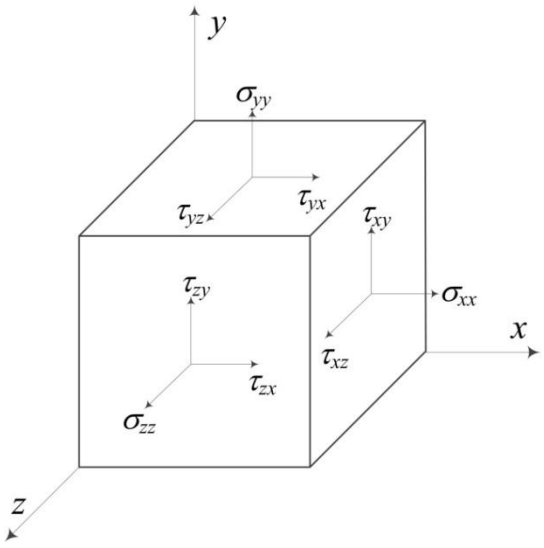

Figure 40: Stresses acting on the six surfaces of a small rectangular element.

A plane strain case of a free panel is described in Fig. 41. The Lamb wave is a guided wave that is described by the governing equation, Eq. (C.6) along with the stress-free boundary conditions in Eq. (C.7).

$$\sigma_{yy} = \tau_{xy} = 0 \text{ at } y = \pm h . \tag{C.7}$$

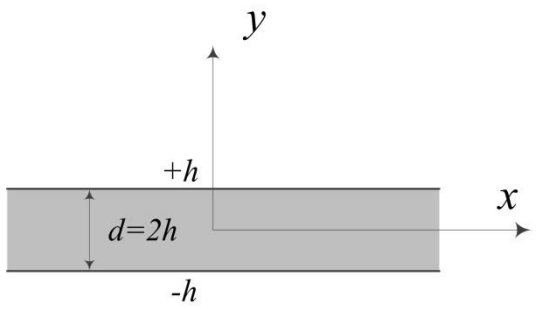

Figure 41: Geometry of a panel for Lamb waves.

The displacement vector, **u** can be expressed as a summation of both the gradient of a scalar potential φ and the curl of a vector potential **H** (i.e. $\mathbf{u} = \nabla\varphi + \nabla\times\mathbf{H}$). By substituting this potential relation into Eq. (C.6),

$$\nabla[(\lambda+2\mu)\nabla^2\varphi - \rho\frac{\partial^2\varphi}{\partial t^2}] + \nabla\times[\mu\nabla^2\mathbf{H} - \rho\frac{\partial^2\mathbf{H}}{\partial t^2}] = 0 . \tag{C.8}$$

From Eq. (C.8), the uncoupled two wave equations (i.e. longitudinal and shear wave equations) in the case of the plane strain can be obtained [3] as $\frac{\partial^2\phi}{\partial x^2} + \frac{\partial^2\phi}{\partial y^2} = \frac{1}{c_L{}^2}\frac{\partial^2\phi}{\partial t^2}$,

(C.9)

$$\frac{\partial^2\psi}{\partial x^2}+\frac{\partial^2\psi}{\partial y^2}=\frac{1}{{c_T}^2}\frac{\partial^2\psi}{\partial t^2}\,, \tag{C.10}$$

where $c_L = [(2\lambda+\mu)/\rho]^{0.5}$ is the phase speed of longitudinal waves, $c_T = (\mu/\rho)^{0.5}$ is the phase speed of shear waves, and ψ is a potential defined as $\psi = \partial H_y/\partial x - \partial H_y/\partial x$. With an assumption of plane strain, the displacement vector **u** can be expressed in term of the potentials: i.e.,

$$\mathbf{u}=\begin{bmatrix} u_x & u_y & u_z \end{bmatrix}^{\mathrm{T}}=\begin{bmatrix} \dfrac{\partial\phi}{\partial x}+\dfrac{\partial\psi}{\partial y} & \dfrac{\partial\phi}{\partial y}-\dfrac{\partial\psi}{\partial x} & 0 \end{bmatrix}^{\mathrm{T}}. \tag{C.11}$$

Then, the stresses on the surfaces in Eq. (C.2) can be related with the potentials [3] as

$$\sigma_{yy}=\lambda(\frac{\partial u_x}{\partial x}+\frac{\partial u_y}{\partial y})+2\mu\frac{\partial u_y}{\partial y}=\lambda(\frac{\partial^2\phi}{\partial x^2}+\frac{\partial^2\phi}{\partial y^2})+2\mu(\frac{\partial^2\phi}{\partial y^2}-\frac{2\partial^2\psi}{\partial x\partial y})\,, \tag{C.12}$$

$$\tau_{xy}=\mu(\frac{\partial u_y}{\partial x}+\frac{\partial u_x}{\partial y})=\mu(\frac{\partial^2\phi}{\partial x\partial y}-\frac{\partial^2\psi}{\partial x^2}+\frac{\partial^2\psi}{\partial y^2})\,. \tag{C.13}$$

Assume the solutions of Eqs. (C.9) and (C.10) as

$$\phi=\Phi(y)\exp[i(kx-\omega t)]\,, \tag{C.14}$$

$$\psi=\Psi(y)\exp[i(kx-\omega t)]\,, \tag{C.15}$$

where k is wavenumber and ω is angular velocity. The wave amplitudes in Eqs. (C.14) and (C.15) can be also assumed as

$$\Phi(y)=A_1\sin(py)+A_2\cos(py)\,, \tag{C.16}$$

$$\Psi(y) = B_1 \sin(qy) + B_2 \cos(qy) \ , \tag{C.17}$$

$$p^2 = \frac{\omega^2}{c_L{}^2} - k^2 , \tag{C.18}$$

$$q^2 = \frac{\omega^2}{c_T{}^2} - k^2 . \tag{C.19}$$

Now, the symmetric waves can be defined when u_x is symmetric with respect to the x-axis in Fig. 41 and u_y is anti-symmetric with respect to the x-axis: i.e.

$$\Phi(y) = A_2 \cos(py) , \tag{C.20a}$$

$$\Psi(y) = B_1 \sin(qy) , \tag{C.20b}$$

$$u_x(x,y,t) = [ikA_2 \cos(py) + qB_1 \cos(qy)]\mathrm{e}^{i(kx-\omega t)} , \tag{C.20c}$$

$$u_y(x,y,t) = [-pA_2 \sin(py) - ikB_1 \sin(qy)]\mathrm{e}^{i(kx-\omega t)} , \tag{C.20d}$$

$$\sigma_{yy}(x,y,t) = \{-\lambda(k^2 + p^2)A_2 \cos(py) - 2\mu[p^2 A_2 \cos(py) + ikqB_1 \cos(qy)]\}\mathrm{e}^{i(kx-\omega t)} , \tag{C.20e}$$

$$\tau_{xy}(x,y,t) = \mu[-2ikpA_2 \sin(py) + (k^2 - q^2)B_1 \sin(qy)]\mathrm{e}^{i(kx-\omega t)} . \tag{C.20f}$$

Similarly, the anti-symmetric wave modes are

$$\Phi(y) = A_1 \sin(py) , \tag{C.21a}$$

$$\Psi(y) = B_2 \cos(qy) , \tag{C.21b}$$

$$u_x(x,y,t) = [ikA_1 \sin(py) - qB_2 \sin(qy)]\mathrm{e}^{i(kx-\omega t)} , \tag{C.21c}$$

$$u_y(x,y,t) = [pA_1\cos(py) - ikB_2\cos(qy)]\mathrm{e}^{i(kx-\omega t)}, \quad \text{(C.21d)}$$

$$\sigma_{yy}(x,y,t) = \{-\lambda(k^2+p^2)A_1\sin(py) - 2\mu[p^2A_1\sin(py) - ikqB_2\sin(qy)]\}\mathrm{e}^{i(kx-\omega t)}, \quad \text{(C.21e)}$$

$$\tau_{xy}(x,y,t) = \mu[2ikpA_1\cos(py) + (k^2-q^2)B_2\cos(qy)]\mathrm{e}^{i(kx-\omega t)}. \quad \text{(C.21f)}$$

By applying the boundary conditions in Eq. (C.7) to Eqs. (C.20) and (C.21), Eqs. (C.22) and (C.23) for the symmetric and anti-symmetric waves, respectively, can be derived as

$$\begin{bmatrix} -2ikp\sin(ph) & (k^2-q^2)\sin(qh) \\ \lambda(k^2+p^2)\cos(ph) + 2\mu p^2\cos(ph) & 2\mu ikq\cos(qh) \end{bmatrix}\begin{bmatrix} A_2 \\ B_1 \end{bmatrix} = 0, \quad \text{(C.22)}$$

$$\begin{bmatrix} \lambda(k^2+p^2)\sin(ph) + 2\mu p^2\sin(ph) & -2\mu ikq\sin(qh) \\ 2ikp\cos(ph) & (k^2-q^2)\cos(qh) \end{bmatrix}\begin{bmatrix} A_1 \\ B_2 \end{bmatrix} = 0. \quad \text{(C.23)}$$

For non-trivial solutions, the determinants of the coefficient matrices in Eqs. (C.22) and (C.23) should be zero. Then, the dispersion (k-ω) relation of the symmetric wave modes can be obtained from

$$\frac{\tan(qh)}{\tan(ph)} = \frac{-4k^2qp}{(q^2-k^2)^2}. \quad \text{(C.24)}$$

Similarly, the dispersion relation of the anti-symmetric modes is obtained by solving the following equation:

$$\frac{\tan(qh)}{\tan(ph)} = \frac{-(q^2-k^2)^2}{4k^2qp}. \quad \text{(C.25)}$$

The mode shapes of the symmetric waves can be obtained by substituting the wavenumbers and frequencies obtained from Eq. (C.24) into Eqs. (C.22), (C.20b), and (C.20c). The mode shapes of the anti-symmetric waves are also calculated in the same way.

C.2 Shear Horizontal Plate Wave: Love Wave

The Shear Horizontal (SH) waves are governed by Eq. (C.6), propagating in the *x*-direction with the particle motions limited only in the *z*-direction (i.e. $u_x = u_y = 0$). The SH waves also satisfy the boundary conditions in Eq. (C.26) [3]:

$$\tau_{yz} = 0 \text{ at } y = \pm h. \tag{C.26}$$

The equation of motion in this case is represented from Eq. (C.6) as

$$\frac{\partial^2 u_z}{\partial x^2} + \frac{\partial^2 u_z}{\partial y^2} = \frac{1}{c_T{}^2}\frac{\partial^2 u_z}{\partial t}. \tag{C.27}$$

The solution of Eq. (C.27) can be assumed as

$$u_z(x, y, t) = f(y)e^{i(kx-\omega t)}. \tag{C.28}$$

By substituting Eq. (C.28) to Eq. (C.27) and defining $\eta = \omega^2/c_T{}^2 - k^2$,

$$f''(y) + \eta^2 f(y) = 0. \tag{C.29}$$

Then, the assumed solution of Eq. (C.28) can be written as

$$u_z(x, y, t) = (C_1 \sin \eta y + C_2 \cos \eta y)\, e^{i(kx-\omega t)}. \tag{C.30}$$

By using stress-strain relation (i.e. $\tau_{yz} = \mu\, \partial u_z/\partial y$) and applying the boundary conditions in Eq. (C.26) to Eq. (C.30), the following eigenvalue problem is obtained:

$$\begin{bmatrix} \cos\eta h & -\sin\eta h \\ \cos\eta h & \sin\eta h \end{bmatrix} \begin{bmatrix} C_1 \\ C_2 \end{bmatrix} = 0 . \tag{C.31}$$

The determinant of the coefficient matrix in Eq. (C.31) should be zero for a non-trivial solution: i.e.,

$$\cos\eta h \sin\eta h = 0 . \tag{C.32}$$

For the symmetric SH wave, $\sin\eta h = 0$ is satisfied: i.e.

$$\eta_s h = n\pi,\ u_z^{\,s}(x,y,t) = C_2 \cos\eta y\ e^{i(kx-\omega t)} . \tag{C.33}$$

Similarly, the anti-symmetric SH wave is represented as

$$\eta_A h = \frac{(2n+1)}{2}\pi,\ u_z^{\,A}(x,y,z) = C_1 \sin\eta y\ e^{i(kx-\omega t)} . \tag{C.34}$$

From the definition of η (i.e. $\eta = \omega^2/c_T^{\,2} - k^2$), the SH wave speed is obtained for both η_s and η_A as

$$c(\omega) = \frac{c_T}{\sqrt{1-\eta^2\left(\frac{c_T}{\omega}\right)^2}} . \tag{C.35}$$

C.3 Ultrasonic Wave Propagation in Circular Pipe

For the purpose of understanding acoustic characteristics of ultrasonic waves propagating in a pipe, analytical solutions are presented in this section [3, 5]. Figure 42

illustrates a circular pipe in the cylindrical coordinates. As described in Section C.1, Eq. (C.6) is valid for any isotropic media (i.e., the displacement vector **u** in the cylindrical coordinate satisfies the Navier's governing equations Eq. (C.6)).

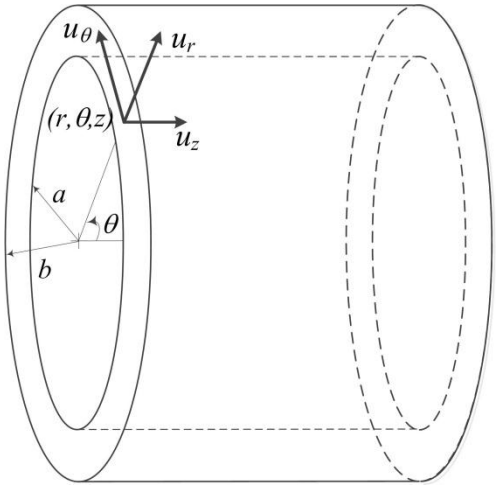

Figure 42: Cylindrical coordinates.

From Eq. (C.8), the two wave equations in the cylindrical coordinates can be obtained as

$$\nabla^2\Phi = \frac{1}{{c_L}^2}\frac{\partial^2\Phi}{\partial t^2}, \tag{C.36a}$$

$$\nabla^2\mathbf{H} = \frac{1}{{c_T}^2}\frac{\partial^2\mathbf{H}}{\partial t^2}. \tag{C.36b}$$

Assume the solutions of these wave equations in cylindrical coordinate as [5]

$$\Phi = f(r)\cos(n\theta)\cos(\omega t + kz), \tag{C.37a}$$

$$H_r = g_r(r)\sin(n\theta)\sin(\omega t + kz)\,, \tag{C.37b}$$

$$H_\theta = g_\theta(r)\cos(n\theta)\sin(\omega t + kz)\,, \tag{C.37c}$$

$$H_z = g_3(r)\sin(n\theta)\cos(\omega t + kz)\,. \tag{C.37d}$$

By substituting Eq. (C.37) into Eq. (C.36), Eq. (C.36) can be represented as

$$(\nabla^2 + \frac{\omega^2}{c_L{}^2})\Phi = 0\,, \tag{C.38a}$$

$$(\nabla^2 + \frac{\omega^2}{c_T{}^2})H_z = 0\,, \tag{C.38b}$$

$$(\nabla^2 - \frac{1}{r^2} + \frac{\omega^2}{c_T{}^2})H_r - \frac{2}{r^2}\frac{\partial H_\theta}{\partial \theta} = 0\,, \tag{C.38c}$$

$$(\nabla^2 - \frac{1}{r^2} + \frac{\omega^2}{c_T{}^2})H_\theta + \frac{2}{r^2}\frac{\partial H_r}{\partial \theta} = 0\,. \tag{C.38d}$$

From $\mathbf{u} = \nabla\varphi + \nabla\times\mathbf{H}$,

$$\begin{aligned}\mathbf{u} &= (\frac{\partial \Phi}{\partial r} + \frac{1}{r}\frac{\partial H_z}{\partial \theta} - \frac{\partial H_\theta}{\partial z})\hat{r} + (\frac{1}{r}\frac{\partial \Phi}{\partial \theta} + \frac{\partial H_r}{\partial z} - \frac{\partial H_z}{\partial r})\hat{\theta} + (\frac{\partial \Phi}{\partial z} + \frac{1}{r}H_\theta + \frac{\partial H_\theta}{\partial z} - \frac{1}{r}\frac{\partial H_r}{\partial \theta})\hat{z} \\ &= u_r\hat{r} + u_\theta\hat{\theta} + u_z\hat{z}\end{aligned}\,. \tag{C.39}$$

By substituting Eq. (C.37) into (C.39), the displacements can be written as

$$u_r = U(r)\cos n\theta\cos(\omega t + kz)\,, \tag{C.40a}$$

$$u_\theta = V(r)\sin n\theta\cos(\omega t + kz)\,, \tag{C.40b}$$

$$u_z = w(r)\cos n\theta \sin(\omega t + kz). \tag{C.40c}$$

The strain-displacement relations in the cylindrical coordinates are

$$\varepsilon_{rr} = \frac{\partial u_r}{\partial r}, \tag{C.41a}$$

$$\varepsilon_{rz} = \frac{1}{2}\left(\frac{\partial u_r}{\partial z} + \frac{\partial u_z}{\partial r}\right), \tag{C.41b}$$

$$\varepsilon_{r\theta} = \frac{1}{2}\left[r\frac{\partial}{\partial r}\left(\frac{u_\theta}{r}\right) + \frac{1}{r}\frac{\partial u_r}{\partial \theta}\right]. \tag{C.41c}$$

The stress-strain relations are represented as

$$\sigma_{rr} = \lambda \nabla^2 \Phi + 2\mu \varepsilon_{rr}, \tag{C.42a}$$

$$\sigma_{rz} = 2\mu \varepsilon_{rz}, \tag{C.42b}$$

$$\sigma_{r\theta} = 2\mu \varepsilon_{r\theta}. \tag{C.42c}$$

The stress-free boundary conditions are

$$\sigma_{rr} = \sigma_{rz} = \sigma_{r\theta} = 0 \qquad at\ r = a,\ r = b. \tag{C.43}$$

By combining Eqs. (C.40)-(C.42) and applying the boundary conditions in Eq. (C.43), dispersion relation for a circular pipe can be obtained as [3,5]

$$\begin{vmatrix} c_{11} & c_{12} & c_{13} & c_{14} & c_{15} & c_{16} \\ c_{21} & c_{22} & c_{23} & c_{24} & c_{25} & c_{26} \\ c_{31} & c_{32} & c_{33} & c_{34} & c_{35} & c_{36} \\ c_{41} & c_{42} & c_{43} & c_{44} & c_{45} & c_{46} \\ c_{51} & c_{52} & c_{53} & c_{54} & c_{55} & c_{56} \\ c_{61} & c_{62} & c_{63} & c_{64} & c_{65} & c_{66} \end{vmatrix} = 0 \ , \tag{C.44}$$

where

$$c_{11} = [2n(n-1) - (\beta^2 - k^2)a^2]Z_n(\alpha_1 a) + 2\lambda_1\alpha_1 a Z_{n+1}(\alpha_1 a) , \tag{C.45a}$$

$$c_{12} = 2k\beta_1 a^2 Z_n(\beta_1 a) - 2ka(n+1)Z_{n+1}(\beta_1 a) , \tag{C.45b}$$

$$c_{13} = -2n(n-1)Z_n(\beta_1 a) + 2\lambda_2 n\beta_1 a Z_{n+1}(\beta_1 a) , \tag{C.45c}$$

$$c_{14} = [2n(n-1) - (\beta^2 - k^2)a^2]W_n(\alpha_1 a) + 2\alpha_1 a W_{n+1}(\alpha_1 a) , \tag{C.45d}$$

$$c_{15} = 2\lambda_2 k\beta_1 a^2 W_n(\beta_1 a) - 2ka(n+1)W_{n+1}(\beta_1 a) , \tag{C.45e}$$

$$c_{16} = -2n(n-1)W_n(\beta_1 a) + 2n\beta_1 a W_{n+1}(\beta_1 a) , \tag{C.45f}$$

$$c_{21} = 2n(n-1)Z_n(\alpha_1 a) - 2\lambda_1 n\alpha_1 a Z_{n+1}(\alpha_1 a) , \tag{C.45g}$$

$$c_{22} = -k\beta_1 a^2 Z_n(\beta_1 a) + 2ka(n+1)Z_{n+1}(\beta_1 a) , \tag{C.45h}$$

$$c_{23} = -[2n(n-1) - \beta^2 a^2]Z_n(\beta_1 a) + 2\lambda_2\beta_1 a Z_{n+1}(\beta_1 a) , \tag{C.45i}$$

$$c_{24} = 2n(n-1)W_n(\alpha_1 a) - 2n\alpha_1 a W_{n+1}(\alpha_1 a) , \tag{C.45j}$$

$$c_{25} = -\lambda_2 k\beta_1 a^2 W_n(\beta_1 a) + 2ka(n+1)W_{n+1}(\beta_1 a) , \tag{C.45k}$$

$$c_{26} = -[2n(n-1) - \beta^2 a^2]W_n(\beta_1 a) - 2\beta_1 a W_{n+1}(\beta_1 a), \tag{C.45l}$$

$$c_{31} = 2nkaZ_n(\alpha_1 a) + 2\lambda_1 k\alpha_1 a^2 Z_{n+1}(\alpha_1 a), \tag{C.45m}$$

$$c_{32} = -n\beta_1 aZ_n(\beta_1 a) + (\beta^2 - k^2)a^2 Z_{n+1}(\beta_1 a), \tag{C.45n}$$

$$c_{33} = nkaZ_n(\beta_1 a), \tag{C.45o}$$

$$c_{34} = -2nkaW_n(\alpha_1 a) + 2k\alpha_1 a^2 W_{n+1}(\alpha_1 a), \tag{C.45p}$$

$$c_{35} = -\lambda_2 n\beta_1 aW_n(\beta_1 a) + (\beta^2 - k^2)a^2 W_{n+1}(\beta_1 a), \tag{C.45q}$$

$$c_{36} = nkaW_n(\beta_1 a). \tag{C.45r}$$

where $\alpha^2 = \omega^2/c_L^2 - k^2$, $\beta^2 = \omega^2/c_T^2 - k^2$, Z_n and W_n are the Bessel function or the modified Bessel function (see Table 13), and λ_1 and λ_2 are 1 or -1 as shown in Table 13. From c_{41} to c_{66}, their values are same as c_{11} to c_{36} except for changing a in Eq. (C.45) to b. For n = 0, Eq (C.44) is decomposed as

$$D = D_1 \square D_2 = 0, \tag{C.46}$$

where

$$D_1 = \begin{vmatrix} c_{11} & c_{12} & c_{14} & c_{15} \\ c_{31} & c_{32} & c_{34} & c_{35} \\ c_{41} & c_{42} & c_{44} & c_{45} \\ c_{61} & c_{62} & c_{64} & c_{65} \end{vmatrix} \text{ and } D_2 = \begin{vmatrix} c_{23} & c_{26} \\ c_{53} & c_{56} \end{vmatrix}. \tag{C.47}$$

The dispersion relations for the longitudinal modes are obtained from $D_1 = 0$ and for the torsional modes, $D_2 = 0$.

Interval	Functions (Z_n :J or I) and (W_n : Y or K)
$c_L < c_p$ or $\alpha^2, \beta^2 > 0$	$J_n(\alpha r)$ and $Y_n(\alpha r)$, $J_n(\beta r)$ and $Y_n(\beta r)$
$c_L > c_p >$ c$_T$ or $\alpha^2 < 0\ \beta^2 > 0$	$I_n(\alpha_1 r)$ and $K_n(\alpha_1 r)$, $J_n(\beta r)$ and $Y_n(\beta r)$
$c_p < c_T$ or $\alpha^2 < 0\ \beta^2 < 0$	$I_n(\alpha_1 r)$ and $K_n(\alpha_1 r)$, $I_n(\beta_1 r)$ and $K_n(\beta_1 r)$

Condition	λ_1(related to Z_n) and λ_2 (related to W_n)
J and Y are used	1
I and K are used	-1

Table 13: Bessel functions in Eq. (C.45) and λ_1 and λ_2 values.